PHD

Scanning Tunnelling Microscopy of Si(111)-7x7: Local Atomic Manipulation and Light Emission

Purkiss, Rebecca

Award date:
2018

Awarding institution:
University of Bath

Scanning Tunnelling Microscopy of Si(111)-7x7: Local Atomic Manipulation and Light Emission

Rebecca Mary Purkiss

A thesis submitted for the degree of Doctor of Philosophy

University of Bath
Department of Physics

July 2018

Signed: …………………………………………………… - Rebecca Purkiss

Abstract

In this thesis, the injection of tunnel current from the STM tip is utilised to locally manipulate individual toluene molecules and also result in the emission of light from the tunnel junction.

Current injection pulses result in the local manipulation of toluene molecules on the Si(111)-7x7 surface. Investigating the rate of manipulation shows an increase with the tunnel current, indicative of a 1-electron process for electron injection at +1.6 V. For hole injection at -1.3 V, this trend exists for low current (2 – 10 pA), but plateaus for high current injections (10 - 900 pA), indicating a 0-electron process with manipulation invariant to the injected current.

The probability of manipulation is measured to decrease for high current hole injection, at small tip-sample separation distances. We propose that this occurs as a result of the tip quenching the excited-state lifetime of the molecule by over two orders of magnitude, due to the creation of a tip-dependent interface state on the molecule, creating a new decay channel for the excited state.

The ability to influence the manipulation process has led to investigating the branching ratio of this system, to determine whether the outcome of the manipulation event can be selected. The branching ratio has been measured and found to be invariant as a function of: voltage, the corresponding tip height, electric field and position. This suggests a 1.4 V threshold to local manipulation and that the manipulation events each occur with the same excited state form. Charge must undergo ultra-fast relaxation to 1.4 V before initiating manipulation when transitioning from this state.

Light emission has been investigated on the same Si(111)-7x7 surface, with the voltage dependence of emission revealing a 1.9 ± 0.3 V threshold, matching that of non-local manipulation. We propose that the mechanism of non-local manipulation and light emission must have a common origin. Once the injected charge has relaxed to the bottom of the surface state (~2 V), transitions from this state can occur via two inelastic decay channels. One results in the manipulation of molecules and the other, light emission. This mechanism is used to re-interpret results previously published by other research groups.

The possibility of observing these effects on a new system of graphite dosed with oxygen atoms is documented, with preliminary work to reliably dose and image the surface.

Acknowledgements

I would like to thank my project supervisor Dr. Peter Sloan for your help and guidance throughout this PhD, and for the constant encouragement to ‘keep chipping away’! Thanks to Kristina Rusimova for your willingness to help and explain and for training me to get the STM up and running. Thanks also to the Condensed Matter Physics Centre for Doctoral Training, for the training and opportunities to explore more areas of physics in our first year.

A huge thank you to all the technicians, Jenny, Paul, Isabel, Martin, Wendy, Stephen and Ashley, your help in making, fixing and supplying things for the lab has been amazing and being able to escape the lab for chats with you all has been invaluable! Thanks also to Dr. Peter Mosley for the use of the *Andor Luca* camera and help with the photon experimental setup. Thank you to all the Physics department lecturers especially Sergey and Gary, you’ve all made studying fun and encouraged me to keep going!

Thank you to all the best Physics PhDs buddies to have embarked on this journey together – 8 years with some of you has been a blast! Finally, I couldn’t have done this without the support of my amazing family and friends– your skypes when things go wrong have kept me going! And to my husband-to-be Phil, thank you!

> “Now all glory to God, who is able, through his mighty power at work
> within us, to accomplish infinitely more than we might ask or think.”
> Ephesians 3:20

Four years studying a small portion of the awesomeness of His creation.

Contents

INTRODUCTION 1

SCANNING TUNNELLING MICROSCOPY 4

2.1 Quantum Tunnelling Theory 4

2.2 Tunnelling current 6

2.3 Experimental Setup 8

ATOMIC MANIPULATION OVERVIEW 10

3.1 Mechanical Manipulation 10

3.2 Electric Field Induced Manipulation 13

3.3 Tunnel Current Induced Manipulation 15
  - 3.3.1 Local Manipulation 15
  - 3.3.2 Non-Local Manipulation 17

EXPERIMENTAL TECHNIQUES 22

4.1 Omicron STM 1 Layout 22
  - 4.1.1 Load Lock 22
  - 4.1.2 Preparation Chamber 23
  - 4.1.3 STM Chamber 23

4.2 Pressure 24

4.3 Venting 24

4.4 Baking 25

4.5 Sample Mounting and Preparation 29

4.6 Tip Preparation 30
  - 4.6.1 Macro Scale 30
  - 4.6.2 Micro Scale 33

4.7 Gas Dosing 35

4.8 Silicon Surface 36
4.8.1 Surface Reconstruction 36
4.8.2 Electronic Structure 38

4.9 Molecular Bonding 40

AUTOMATION TECHNIQUES 43

5.1 Background 43

5.2 Drift Tracking 46

5.3 Injection 47

LOCAL MANIPULATION 49

6.1 Literature Review 49

6.2 Detecting manipulation 55

6.3 Results 55
6.3.1 Thermal Effects 56
6.3.2 Mechanical Tip Interaction 57
6.3.3 Electric Field Effect 58

6.4 Discussion 59

BRANCHING RATIOS 64

7.1 Literature Review 64

7.2 Experimental Improvements 67
7.2.1 Site Injection 67
7.2.2 Injection Accuracy Improvements 68
7.2.3 Stopping Injections 70

7.3 Results 72
7.3.1 Voltage dependence 72
7.3.2 Tip height dependence 74
7.3.3 Electric field dependence 75
7.3.4 Position Dependence 76

7.5 Future Work 80

LIGHT EMISSION 81

8.1 Literature Review of STM Light Emission 81

8.2 Preliminary Investigation 85

8.3 Results – Voltage Dependence 89
8.3.1 Electrons 89

8.3.2 Holes 90

8.4 Discussion 90

8.5 Future Work 93

GRAPHITE 96

9.1 Literature Review 96

9.2 Preliminary Results 98
9.2.1 Substrate Imaging 98
9.2.2 Dosing Technique 101

9.3 Future Work 103

SUMMARY 104

REFERENCES 106

Chapter 1

Introduction

This scientific story starts in 1982, when the Scanning Tunnelling Microscope (STM) was first invented by Binnig and Rohrer [1]. Since then, the STM has materialised Richard Feynman's dream of his 'Plenty of room at the bottom' speech; enabling not only precision imaging at the atomic scale, but atomic manipulation and controlling individual atoms [2].

The abilities of the STM reach into a range of fields of science, offering the capabilities to manipulate the position of individual atoms, demonstrated by the Don Eigler team with the IBM nanoadvert [3], and expanding into the Boy and his atom short film [4] shown in Figure 1. Other manipulation techniques like dissociation [5, 6], tautomerisation [7], and atomic switches [8], on a wide variety of materials have also been demonstrated. This is by no means an exhaustive list of the capabilities of an STM, also extending into light emission [9, 10] and property measurements of materials, such as the conductance of molecular wires [11] and electronic structure information from scanning tunnelling spectroscopy data [12, 13].

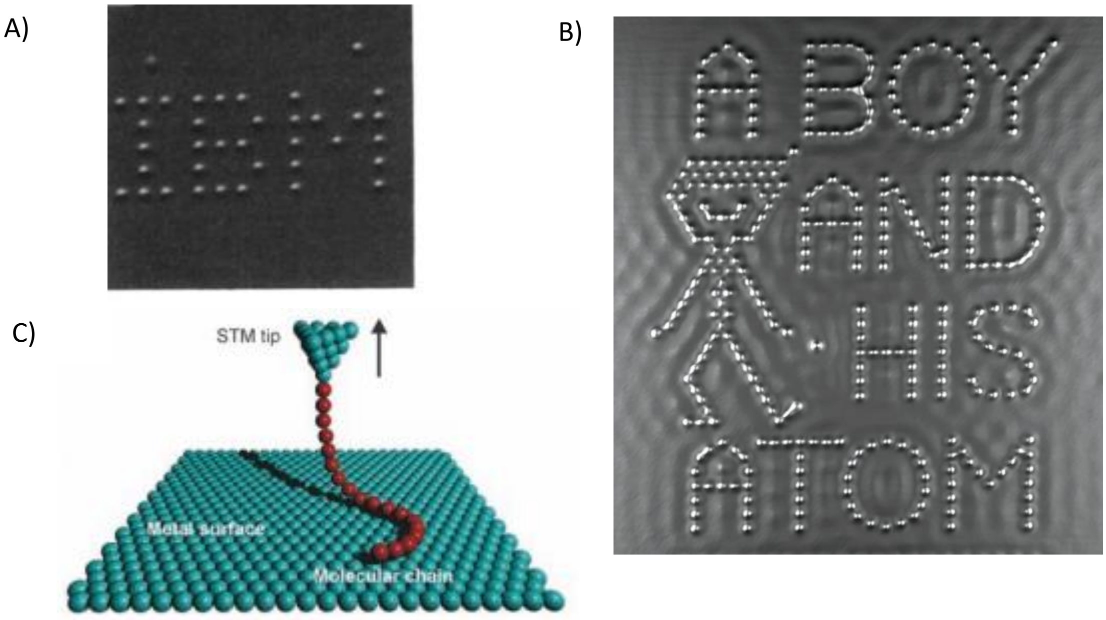

Figure 1: Examples of the capabilities of atomic manipulation with an STM. A): STM image of the IBM nanoadvert, created by mechanically manipulating xenon atoms on the nickel(110) surface. Each letter has a length top to bottom of 50 Å. [3] B): The 'boy and his atom' short film created by IBM with CO molecules on the Cu(111) surface. [4] C): Schematic of an STM tip lifting a molecular chain to measure the conductance through an atomic wire. [11]

The work in this thesis aims to investigate what happens to the charge injected from the STM tip into the Si(111)-7x7 surface. This is achieved by the manipulation of individual molecules and the emission of light from the system. Initially, I will outline the workings of the STM, and the experimental methods and techniques required to achieve reliable atomic resolution when imaging.

Chapter 6 will address local atomic manipulation, whereby an individual toluene molecule located directly below the STM tip, can be induced to move by the injection of tunnelling current above the molecule. The manipulation process occurs in the following three stages [14]: *Capture* - When the injected charge attaches onto a molecule and excites it. *Dynamics* - the excited molecule then follows its excited state potential. *Detachment* - this state decays leaving a vibrationally excited neutral molecule. During this process the molecule-surface bonds can be broken providing enough energy for the molecule to enter the physisorbed state and move on the surface, or to completely leave.

Investigating the rates of this manipulation mechanism reveals a plateau for hole injection at high current (>10 pA). This corresponds to a drop in the probability per hole for inducing manipulation. This suggests that the presence of the STM tip influences the manipulation process, resulting in the quenching of the excited-state lifetime of the molecule, from 10 fs to less than 0.1 fs. Hence influencing the *Dynamics* step of the manipulation process. We propose that this quenching occurs via the creation of a tip dependant channel for the excited state of the molecule to decay to, before its naturally elapsed lifetime.

The ability to influence the molecules excited state has prompted work on the types of manipulation outcomes observed following charge injection, documented in chapter 7. The branching ratio compares the observed manipulation outcomes, defined as the ratio of the number of diffusion to desorption events. The branching ratio is investigated as a function of voltage and other experimental parameters and is found to be constant (0.27 ± 0.03). This indicates a common final step to manipulation, *Detachment*, for both outcomes. The ratio of outcomes observed is therefore determined by the electronic states of the molecule/sample system and not influenced by the user.

Chapter 8 details how the same Si(111)-7x7 system has been investigated for its light emitting properties. Light emission is detected from the tunnel junction when the STM is in tunnelling contact. No light is detected when the measurement is repeated with the STM tip withdrawn from the surface, with no tunnelling current present. A range of mechanisms for light emission are documented in the literature. Probing the voltage dependence for this light emission reveals a voltage threshold that matches that of the non-local manipulation work previously reported by our research group. The proposal of a common mechanism for both manipulation and light emission is discussed and reinterpretation of previously published work is suggested within this new emission mechanism.

Finally, chapter 9 summarises initial work on a new system of graphite and oxygen atoms in the hope that these manipulation processes may be visible on other surfaces. Imaging the graphene and graphite surface is characterised and reliable stable imaging of graphite proves a suitable substrate to investigate on. Methods to crack molecular oxygen are documented and the use of an electron gun to create oxygen atoms to dose the surface proves successful.

1.1 Declaration of work done in conjunction with others

During my PhD I have worked closely with fellow PhD student Kristina Rusimova, who has trained me in the methods and techniques involved in being a UHV STM scientist. For the past two years I have been running the Omicron STM 1 machine independently, undertaking the daily tasks for its effective working and trouble-shooting on my own, with help from my supervisor Dr. Peter Sloan when complex issues have arisen.

Due to the volume of data required to get significant results, we have worked together on the same scientific story during this overlap and the data analysis software for this was already written by both Peter and Kristina prior to my arrival. Parts of these codes have been edited by myself to achieve necessary plots and analysis for my investigations.

Chapter 6 – Local Manipulation

-I have taken low current hole and high current electron injection data to confirm the initial trends seen in Kristina’s first results and carried out the same MATLAB analysis to extract rates from this data.

-Large tip height data was taken and analysed by myself to add onto the small tip height data taken by Kristina.

-The electric field data was solely taken by Kristina during her PhD, but is explained in detail in this thesis as it is crucial to conclusions drawn from this chapter.

Chapter 7 – Branching Ratio

-The branching ratio data was all taken and analysed by myself with adaptions to the pre-existing LabVIEW code for the halting injections carried out by Peter.

Chapter 8 – Light Emission

-Following discussion with Professor William Wadsworth and Dr Peter Mosley for the experimental setup (and the loan of Dr Mosley’s camera), the photon data was taken manually and analysed by myself.

-Comparisons to the non-local mechanism for electrons were drawn using non-local model parameters measured by Kristina.

-All STS data presented in this thesis was obtained by Kristina Rusimova, with analysis in chapter 8 carried out by myself.

Chapter 2

Scanning Tunnelling Microscopy

The STM founding phenomena involves the tunnelling of charges across the vacuum barrier in order to maintain a tunnelling current. A tunnelling current from the STM is obtained from the overlap of the wavefunctions of the tip and the surface. This chapter details the theory behind this tunnelling process and derives the relevant equations highlighting that an STM image consists of a topographic map of the local density of states (LDOS) of the surface imaged. See Rae for full derivation details [15].

2.1 Quantum Tunnelling Theory

The foundational physics underlying the workings of an STM can be derived using undergraduate physics looking at the solutions to the time-independent Schrödinger equation (TISE) in 1D for a finite potential barrier of width *d*,

$$-\frac{\hbar^2}{2m}\frac{d^2\psi}{dz^2}+V(z)\psi=E\psi \tag{2.1}$$

considering a particle of mass *m*, with a wavefunction ψ, and energy *E* incident on a potential barrier of height *V*, where *V>E*.

The TISE can be solved in three regions shown in Figure 2, before, within and after the barrier.

Region I: Potential *V=0*, so the TISE simplifies to

$$-\frac{\hbar^2}{2m}\frac{d^2\psi_1}{dz^2}=E\psi_1. \tag{2.2}$$

This has the general solution:

$$\psi_I=A\,exp(ik_Iz)+Bexp(-ik_Iz), \tag{2.3}$$

where *A* and *B* are constants and

$$k_I=\frac{\sqrt{2mE}}{\hbar}. \tag{2.4}$$

Region II: Within the barrier, $V=V_0$ substitutes into the TISE becoming

$$-\frac{\hbar^2}{2m}\frac{d^2\psi}{dz^2}+(V_0-E)\psi=0, \tag{2.5}$$

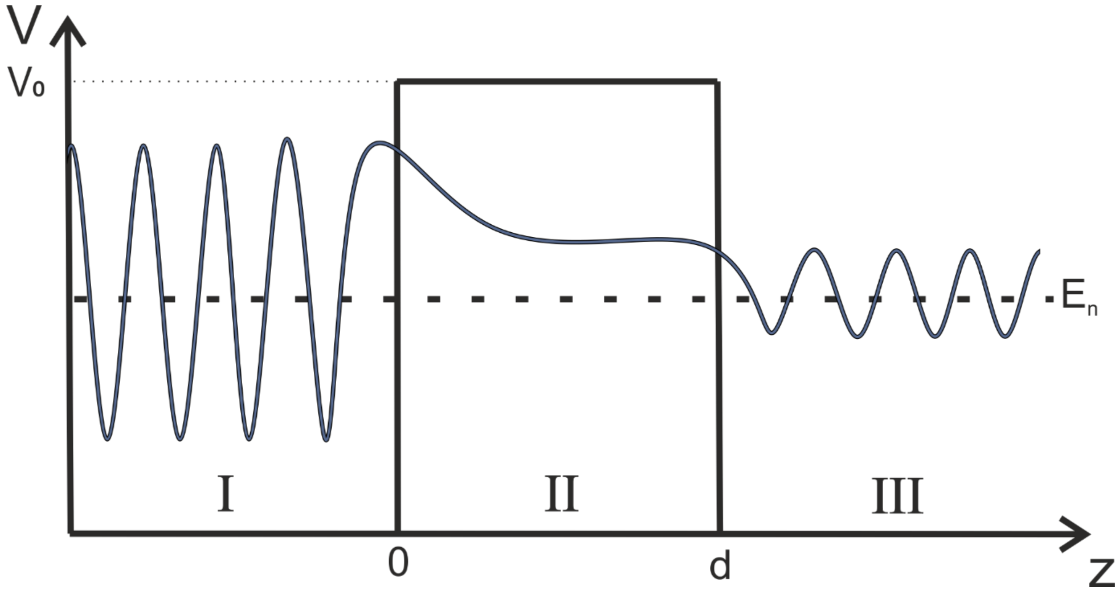

Figure 2: Schematic of a potential barrier of height V_0 and width d, with the wavefunction shown in blue, exponentially decaying within the barrier (II) and a finite probability beyond the barrier (III).

with the general solution

$$\psi_{II} = C\,exp(k_{II}z) + Dexp(-k_{II}z). \tag{2.6}$$

C and *D* are constants and

$$k_{II} = \frac{\sqrt{2m(V_0 - E)}}{\hbar}. \tag{2.7}$$

Region III: As in region I, the potential *V=0* again after the barrier and so the general solution has the same form as region I,

$$\psi_{III} = E\,exp(-ik_I z) + Fexp(ik_I z), \tag{2.8}$$

where *E* and *F* are constants. We can consider *E = 0*, as the particle travels in the positive *z* direction having left the barrier.

To solve for the constants in the general solutions, boundary conditions of a continuous wavefunction and its derivative must be obeyed at the barrier boundaries of *z=0* and *z=d*, shown in equations (2.9 - 2.10) and (2.11 - 2.12) respectively.

z=0:

$$A + B = C + D \tag{2.9}$$

$$A - B = \frac{k_{II}}{ik_I}(C - D) \tag{2.10}$$

z=d:

$$C\,exp(k_{II}d) + Dexp(-k_{II}d) = \ F\,exp(ik_Id) \tag{2.11}$$

$$C\,exp(k_{II}d) - Dexp(-k_{II}d) = \frac{ik_I}{k_{II}}F\,exp(ik_Id) \tag{2.12}$$

This allows the transmission coefficient of a particle through the barrier to be found from the ratio of the transmitted to incident beam:

$$\frac{F}{A} = \frac{4ik_Ik_{II}\,exp(-ik_Id)}{(2ik_Ik_{II} - k_I^2 + k_{II}^2)\,exp(-k_{II}d) + (2ik_Ik_{II} + k_I^2 - k_{II}^2)\,exp(k_{II}b)} \tag{2.13}$$

To find the transmission probability, *T*, this simplifies by assuming a large barrier where $exp(-k_{II}d) \rightarrow 0$, and finding the ratio of the transmitted to incident probabilities:

$$T = \frac{|F|^2}{|A|^2} = \frac{16k_I^2k_{II}^2}{(k_I^2 + k_{II}^2)^2}exp(-2k_{II}^2d) \tag{2.14}$$

This reveals non-zero probability of finding the particle beyond the barrier. It also shows how the transmission through the barrier has a dependence on V_0, the barrier height and *E* the particles energy (through the k_I and k_{II} parameters) and *d*, the width of the barrier. It is the exponential dependence on the tunnelling barrier distance, *d*, which results in the STMs ability to achieve atomic resolution.

2.2 Tunnelling current

This model can be extended to the STM whereby region I, II and III mimic the tip, vacuum and the sample respectively. In this situation, a voltage *V*, can be applied shifting the Fermi level of the tip relative to the sample and hence electrons from filled states in the tip can tunnel to empty states in the sample. The energy barrier to allow tunnelling is the ϕ, the workfunction of the metal, the energy required to raise an electron from the Fermi level to vacuum energy. For small bias, the work function of the tip and sample can be assumed the same, so all electrons observe the same barrier to tunnelling, as shown in Figure 3. (For larger applied bias the barrier to tunnelling can be considered as the average work function of both the tip, ϕ_t and the sample ϕ_s, where $(\frac{\phi_t+\phi_s}{2} - E)$ replaces the energy term in equation (2.7)).

For the small bias case, consider the wavefunction for the *nth* particle tunnelling from the tip to the sample at energy level E_n,

$$\psi_n(d) = \ \psi_n(0)\,exp(-k_{II}d) \tag{2.15}$$

where the probability of finding this particle beyond the barrier, *z=d* is,

$$P_n(d) = |\psi_n(0)|^2\,exp(-2k_{II}d) \tag{2.16}$$

here $\psi_n(0)$ gives the *nth* tip state at *z=0* and k_{II} can be considered as $\sqrt{\frac{2m(\phi-E)}{\hbar^2}}$. Assuming $\phi{\sim}\phi_s{\sim}\phi_t$ and $\phi >> eV$.

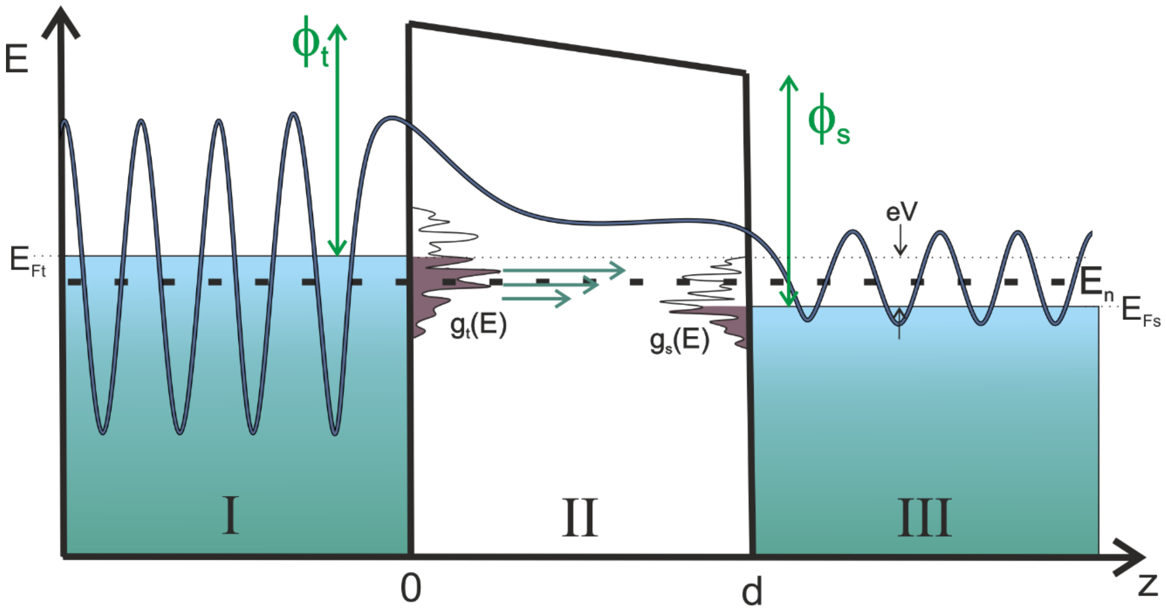

Figure 3: Schematic of quantum tunnelling through a potential barrier of width d, with the work function of the tip and sample ϕ_t and ϕ_s shown. The wavefunction of a particle with energy E_n is shown in blue with the shaded blue regions showing the filled states up to the Fermi levels of the tip (E_{Ft}) and sample (E_{Fs}) in region I and III respectively, shifted due to the application of bias V. The density of states of the tip $g_t(E)$ and sample $g_S(E)$ show tunnelling can occur in the region of occupied to unoccupied states indicated by the green arrows.

The tunnelling current is proportional to the probability of electrons that can tunnel through the barrier within the region of tunnelling states available. Those in the E_F-eV → E_F energy window.

$$I \propto \sum_{E_n=E_F-eV}^{E_F} |\psi_n(0)|^2 \, exp(-2k_{II}d) \tag{2.17}$$

For small applied bias, the density of states can be considered to have little variation within the applied bias window, so we can consider the local density of states (LDOS) at the Fermi energy to recast equation (2.17). The LDOS, $g_E(z,E)$, is defined as the number of electronic states per unit energy for a given position at a given energy, and hence can be written as,

$$g_E(z,E) = \frac{1}{eV} \sum_{E_n=E_F-eV}^{E_F} |\psi_n(z)|^2 \tag{2.18}$$

Recasting equation (2.17), the tunnel current can be considered as,

$$I \propto V g_E(0,E_F) \, exp(-2k_{II}d) \tag{2.19}$$

where $g_E(0,E_F)$ is the LDOS of the tip at the Fermi energy.

Alternatively using the LDOS definition (2.18) and (2.15) the tunnel current can also be written as,

$$I \propto V g_E(d,E_F) \tag{2.20}$$

From this 1D model, both (2.19) and (2.20) clearly indicate that tunnel current depends on a) the tunnelling voltage V, b) tip height, z, c) the local density of states of both the tip and sample and d) the workfunction of the sample imaged. So scanning in the constant current mode enables a LDOS of states map of the region to be built up.

2.3 Experimental Setup

To obtain this tunnelling current the STM tip is approached typically ~1 nm away from the surface, initially by coarse approach motors applying voltages to piezo crystals causing them to expand and contract, as can be seen from equation (2.21).

$$\Delta L = pV\frac{L}{h} \tag{2.21}$$

where ΔL is the length change in a piezo crystal of length L and thickness h following the application of a voltage V and p is the piezoelectric coefficient [16].

To reach these small distances the tip approaches with a 'slip and stick' method. The *z* piezo crystal fully extends, decreasing the tip to sample distance. If the set tunnel current is not detected during this extension, the piezo crystal retracts. The piezo crystals attached to the sample (not shown in Figure 4) then approach by one step. The *z* piezo extension is repeated, and this cycle continues until an extension of the *z* piezo results in the detection of the user specified set tunnelling current. This allows a safe approach to the sample, avoiding crashing, providing that the sample motor step is smaller than the full extension of the piezo crystal.

The STM is typically operated in constant current mode where the current is maintained at a constant user specified value by a feedback loop, controlling piezo motors to move the tip to retain this constant set value.

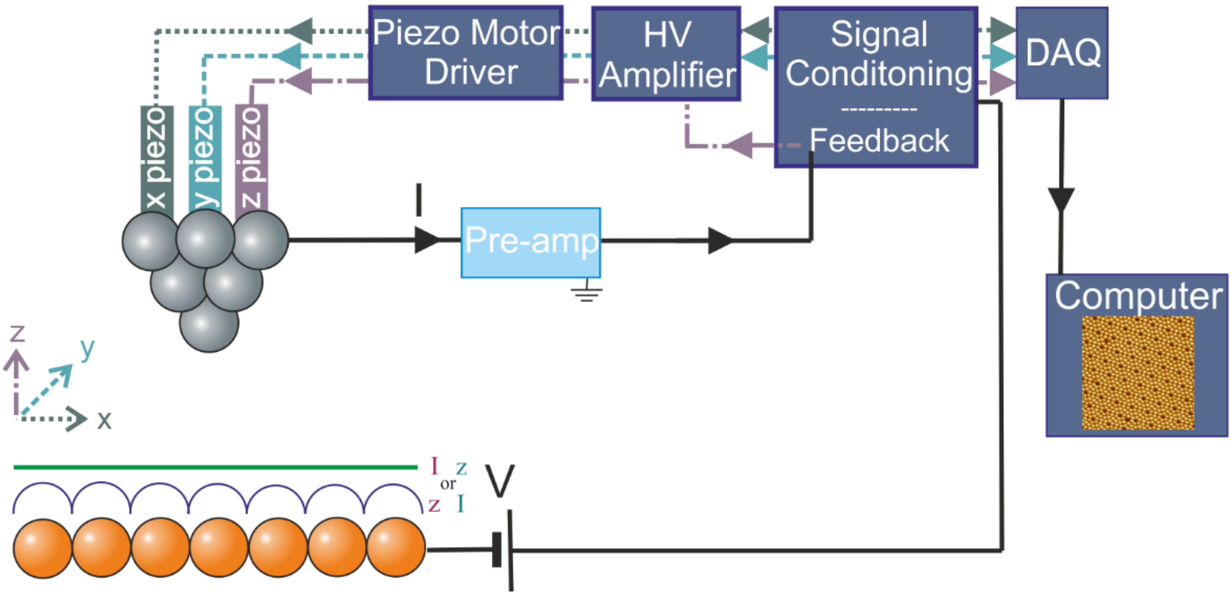

Figure 4: Schematic of the STM operation and electronics setup. Voltage applied to the sample allows a tunnel current to flow between the tip and sample. The current is amplified via the pre-amp and compared to the user specified value by the feedback loop. The z height of the tip is changed by the z piezo to return the current to the specified value. All this data is sent to the computer via a digital-analogue converted to obtain a topographic image of the surface scanned.

A detailed schematic of this process can be seen in Figure 4. In our system, the bias is applied to the sample and the tip is grounded via the preamplifier. The preamplifier amplifies the current, which is passed to the signal conditioning unit where the feedback loop monitors and compares this current to the user specified value. In constant current mode the tip height is then reduced or increased by the *z* piezo motor to increase or decrease the measured tunnelling current respectively, to maintain the constant current value. Similarly, voltages are applied to the *x* and *y* piezos to raster the tip across the surface for scanning. All this information is passed through a digital-analogue converter to the *Nanonis* software on the computer to build a topographic image of the surface. Due to the exponential distance dependence and proportionality to the LDOS the STM can achieve atomic resolution.

Alternatively, constant height mode is a less commonly used imaging mode. In this mode of operation, the current is measured as the tip is rastered across the surface at a fixed height. This can provide rapid scanning of atomically flat surfaces, however, the major disadvantage with this imaging mode is the high risk of a tip crash when surfaces are not atomically flat.

Chapter 3

Atomic Manipulation Overview

The main drive behind this thesis is in the field of Atomic Manipulation. This offers the opportunity to fabricate nanomaterials in a 'bottom-up' fashion, tailoring materials with specific properties. It also allows access to fundamental information within the systems probed, such a charge transport properties and injected charge carrier lifetimes. There are three main ways in which the STM can induce atomic manipulation, documented in this section.

3.1 Mechanical Manipulation

When the STM tip is brought into close proximity with the surface, adsorbed molecules can be pushed and pulled by short range tip-atom interactions to new locations. A schematic of this process is shown in Figure 5A, where the tip approaches above an atom (a-b), so that an attractive van der Waals force between the tip and the atom is strong enough that lateral movement of the tip (c), pulls the atom along the surface. This force however, is not strong enough to overcome the forces between the molecule and the surface and therefore it remains attached [3]. As the tip is retracted from this new position, the atom remains on the surface at its new location (d-e). It is this process that was used to create the IBM nanoadvert by Don Eigler and his team, as seen in Figure 5B [3]. Here Xenon atoms were moved across a nickel(110) surface at 4 K, by increasing the tunnelling current to 160 nA above an atom [3]. This method of manipulation has been achieved with a range of adsorbates, metal atoms such as Ag [17] and Pt [18] and even with molecules such as CO [18] and O_2 [19], although these typically are achieved using low temperature STM machines between 4 – 6 K.

A further example of mechanical manipulation is in the quantum corral, Figure 5C [20]. A Cu(111) surface was used with iron atoms arranged in a ring via mechanical methods, with the tunnel current elevated to 5×10^{-8} A for manipulation. This confined the surface state electrons in the copper within this circular region causing them to scatter off the boundary atoms, giving rise to the standing wave pattern from the interference of these electrons, mimicking that of a particle in a 2D box.

This lateral movement of molecules across the surface can be done using three techniques operating at constant tunnelling current with the tip moving laterally across the surface.

a) Pushing – where the tip approaches close to the adsorbate and repulsive forces cause the adsorbate to jump to a neighbouring site away from the tip. This causes the tip to approach back towards the surface. Here the molecule always remains in front of the tip.
b) Pulling – where an attractive force is experienced and the adsorbate jumps towards the tip causing the tip to retract. Here the molecule is always behind the tip.
c) Sliding – occurs when the tip is closer than in the pulling mode resulting in a stronger attractive force to slide the adsorbate across the surface.

The tip height motion for these cases is illustrated in Figure 6, where the pulling, sliding and pushing can be seen of Cu, Pb atoms and CO molecules respectively. The CO molecule images as a hollow on the surface and hence the tip must retract once the pushing has caused the CO molecule to jump sites. Therefore, an inverted tip height trace is plotted in c) compared to that typically expected for pushing [21].

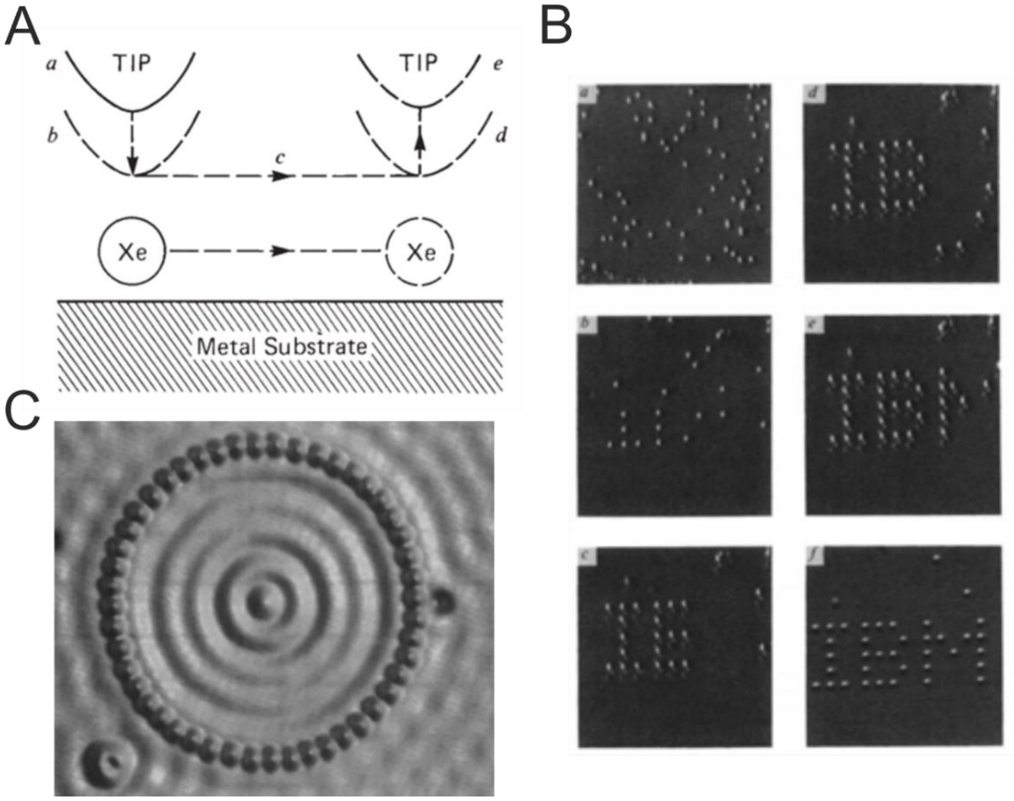

Figure 5: A: Schematic of mechanical manipulation process where the tip approaches above a molecule and attractive forces allow it to be laterally moved across the surface [3]. B: Xenon atoms on a nickel(110) surface mechanically manipulated at 4 K [3]. C: A quantum corral from a ring of iron atoms on a Cu(111) surface [20].

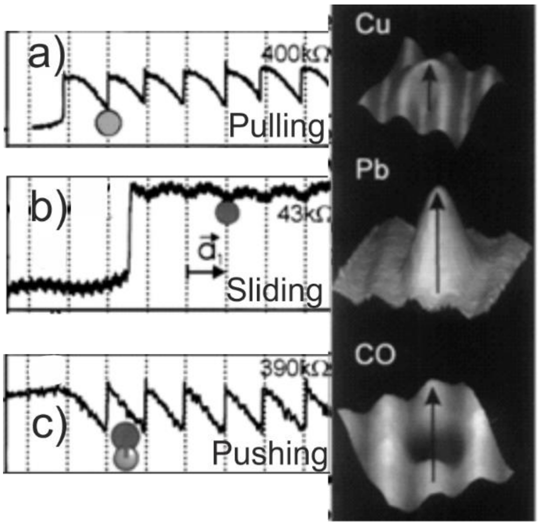

Figure 6: Tip height traces as the tip moves laterally across the surface, to illustrate mechanical manipulation via: a) pulling of a copper atom, b) sliding of a lead atom and c) pushing of a cobalt atom (trace inverted) - adapted from [21].

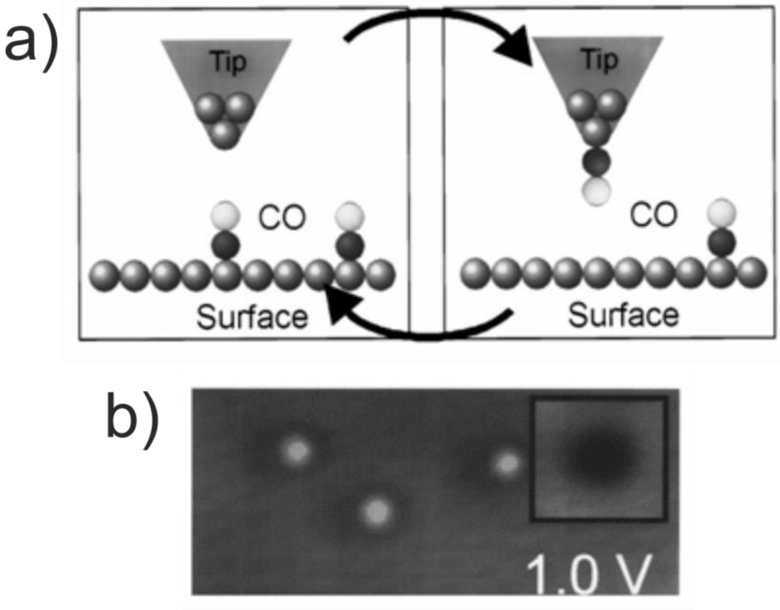

Figure 7: a) Schematic of the lateral mechanical manipulation of a CO molecule on Cu(111). The electric field between the tip and sample is utilised to flip the polar CO molecule. b) STM images illustrating the transfer of the CO molecule. The CO molecule images as an indentation with a bare metal tip (see inset), and as bright protrusions when imaged with a CO molecule at the apex of the tip. [22]

As well as this lateral movement, this manipulation process can also move molecules in a vertical manner, where the adsorbed molecule is attached to the tip and moved to a new location. CO molecules on Cu(111) were transferred by approaching above the CO molecule at 2 V, 1 nA [22]. The feedback loop was switched off and the voltage was ramped to 3 V, before being dropped to 0 V whilst approaching the tip to the molecule. The CO molecule is polar and was required to flip orientation to bond to the tip, therefore the electric field between the tip and sample was utilised to control this orientation change and aid transfer. A schematic of the transfer can be seen in Figure 7.

The process was reversed returning the CO molecule back to the surface in a new location by ramping through negative voltages. The vertical transfer of sample to tip and vice versa was confirmed by the altered STM images, where CO molecules were imaged as depressions with a clean STM tip, but as protrusions with a CO molecule on the apex, seen in Figure 7 [22]. Similar vertical manipulation was achieved with germanium atoms from the Ge(111) surface [23].

Vertical manipulation techniques such as these are used to functionalise STM tips for specific properties as the vertical manipulation results in a known tip apex. A CO functionalised tip [24] and a tip functionalised with an O_2 molecule [25], allowed imaging of intramolecular features unobtainable with a bare tungsten tip, highlighted in Figure 8.

Given that it is the short-range van der Waals forces between the tip and the sample that allow the vertical manipulation to occur, the use of a qPlus STM allows further information of the tip-molecule interaction forces to be gathered [26, 27]. A simultaneous measurement of both STM and non-contact AFM with a tuning fork to measure both the tunnelling current and Δf frequencies were used to deduce forces whilst scanning [28].

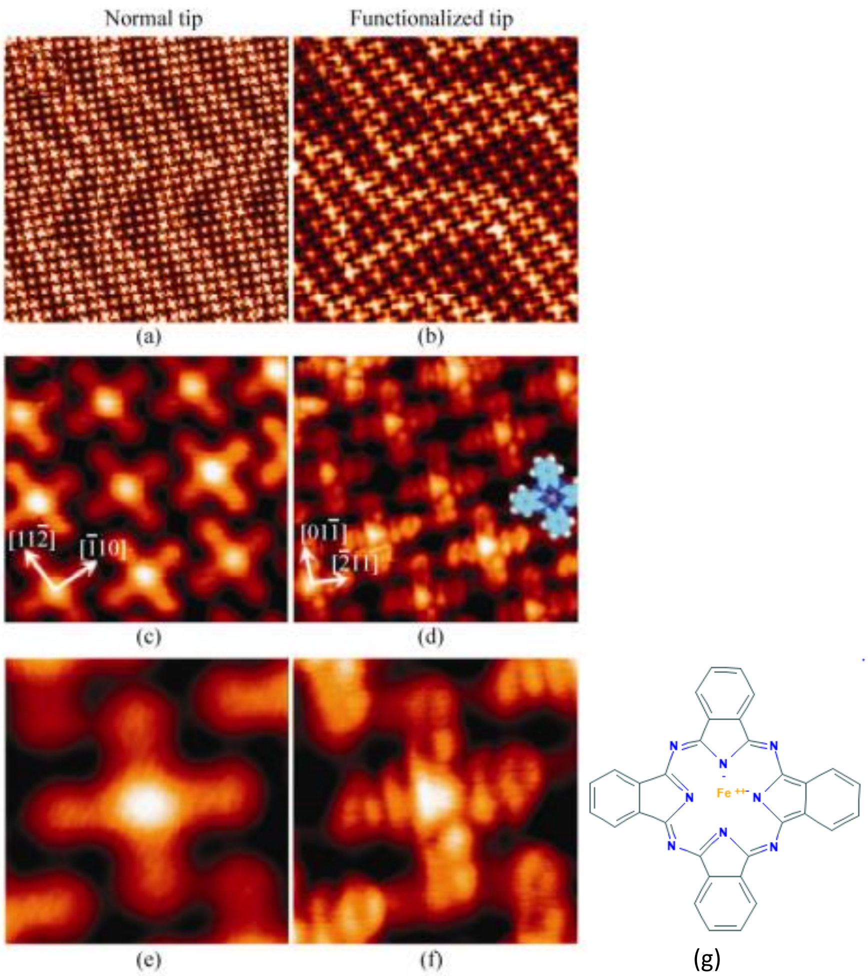

Figure 8: STM images of iron phthalocyanine on Au(111) when imaged with a bare tungsten tip (a, c, and e) compared to an O_2 functionalised tip (b, d and f) revealing detailed intramolecular features not visible prior to functionalisation. A schematic of the iron phthalocyanine molecule is overlaid in d) and shown in (g) [29]. STM image parameters: a: 40 nm x 40 nm, b: 20 nm x 20 nm, c-d: 5 nm x 5 nm, and e-f: 2 nm x 2 nm. Each obtained with -0.4 V and 0.05 nA. [25]

3.2 Electric Field Induced Manipulation

As a voltage is applied between the tip and the sample, a large electric field can build up in the tunnelling gap which interacts with the potential energy of the adsorbate and surface, as can be seen in Figure 9a [31]. Typically, at passive imaging parameters of 1 V and 100 pA, the field strength is of the order $1\text{x}10^9$ Vm^{-1}. The non-uniformity of this electric field E, can induce a potential energy gradient therefore exerting a force on the adsorbate in the radial direction, described by equation (3.1).

$$\frac{dU_E}{dr}\hat{r} \approx -(\mu + \alpha E)\frac{dE}{dr}\,\hat{r} \tag{3.1}$$

where μ is the static dipole moment, αE is the induced dipole moment and U_E is the potential energy with radial distance r [30]. Figure 9 illustrates the effect of the tip induced electric field on the potential energy of the surface in comparison to the potential energy modification of the surface in the mechanical manipulation technique [31].

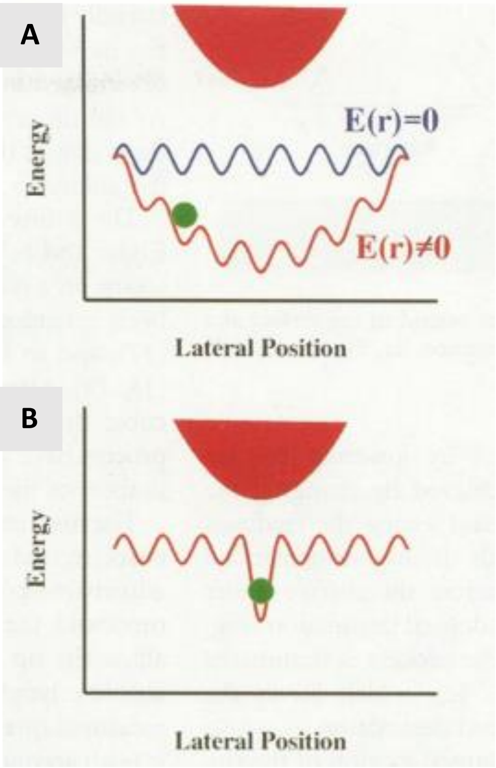

Figure 9: Graph showing the effect of the tip induced electric field ***A,*** *and mechanical manipulation* ***B****, on the potential energy of the surface [31].*

Molecules on the surface that have a dipole can therefore be induced to desorb from this electric field effect. An example of this was seen with the field induced diffusion of caesium (Cs) chains across the GaAs(110) and the InSb(110) surfaces [30]. The Cs atoms formed chains on the surface (seen in Figure 10) and following a pulse of 1 V for 0.35 s, it was shown that the coverage of Cs chains in the region below the tip increased a) – c). The dipole moment of the Cs atoms resulted in the chains moving towards the region of the higher electric field. When larger voltages and longer pulses were used, this effect was seen more dramatically, as shown in Figure 10 d) and e).

A second example of electric field induced manipulation is the controlled direction of CH_3S molecules on the Cu(111) surface [32]. When charge was injected into the centre of the molecule, at voltages greater than or equal to a vibrational excitation mode of the molecule, the molecule was induced to hop to either of the three nearest neighbour sites with equal probability. However, if the STM tip injected into the molecule off centre, then the direction in which the molecule hopped was dependent on the tips voltage. When electrons were injected (negative tip bias), the molecule hopped away from the STM tip, whereas it hopped towards the tip when holes were injected (positive tip bias).

The CH_3S molecule on the surface was negatively charged by charge transfer from the Cu(111), confirming its movement away from a negative STM tip when injecting electrons, and towards a positive STM tip when injecting holes. When the STM tip sits directly above the molecule, it was argued that the electric field could be considered homogeneous from the perspective of the molecule on the surface and therefore no hopping site was preferred in either polarity of voltage [32].

The group have also mimicked this work with CO molecules on a Pd(110) surface, which also transferred charge to the adsorbed molecule, allowing attractive and repulsive movements controlled by the tip bias [32]. Both indicate how the direction of a molecules movements can be controlled from the electric field it experiences, once vibrationally excited enough to undergo hopping.

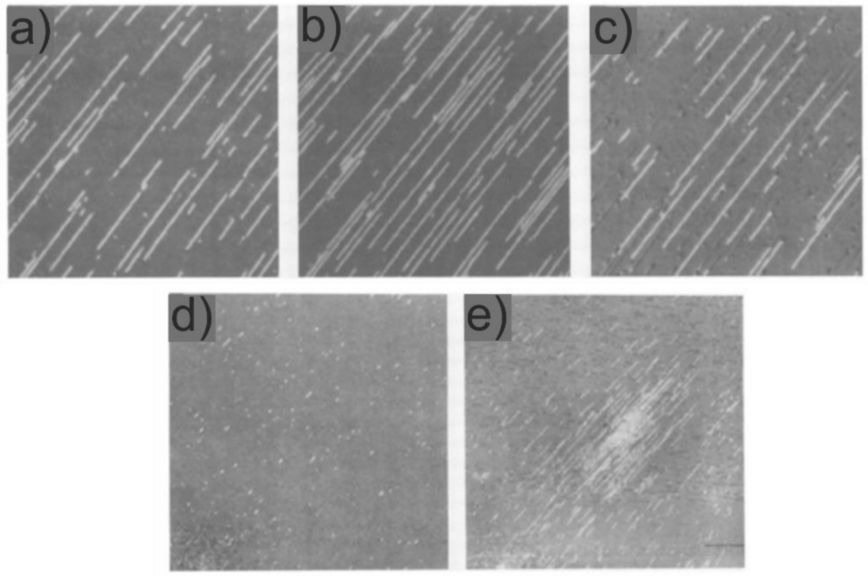

Figure 10: STM image of Cs chains on GaAs(110). a) and b) show before and after a 1 V pulse for 0.35 s, with c) showing the difference between these two images, a)-c) 140 nm x 140 nm. The number and length of Cs chains has increased as the dipole moments of Cs atoms result in the movement of atoms towards the field. d) and e) show before and after images for a larger voltage pulse of 3 V for 0.1 s, where greater numbers of Cs atoms have added to chains forming a dense region where the high electric field was present, d) – e) 350 nm x 350 nm. [30]

Typically, electric field induced manipulation does not occur solely with the electric field but in conjunction with other manipulation methods. As with this example, the CH_3S molecule was first required to be vibrationally excited. Similarly, silicon atoms and clusters were removed from the Si(111)-7x7 surface with the application of voltage pulses and altering the tip-sample distance. However, this utilised chemical forces between the tip and surface at electronic point of contact of the tip with the surface [33]. The close proximity of the tip above a gold Au(111) surface also allowed gold mounds to be deposited from the tip following the application of high bias pulses and hence high electric fields [34].

3.3 Tunnel Current Induced Manipulation

3.3.1 Local Manipulation

A third technique is tunnel current induced manipulation, where the charge injected into the surface from the STM tip results in manipulation events. This is the method used for manipulation in this thesis. Also called inelastic electron tunnelling (IET) where the tunnelling charge loses energy in exciting the molecule to be manipulated [35]. An early example of this was from Stipe *et al.* with the dissociation of oxygen molecules on a Pt(111) surface, as seen in Figure 11 [5]. The STM tip was approached directly above one molecule and a voltage pulse of 0.3 V for 30 ms was applied [5]. The same area was re-imaged in c) under passive parameters of 25 mV and 5 nA, where the oxygen molecule had dissociated into its constituent atoms. A further dissociation was carried out on the second molecule, seen in d) and the drop in tunnel current indicated the instant of dissociation in b) [5]. This dissociation process illustrates that these manipulation events can occur directly below the STM tip, manipulating an individual atom and are categorised as local manipulation.

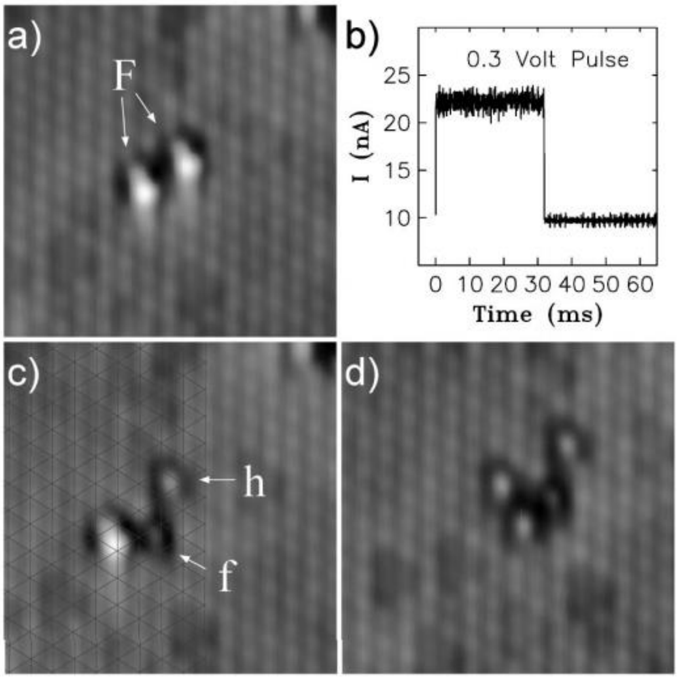

Figure 11: a) Two oxygen molecules adsorbed on the Pt(111) surface. Following a voltage pulse of 0.3 V for 30 s above one molecule a dissociation into its constituent atoms occurs in c). A further pulse above the second molecule induced this to also dissociate d). The drop in tunnelling current in b) indicates the time of the dissociation. Images taken at passive parameters of 25 mV and 5 nA [5].

This tunnel current induced manipulation process occurs via a DIET process: desorption induced by electronic excitation. A tunnelling charge excites the molecule whereby it can be given enough energy to overcome the desorption barrier and leave the surface, providing the lifetime of the excited state survives long enough. More details on the DIET process and models for manipulation are discussed in chapter 6.

The tunnel current has not only been used to manipulate adsorbates on the surface, but also the surface itself. Wilson Ho's group have demonstrated adatom hopping on the Si(111)-7x7 surface when scanning at low temperature with a 3 V pulse above a silicon adatom, see Figure 12 [36]. The 'after' image revealed a bright region adjacent to the injection site, now dark. The centre adatom had hopped to a neighbouring centre adatom, imaging as a bright protrusion and a drop in tunnelling current was used to indicate the time-to-manipulation.

Application of this effective two-state atomic switch was further investigated by Sagisaka *et al.*, where a five-level switching was observed in the tunnel current [37]. This corresponded to: A: the normal adatom, B: the adatom hopping away from the injection site, or C: the adatom hopping towards the injection site. D: shows a second adatom also hopping towards the injection site or E: hopping in an adjacent unit cell. Each of these gave a different tunnel current signature, all shown in Figure 13 [37].

Other outcomes of this tunnel current induced manipulation, (such as: chemical reactions and single molecule chemistry [38], rotation of molecules [74] and isomerization [39]) all utilise the generation of excited states of the adsorbates from the injected charge. Further details of this mechanism and examples of manipulation outcomes are detailed in section 6.1, as this is the basis of the local manipulation work carried out in chapters 6 and 7 of this thesis.

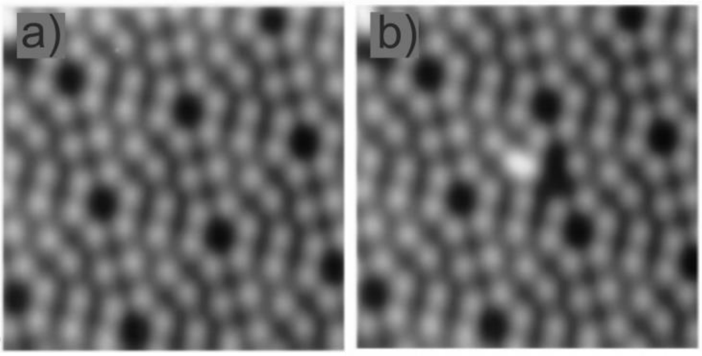

Figure 12: STM images of the Si(111)-7x7 surface a) before and b) after a 3 V pulse above a centre adatom site. b) shows adatom hopping has been induced as the adatom into which charge was injected has hopped onto a neighbouring adatom (imaged as a bright protrusion) and left a dark hollow in its place. [36]

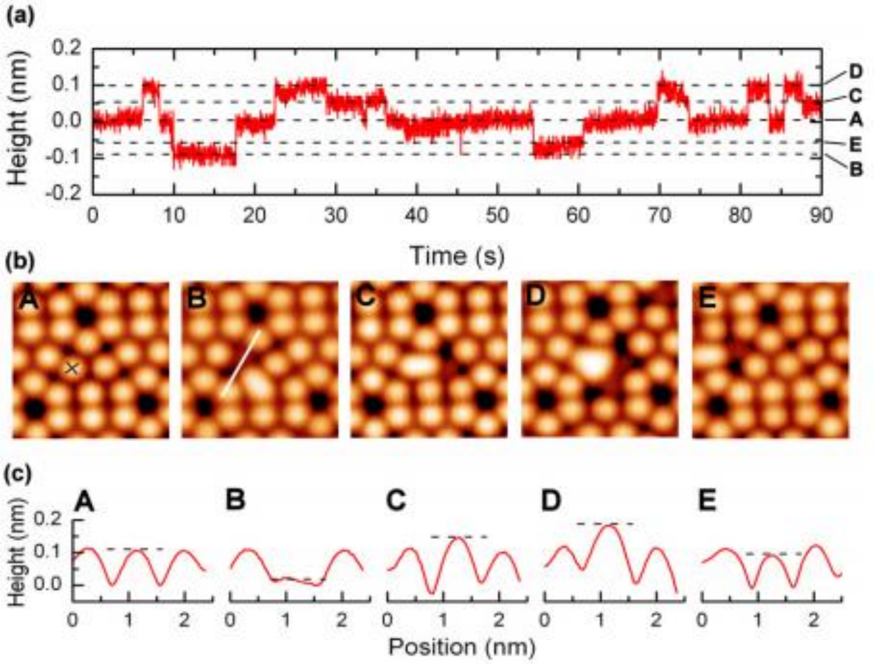

Figure 13: (a) Tip height trace recording different possible adatom hopping states when the tip is located at position 'x' in (b) at 1.8 V and 0.2 nA. (b) shows STM images taken at 1 V and 0.1 nA, illustrating these different states. These states correspond to, A: normal adatom positions, B: adatom hopped away from the injection site, C: adatom hopped towards the injection site, D: a second adatom hopped towards the injection site and E: adatom hopping in an adjacent unit cell. (c) shows the tip height along the white line shown in B for each of the hopping states. [37]

3.3.2 Non-Local Manipulation

Tunnel current induced manipulation does not purely occur on a local scale directly below the tip. Non-local manipulation is a second category of tunnel current induced manipulation where widespread manipulation events are observed at a distance from the injection site of current. This can be clearly seen in Figure 14 [40]. Maksymovych *et al.* worked on a Au(111) surface dosed with CH_3SSCH_3 molecules (along side other noble metal substrates e.g Cu(111)) at low temperature, 5 K [40]. An injection pulse of 2.5 V, 1 nA for 200 ms, was applied at the centre of the image in Figure 14(c), resulting

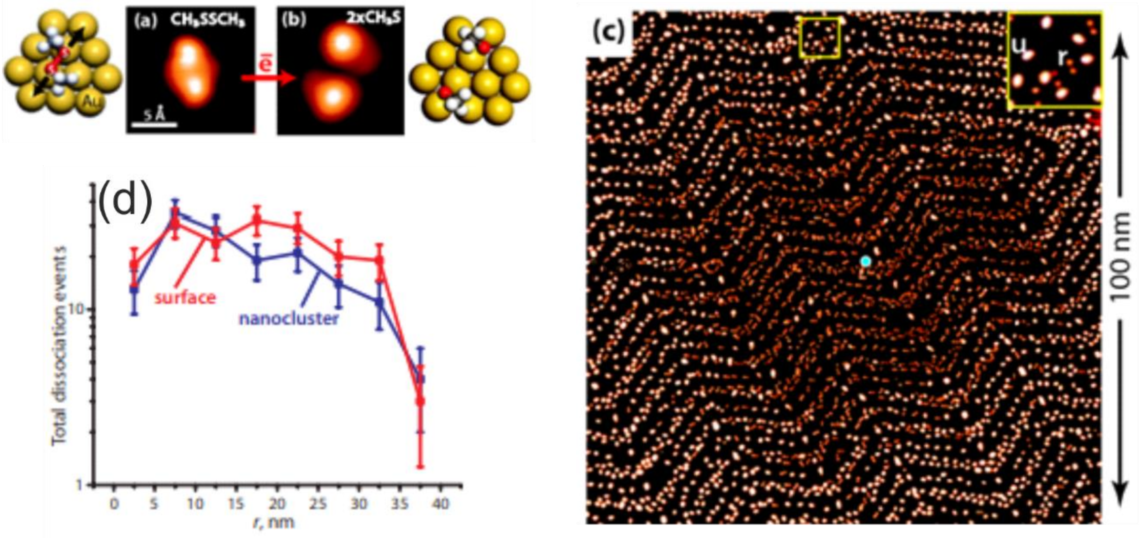

Figure 14: Non-local manipulation of CH_3SSCH_3 on Au(111). (c) shows a region of radius ~46 nm, of manipulated molecules surrounding the injection site marked with a blue dot. The injected charge results in the breaking of the S-S bond of the molecule illustrated in (a) and (b). (d) shows the number of manipulation events as a function of radius for manipulation injection atop a nanocluster, compared to injection on the surface. [40]

in the breaking of the S-S bond of the molecule, indicated in (a) and (b). The image taken following the injection, (c), revealed that dissociation events had occurred within a circular region surrounding the injection site of ~46 nm.

This effect was investigated for a range of voltages with a minimum threshold of 1.4 V required to observe the non-local effect. Larger radii of dissociation, up to 100 nm, were observed for larger voltage injections. The threshold varied depending on the substrate used, suggesting the mechanism for this manipulation was by hot electrons moving across the surface and causing dissociation by 'dissociative electron attachment' [40].

To rule out an electric field effect and tunnelling from multiple tips as non-local causes, the tip was crashed into the surface creating clusters higher than the normal Au surface. An injection was carried out above a cluster meaning that the tip was retracted further from the surface than for normal injection on Au(111). Thus, a reduced electric field and a reduced current would be experienced from this increased distance. However, these cluster injections revealed that the same amount of non-local manipulation was observed. Figure 14(d) shows the total number of dissociation events when injecting above a cluster compared to the normal surface, for a range of voltages. This suggests that it was the hot electrons traversing the surface that was responsible for this distance manipulation, enabling hot electron transport to be studied and to investigate electron induced interaction without the STM tips presence influencing the outcome.

Other non-local outcomes were seen on C_{60} layers on a Si(111)-7x7 substrate [41]. 30 s pulses of -3 V and 0.2 nA induced polymerisation of these C_{60} molecules resulting in a ring formation, shown in Figure 15(a). Polymerisation caused the dark regions and depolymerisation resulted in the bright regions, induced by both electron and hole injection within an energy window. Greater magnitudes of voltage resulted in larger diameter rings, seen in Figure 15(b). It also showed a difference between electron and hole injections, where bias voltage injections of +3 or -3 V generated rings of different diameter, seen in Figure 15(a) and (c).

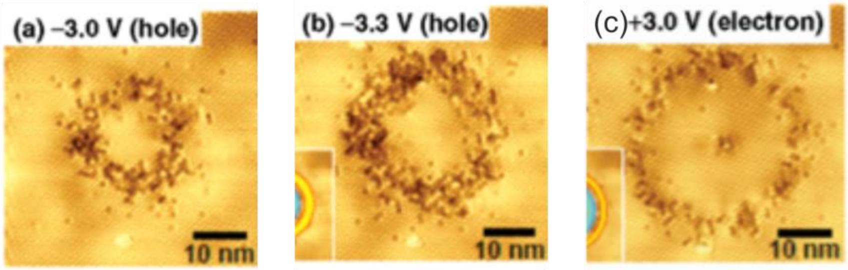

Figure 15: C_{60} on Si(111)-7x7. Following voltage pulse of -3 V and 0.2 nA for 30 s causes polymerisation resulting in a dark ring, this ring is larger for greater magnitude voltages, seen in (b) when compared to (a). (c) shows the polymerisation reaction also occurs for electron injection, but the equivalent magnitude results in a larger diameter ring for electron injection. [41]

This non-local mechanism has been extensively studied by our research group, as the manipulation of aromatic molecules like chlorobenzene and toluene also display non-local behaviour on the Si(111)-7x7 surface [42, 43]. Figure 16A and B show 'before' and 'after' images of the toluene dosed surface following an injection at the site marked '*X*' of -1.9 V, 900 pA for 10 s. An even distribution of toluene molecules (dark spots) is seen in A, and the 'after' image in B reveals a region with a reduced number of dark spots around the injection site marked '*x*'. The graph in Figure 16C shows *$N(r)/N_0(r)$,* the fraction of manipulated molecules, as a function of radial distance from the injection site [43].

At distances larger than 10 nm from the injection site, the data in Figure 16C was fitted with a 2D diffusion model. The parameters involved in this model are shown in Figure 17. The probability per hole of inducing a manipulation event β, increases linearly with more negative voltages. The length scale of diffusive transport λ, displays two distinct values around a -1.5 V threshold. This voltage also corresponds to the 're-setting' of the saw-tooth trend in *R*, the suppression region - the initial distance over which the 2D diffusion model does not effectively fit. This threshold voltage coincides with the onset of a silicon surface state, highlighted in the STS data in Figure 17d. The non-local effect was only apparent with a threshold at -1.2 V, which again corresponds to the onset of a silicon surface state rather than the peak.

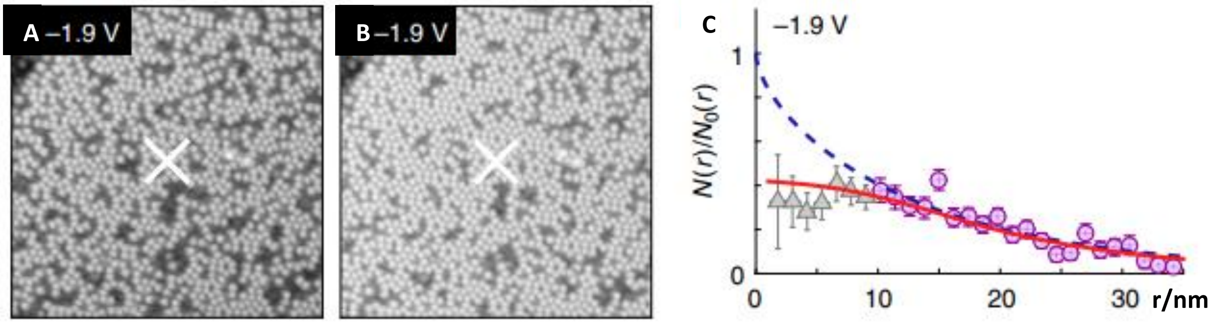

Figure 16: A: Before image of the toluene dosed Si(111)-7x7 surface with an even distribution of dark toluene molecules all over the image. B: After image following an injection at the site marked 'X' with a reduced number of dark spots around the injection site where molecules have non-locally been manipulated. Image parameters: 1 V and 100 pA, 30 nm x 30 nm. C: The fraction of manipulated molecules as a function of the radial distance from the injection site. $N(r)$ is the number of manipulated molecules and $N_0(r)$ is the total number of molecules. The blue dashed line shows a fit to the pink data points with a 2D diffusion model; the red line shows the two-stage fit of inflation followed by 2D diffusion for both the grey and pink points. [43]

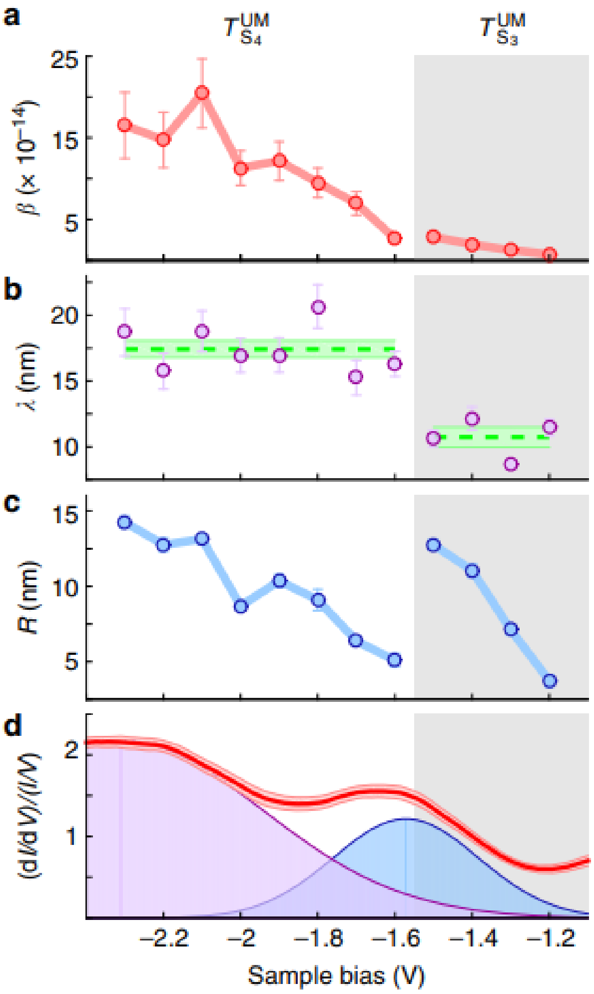

Figure 17: Non-local manipulation model parameters as a function of voltage. a: β, the probability per injected hole of manipulation rises with greater magnitude of voltage. b: λ the 2D diffusion length scale displays two distinct levels. c: R, the suppression region, has a saw-tooth dependence rising with larger magnitudes of voltage and resetting at ~-1.5 V (the same threshold for λ) and corresponding to the onset of a new silicon surface state shown by the STS data in d. [43]

From this, the group concluded that the reduction in manipulation events at distances close to the injection site (< 15 nm), the suppression region, were not occurring due to electric field effects; because at larger voltages the field would increase, yet the *R* parameter displays a saw-tooth tendency. Mechanical methods were also dismissed because the tip would retract further from the surface to maintain a constant current at greater negative voltages. It was proposed that the injected charge undergoes an expansion or 'inflation' before the charge relaxes to the bottom of the surface state into which it has been injected, via scattering events. Here the charge commences a slow 2D diffusion and following this, transitioning from this state can result in manipulation. This results in reduced molecular manipulation directly below the tip to a certain radius of charge expansion, before manipulation is more probable. This has been modelled on data in Figure 16C by the solid red line, where a two-step fit of inflation followed by a 2D diffusion once at a radius of *R*, fits the data extremely well in comparison to a solely diffusion model of the blue dashed line. Further details of this process can be found in [43].

It is this non-local manipulation knowledge that underpins the work carried out in this thesis. Within the context of this proposed mechanism, the single molecule local manipulation is carried out to understand the manipulation process of individual molecules. To further understand and develop this non-local manipulation process, the work documented in chapter 8 investigates light emission from the same Si(111)-7x7 surface.

Chapter 4

Experimental Techniques

Work done in this thesis was carried out on a room temperature Omicron STM 1 housed in a UHV chamber with pressure ~10^{-10} mbar. This chapter will introduce this machine and the methods required for its effective working, including baking and venting. The procedure will be outlined for sample preparation and for tip etching and the steps taken towards obtaining a stable and reliable STM image.

4.1 Omicron STM 1 Layout

The Omicron STM 1 used in this thesis has the layout depicted in Figure 18, where the role of each area of the system is detailed in the sections below.

4.1.1 Load Lock

The load lock (I in Figure 18), is a small volume chamber used for getting samples and tips into and out of vacuum. A 'fast-entry' door seals with a fluorocarbon o-ring to maintain vacuum, while the valve head contains spring copper runners to accept sample and tip holder plates. This section can be pumped by the Turbo Molecular Pump (TMP) from atmosphere providing valve V1 and vent valves (VV) VV1 and VV2 are shut, and V6 and V7 are open. The roughing pump (RP) provides the backing pressure for the TMP and therefore these should always be running simultaneously.

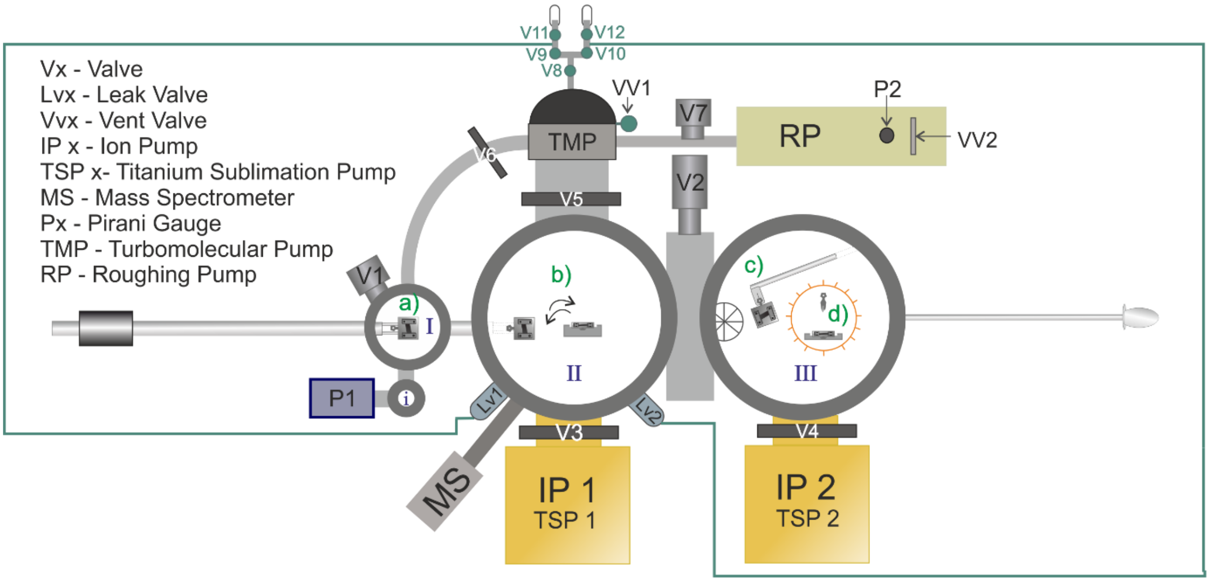

Figure 18: Schematic diagram of the Omicron STM 1 layout used in this thesis.

Attached to the load lock is section i, an extension used for tip flashing which will be explained in detail in section 4.6.1. The pressure of both the load lock and flashing extension is monitored by a Pirani gauge (P1 in Figure 18). Further details of pumps and gauges and the levels of vacuum they achieve can be found in section 4.2.

4.1.2 Preparation Chamber

The 'Prep' Chamber (II in Figure 18), enables all the 'messy' work to be done involving higher pressures, without contaminating the STM chamber itself. Here the samples are cleaned using a sample heater. For silicon, this is direct heating with metal fingers to contact the sample. Indirect heating for tip plates and graphite samples is achieved with a tungsten filament mounted behind the sample plate. Gases can be dosed via the leak valves (LV) LV1 and LV2 each operated by a stepper motor. More details on the sample flashing and dosing processes can be found in section 4.2.

4.1.3 STM Chamber

The heart of this machine, the STM head, consisting of the STM tip and sample are housed in the STM chamber (III in Figure 18). A detailed image of the STM head can be seen in Figure 19. The tip and sample location are highlighted, along with the wires carrying the tunnelling current down to the pre-amplifer and *Nanonis* electronics connected externally underneath this chamber. This helps to minimise any electrical noise in the system.

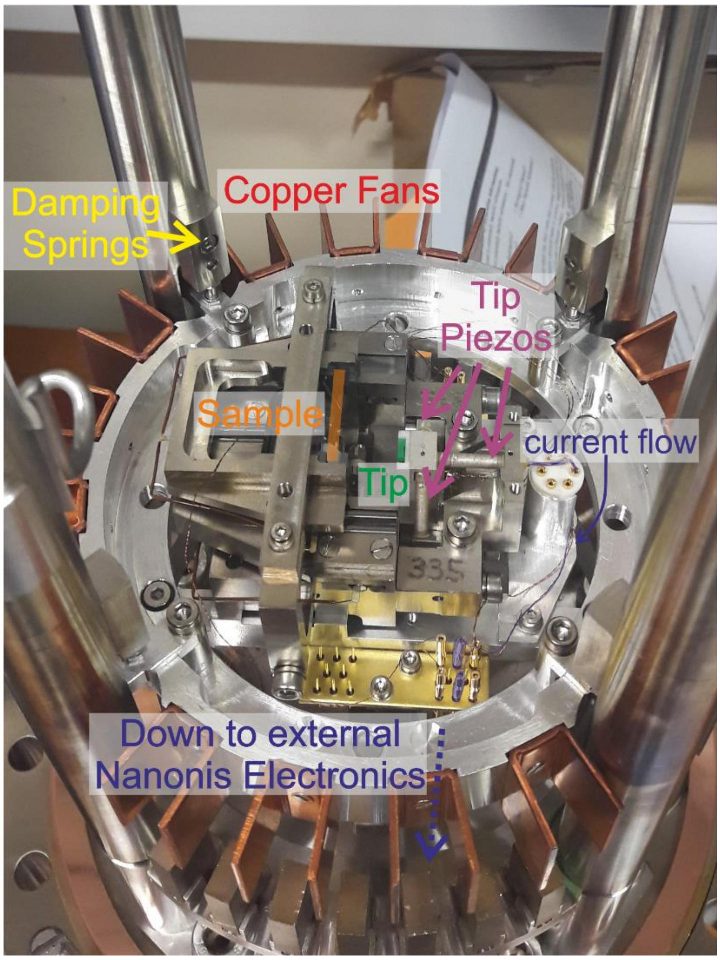

Figure 19: STM head image showing labelled components, the sample holder slot is highlighted in orange and the STM tip slot is highlighted in green. The blue regions highlight the flow of the tunnel current from the tip down to the external Nanonis electronics.

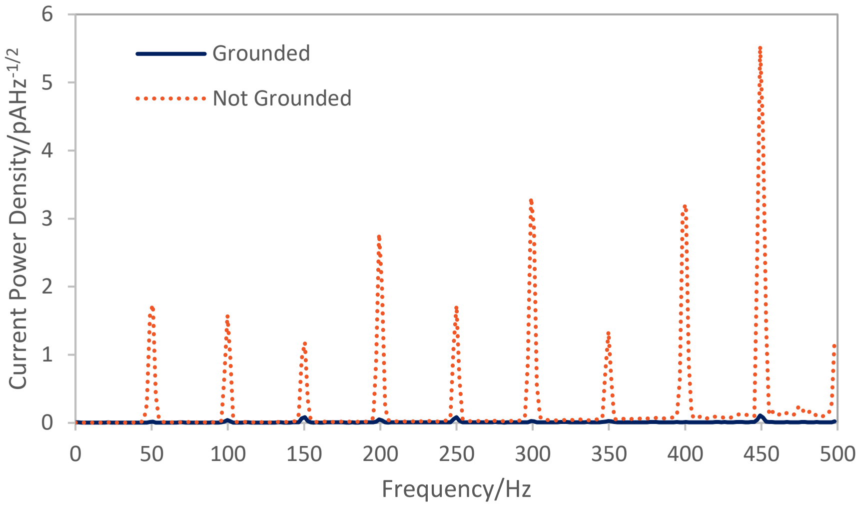

Figure 20: Noise spectrum of the Omicron STM 1 in a grounded and non-grounded state.

Noise is an important factor for an STM scientist working at such small atomic scales. The STM head is attached to four springs with low resonant frequency to dampen any oscillations and hence, it is crucial that the legs of the STM frame are level allowing the STM head to hang freely. The STM head also includes a ring of copper fans (see Figure 19), that slot between mounted permanent magnets. Any movement of the copper fans through this magnetic field induces Eddy currents to oppose the STM head motion. The whole STM frame is then mounted on rubber mats for further damping effect and to decouple the system from external vibrations.

The *Nanonis* electronics used to receive the signal from the STM head are carefully mounted and earthed to minimise noise detected on the spectrum analyser, shown in Figure 20. Regular peaks occur at 50 Hz intervals (typical of mains noise), which are decreased by two orders of magnitude with the careful addition of grounding wires.

4.2 Pressure

To achieve and monitor UHV, a range of pumping stages to intermediate pressures are required. The schematic in Figure 21 illustrates these pressure regions, with the pumps used to achieve them and the gauges required to detect them. These regions of vacuum are highlighted on the STM photo in Figure 22.

4.3 Venting

Bringing the STM system up to atmosphere is a necessity for making changes to the system or carrying out any repairs.

To vent the system, we require that all the chambers are open and connected to each other. Typically the load lock will remain at an atmosphere of nitrogen, as this area is prone to leaks and therefore remains cleaner when filled with nitrogen. To connect the load lock to the prep chamber V6 should be open and the roughing pump is started to build up a backing pressure. When this reaches 5×10^{-2} mbar, V7 is opened and the pressure of the load lock region can be seen to drop on the pirani gauge P1. Once below ~1×10^{-1} mbar, the TMP can be switched on to pump the rest of the system to high vacuum.

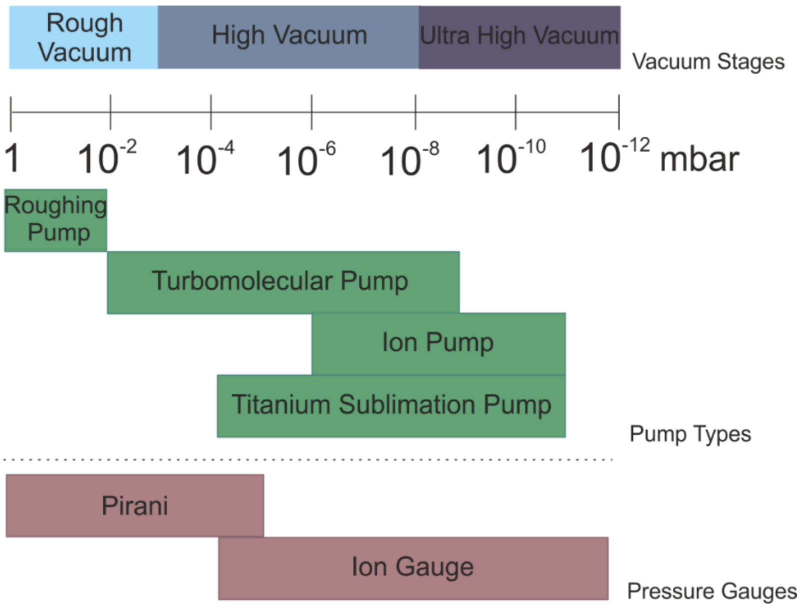

Figure 21: Schematic of the levels of vacuum, with the pumps required to achieve them and the gauges required to measure them.

The load lock typically reaches pressure in the range 10^{-5} to 10^{-6} mbar after an hour of pumping. V1 can then be opened slowly to avoid large pressure spikes in the main chamber. With V2 open, all the chambers are now connected. Next V3 and V4 must be shut. This isolates the ion pumps (IP) so they can remain clean and under vacuum. All STM electronics must be turned off to prevent damage from corona discharge.

Venting occurs through VV1, so the TMP cannot be running. V6 and V7 are shut and the TMP switched off. After allowing 30 minutes for the TMP to slow down, it is vented with nitrogen gas from liquid nitrogen (LN2) through VV1. V6 is slowly opened so the nitrogen gas floods the entire system. Nitrogen is used as it is an inert, light material that is easy to pump away and having no dipole moments does not stick to the walls of the chamber. VV1 should now be shut and VV2 opened to return the roughing pump to atmosphere.

V1, V2, V6 can now be shut to trap the nitrogen in each individual chamber. This minimises the areas of the system exposed to contamination with air when flanges are removed to carry out repairs.

4.4 Baking

Having opened to atmosphere for any repairs, contaminants will have entered the chamber. The most influential being water vapour. As water molecules have a dipole moment, mirror charges can be induced in the metal walls of the STM chamber attracting the water molecules to the surface. This reduces the pressure that can be maintained in the system. To remove this and recover a UHV pressure of 10^{-10} to 10^{-11} mbar, the system must be heated to allow the water to evaporate off the surfaces and be pumped away.

To bake, the UHV system must be pumped solely by the TMP. Following the venting process whilst the load lock is at atmosphere, the quick release load lock must be removed and replaced with a traditional flange viewport as the fluorocarbon seal cannot withstand temperatures within the bake. The chambers must all be connected, so V2 is opened and the same procedure documented in section 4.3 can be followed to pump and open the load lock to connect it to the other two chambers. Once the

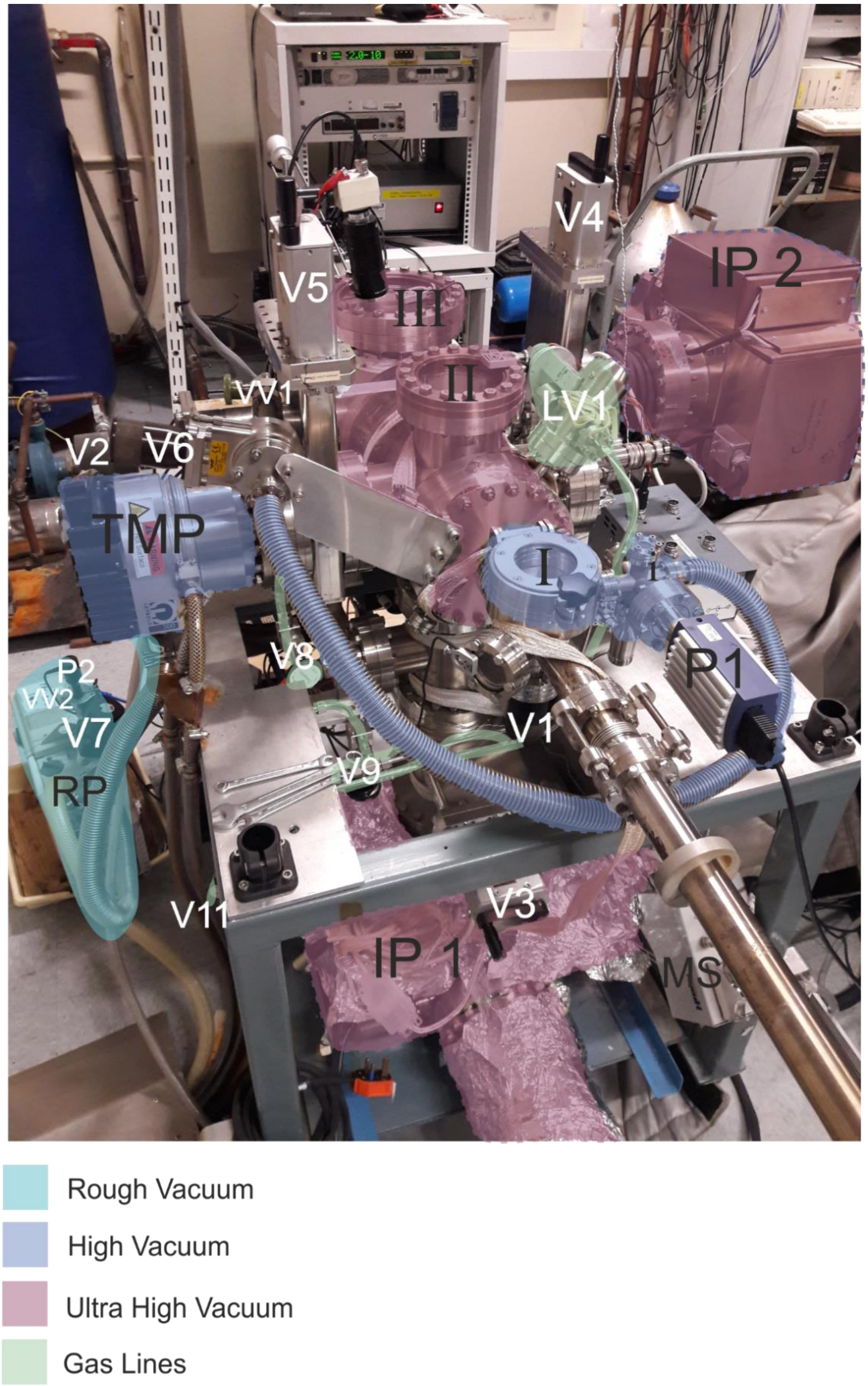

Figure 22: The Omicron STM 1 with regions of vacuum highlighted.

chambers are being pumped by the TMP via the load lock, V5 can be opened for more efficient pumping. V3 and V4 remain shut, and the IPs switched off to avoid damage in the baking process.

The test tubes containing liquid chemicals for dosing molecules are unbolted from the chamber and removed. The gas lines must be pumped down by the TMP to eliminate any remaining gas. Whilst the TMP is running, V8 is opened slowly and the pressure can be watched on P1 as it returns to its normal value. V9 and V10 must each be opened in turn allowing the final stretch of gas line to be evacuated (V11 and 12 remain closed). Stepper motors are removed and each leak valve is opened by half a turn manually to allow for expansion in the bake out.

All STM electronics, power supply connectors, mass spectrometer and P1 are removed and the feedthrough pins grounded using aluminium foil. The sample is removed from the STM head and placed back in the carousel and all the viewports are covered in foil to reflect the heat and prevent any sudden shock to the glass. Finally, all valve handles for V3-5 and V8-10 are removed, the tip approach camera and its electronics are taken off and the transfer arm magnet is slid off and kept outside the bake to prevent de-magnetisation. The inlet funnels and outlet piping for the TSPs are also disconnected.

A final preparation step is to check each of the four thermocouples attached to the STM at strategic locations (such as the STM head base) are working. Using a LabVIEW script, the thermocouples can be tested by placing a warm hand over each in turn and observing the temperature rise.

The STM system is now ready to be covered in a fibre-glass heat shield tent for baking. This holds the heat from ceramic tapes wrapped around the chambers and free-standing ceramic heaters inside the tent. Each tape and ceramic heater is connected via 3-phase power and controlled by a LabVIEW script enabling the bake temperature, its rate of increase and the bake time to be set. The thermocouples are then used to monitor the temperature of the STM system and a feedback loop turns these heaters on and off repeatedly to reach the desired value.

For an ideal bake, all regions of the STM system will increase in temperature at roughly the same rate and to the same temperature, otherwise the contaminants will stick to the cooler regions of the system. Typically our bakes are set to initially increase to 70°C, by 12°C per hour, to prevent any large pressure spikes in the system. Once the pressure has begun to level out, the bake temperature is increased to 120°C and left for roughly three days. A bake cannot exceed 150°C as this would damage the IPs. The bake data collected from LabVIEW is plotted in Figure 23.

The monitored temperatures generally follow the set temperature curve. The Prep Ion Pump curve is lower than all the others as the internal heaters on the Prep IP no longer work, so free-standing ceramic heaters were used to increase the temperature of this lower region of the STM. The temperature was set to increase to 120°C after ~30 hours had elapsed and after ~45 hours the sample heater was removed from the feedback loop to increase the temperature of the whole system. The pressure spike after ~95 hours results from the IPs being turned back on as the pressure had recovered to ~10^{-7} mbar. The whole system was then set to cool at 12°C per hour just before ~110 hours elapse, and the total bake duration here equals 113 hours.

Once cooled to room temperature, the items removed from the system can all be replaced. The internal parts of the STM system, especially the IPs will remain hot, so everything is left to cool for a further 24 hours. The TSPs can then be filled with LN2 and each filament flashed three times each for 60 s. This removes contaminant layers from the filaments and ensures a fresh layer of titanium is sputtered on the walls of the TSP. This should further reduce the pressure of the STM system.

A quadrapole mass spectrometer is attached on an arm from the prep chamber. Figure 24 shows the spectrum obtained before and after baking, with peaks of common contaminants identified. It illustrates that a pressure reduction occurs following a bake by three orders of magnitude and recovers a UHV pressure of 10^{-10} to 10^{-11} mbar.

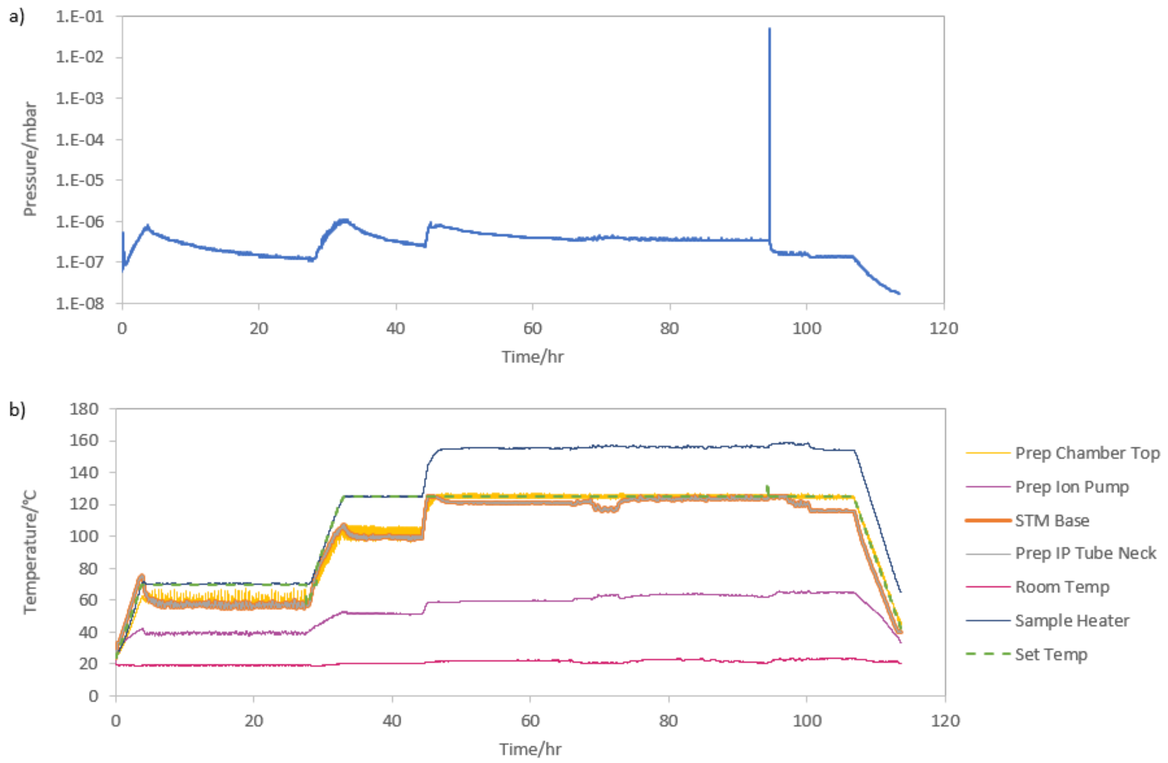

Figure 23: Pressure and temperature data in a) and b) respectively, as a function of the time of the STM bake.

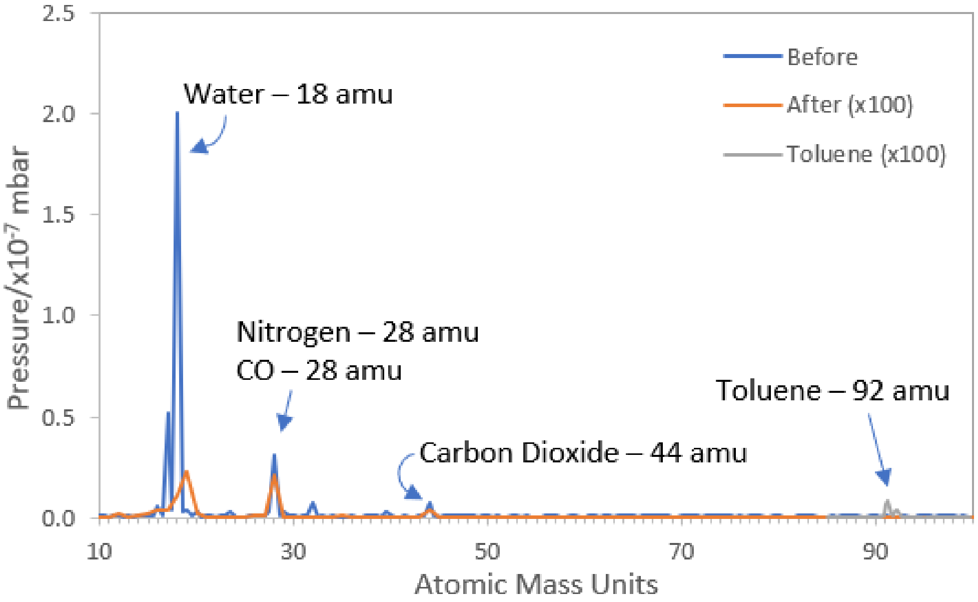

Figure 24: Mass Spectrometer spectrums for the Omicron STM 1 before and after baking and during a dose of toluene gas.

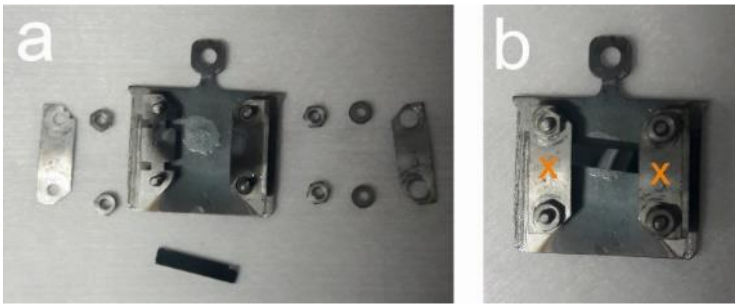

Figure 25: Silicon wafer sample holder. Each component shown in a, and an assembled holder with a wafer shown in b.

4.5 Sample Mounting and Preparation

The Silicon(111)-7x7 surface was mainly used in this thesis. To prepare this for imaging, pre-cut Si(111) wafers (n type, phosphorus doped 0.001-0.002 Ωcm) were mounted on a molybdenum sample holder, as can be seen in Figure 25. Ceramic washers are used to insulate one side of the sample to allow current to be applied for direct resistive heating. Using a multimeter between the orange crosses gives the resistance of the sample, typically 3.5-4 Ω.

The schematic in Figure 18 illustrates how to transfer a sample into the STM head.

a) When the load lock is at atmosphere, the sample holder is slid into the copper runners using tweezers, and the load lock is pumped (see 4.3). When at high vacuum (10^{-5} – 10^{-6} mbar) V1 is opened and the transfer arm pins slot into the valve head. This allows rotation of the transfer arm magnet to lower the hammer and hold the sample plate. The transfer arm and sample are extracted and V1 is shut.
b) The transfer arm moves the sample into the prep chamber and aligns with the sample heater. Twisting the transfer arm releases the hammer, so that it can be withdrawn leaving the sample holder placed in the sample heater. The heater is rotated by 90°.
c) The wobble stick extends into the prep chamber and the jaws clamp around the sample holder tag. The sample can then be lifted from the heater and placed in the carousel holder in the STM chamber, if not needed at present.
d) The wobble stick lifts the sample holder into STM head which can be floated on its springs ready for imaging.

Before the sample can be imaged it must be cleaned, in a commonly documented process [44]. Stage one of the cleaning process is to degas contaminants on the surface. The sample is placed in the sample heater and resistively heated by passing a current through it (typically starting at 0.5 A to 1.5 A) to heat to ~600°C, below the melting point of the SiO_2 layer. It is held at this temperature for a few hours, until the pressure has recovered to ~10^{-9} mbar.

For the Si(111)-7x7 reconstruction, the current applied directly to the sample is calibrated to the sample temperature, in order to heat the sample to ~1200°C and 960°C for flashing and reconstruction respectively. The sample is then flashed multiple times at 1200°C for 10 s, before it is heated to 960°C and slowly cooled to room temperature to allow the Si(111)-7x7 reconstruction to occur. Figure 26 shows data from the automated flashing programme monitoring the flashing current and pressure, initially with a failed flash as a pressure spike exceeds 1×10^{-9} mbar (shaded red). Three 'good' flashes follow (shaded yellow), each with a reduced pressure spike and finally a reconstruction flash cools the sample slowly to allow the Si(111)-7x7 reconstruction to occur (shaded green). When first calibrating a sample, images must be taken to ensure the number of contaminants per unit cell is low (of order 0.03-0.1 per unit cell) verifying the correct flashing and reconstruction parameters.

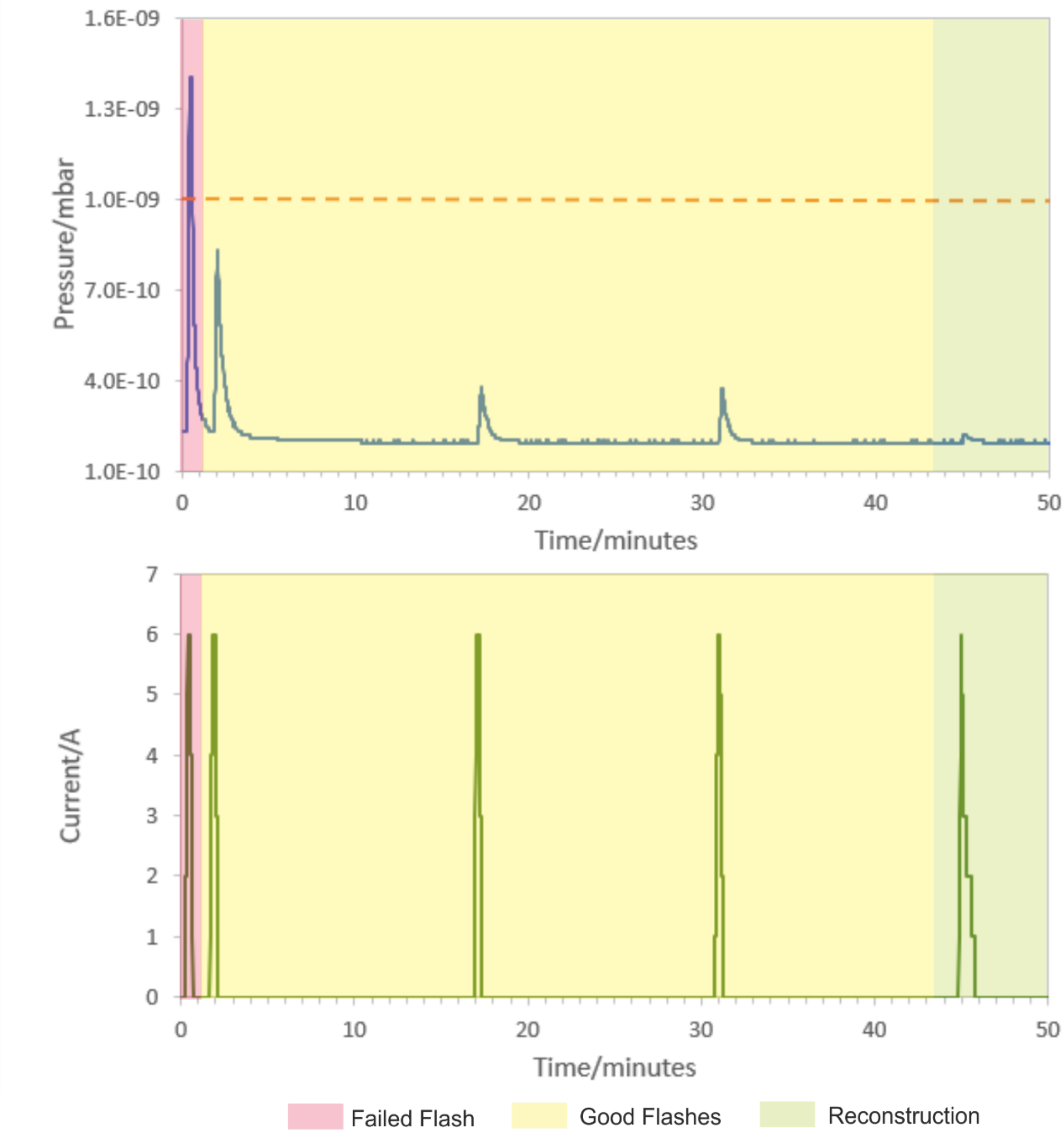

Figure 26: Sample flashing program showing the pressure spikes as a result of direct current heating flashes. A failed flash is highlighted in red as it exceeds 1x10^{-9} mbar, indicated by the dashed line. The yellow region highlights three good flashes, each with a decreasing pressure. The reconstruction with slow cooling from 960˚C is shown in green.

4.6 Tip Preparation

4.6.1 Macro Scale

For stable atomic scale imaging, the ideal tip terminates in an individual atom with a macroscopic apex structure of equal height and base length. Typical tip materials are platinum/iridium, tungsten and silver. Tungsten tips are used in this thesis for their strength, and SEM (scanning electron microscope) images of some used STM tips are shown in Figure 27 a) and b).

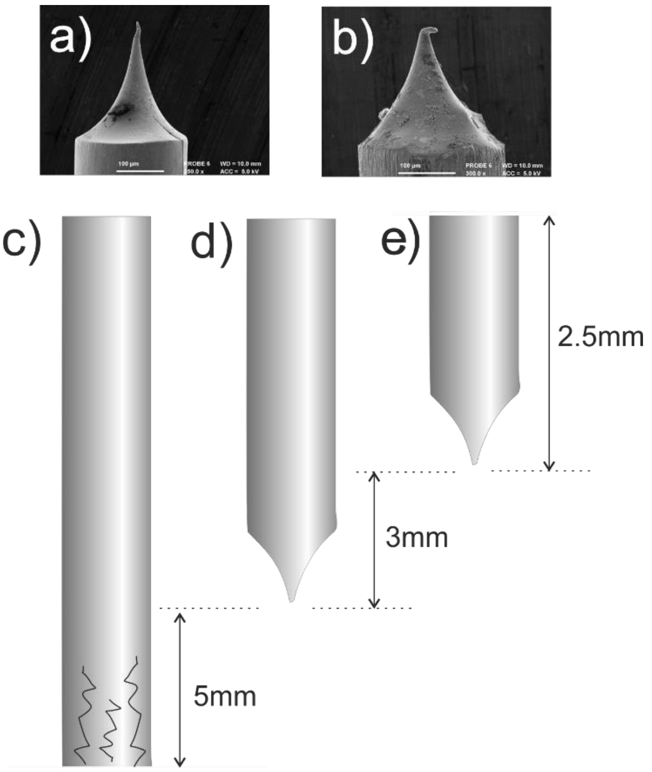

Figure 27: a) and b) show SEM images of STM tips used in this thesis. c) – e) Schematic showing the stages of etching of the tungsten wire.

Tungsten wire 0.25 mm in diameter is fabricated into a tip by chemically etching in 2M sodium hydroxide (NaOH) solution, a schematic in Figure 28 describes the process. The cut wire is lowered into the solution by 5 mm, aligned in the centre of the gold wire ring cathode. An automated LabVIEW programme applies 10 V to the anode and -2 V to the cathode with hydrogen gas bubbling off the cathode ring. The tip is etched at the meniscus where the wire enters the solution, with the flow of WO_4^{2-} hindering etching of the lower submerged region of wire. When the submerged section drops off, a drop in current is detected by LabVIEW which turns off the current, halting further etching. The tip is rinsed in isopropanol and distilled water and submerged by a further 3 mm. This second etch creates the final tip, the first etch being used to remove the fractured section of wire from the cutting process. Following the second etch, a tip roughly 2.5 mm in length is left, illustrated in Figure 27 c) – e). This process is carried out surrounded by a polystyrene box to minimise vibrations of the NaOH liquid and hence meniscus, which can result in a jagged etch. A factor effecting the apex of the etched tip is the length of submerged wire; too long and the etched apex region can stretch under the weight of the lower section and even result in an apex recoil once drop-off occurs. A second factor is the cut-off current trigger. If the trigger is set too high, etching halts before the lower section had dropped off. If set too low, etching will continue even after the lower section drops off and results in a blunt tip. [16, 45, 46]

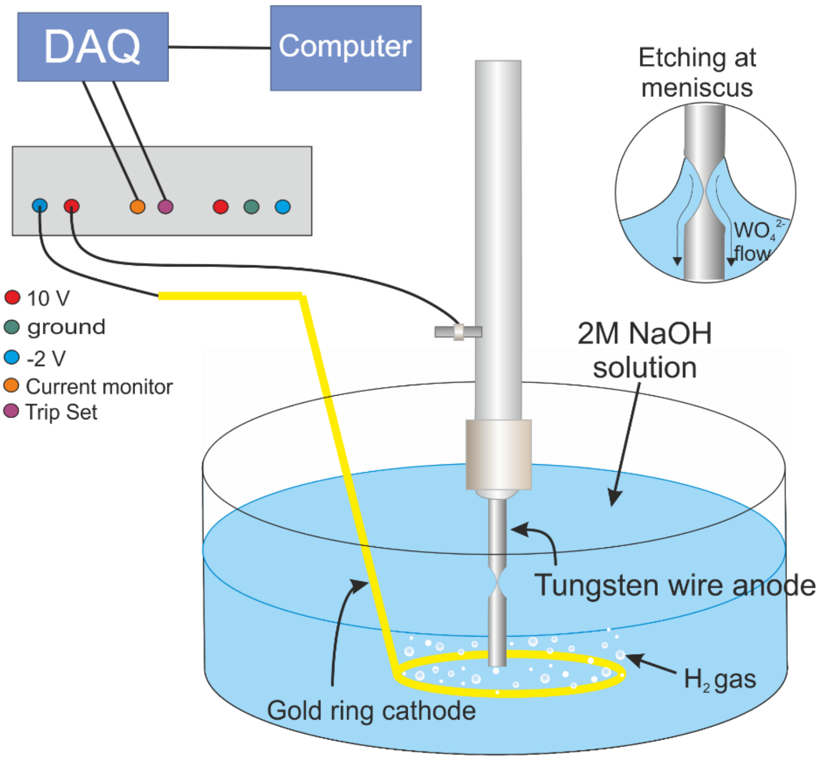

Figure 28: Schematic of the electrochemical etching process to etch tungsten tips, inset shows etching at the meniscus.

The chemical reactions occurring in etching are shown below [16]:

$$\text{Cathode:} \quad 6H_2O + 6e^- \rightarrow 3H_2 + 6OH^- \tag{4.1}$$

$$\text{Anode:} \quad W + 8OH^- \rightarrow WO_4^{2-} + 4H_2O + 6e^- \tag{4.2}$$

$$\text{Overall:} \quad W + 2OH^- + 2H_2O \rightarrow WO_4^{2-} + 3H_2 \tag{4.3}$$

A tungsten oxide layer builds up as a result of etching, which is removed by resistive heating, described by the reaction equation:

$$2WO_3 + W \rightarrow 3WO_2 \tag{4.4}$$

The etched tip is mounted in a ‘flashing station’ and a tungsten crossbar of greater thickness makes contact to it, see Figure 29a). This is attached at region i of the STM chamber (see Figure 18) and once the load lock region is pumped (10^{-5} to 10^{-6} mbar), a LabVIEW programme is used to pass current across the tip for 3 s flashes, until the tip glows ‘bright orange’. It is then baked at a lower current with a ‘dull red’ colour for a further 20 to 30 mins. Typically, 5 to 6 A for flashing and 2 to 3 A for a bake.

For use, the tip must be mounted in a tip holder (see Figure 29 b)), so the load lock is vented and the flashing station is removed. The tip holder and tools used are all cleaned in isopropanol in an ultrasonicator before touching the cleaned tip. The tip is delicately dropped into the holder and clamped in position. The tip holder slides into a tip mount plate (Figure 29 c)) before being taken into the STM using the same methods described in 4.5.

Once the tip holder is placed in the carousel, the wobble stick is used to delicately remove the tip from its mount and slot it into place on the STM head, highlighted in green in Figure 19.

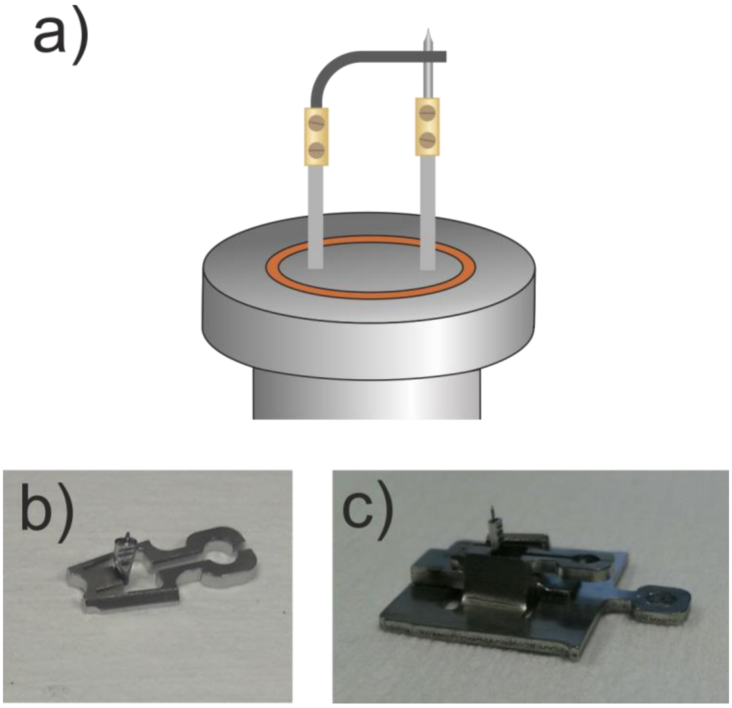

Figure 29: a) Schematic of the tip flashing station used to remove the tungsten oxide from the tip. b) shows a mounted tip and c) shows the mounted tip in a tip plate for transfer into UHV.

4.6.2 Micro Scale

Achieving atomic resolution images can be exceedingly difficult and require multiple tips before one has suitable atomic imaging capability. Once rough atomic resolution is achieved, there are some techniques in order to improve the tip imaging quality [47, 48]:

a) Scanning at negative bias above the work function of the silicon (-4 V) can rip silicon atoms up from the sample surface and rebuild the micro structure of the tip apex, aiming to terminate in a single atom. This technique can be useful when the present tip termination is not the correct state (Figure 30a-c), or if the tip is unstable and repeatedly changing state during imaging (Figure 30d-e).

b) Scanning at positive bias (+4 V) can deposit tungsten or other contaminants from the tip onto the surface. This is particularly useful when bright white contaminants are deposited on the surface during imaging, see Figure 30h.

c) Voltage pulses, at either polarity, can nudge the terminating atoms enough to create a stable image. Useful when the tip state keeps changing, see Figure 30g.

d) As a last resort, the sample voltage can be passed through zero volts initiating a tip crash, or in extreme cases, steps into the sample can be forced. This can be used to knock off insulating material from the tip apex when atomic scale images can only be seen at elevated voltages and not at the usual 1 V, 100 pA passive parameters.

e) Further steps to improve image quality do not directly involve the tip apex, but the feedback loop maintaining the responsiveness of the tip to changing tunnelling current. A feedback loop that is too slow smooths out features on the surface. Increasing the feedback loop (by decreasing the time constant or increasing the proportional gain) enables the piezos moving the position of the tip to react faster to changes in the tunnelling current. However, if set too fast, the tip rapidly retracts and approaches the sample repeatedly in a bouncing motion (the ‘sewing machine’ mode), see Figure 30i.

An ideal, stable, atomic resolution image is shown in Figure 30l). Figure 30j) – k) show piezo creep at the top of each image, corrected for using drift compensation described later in section 5.2.

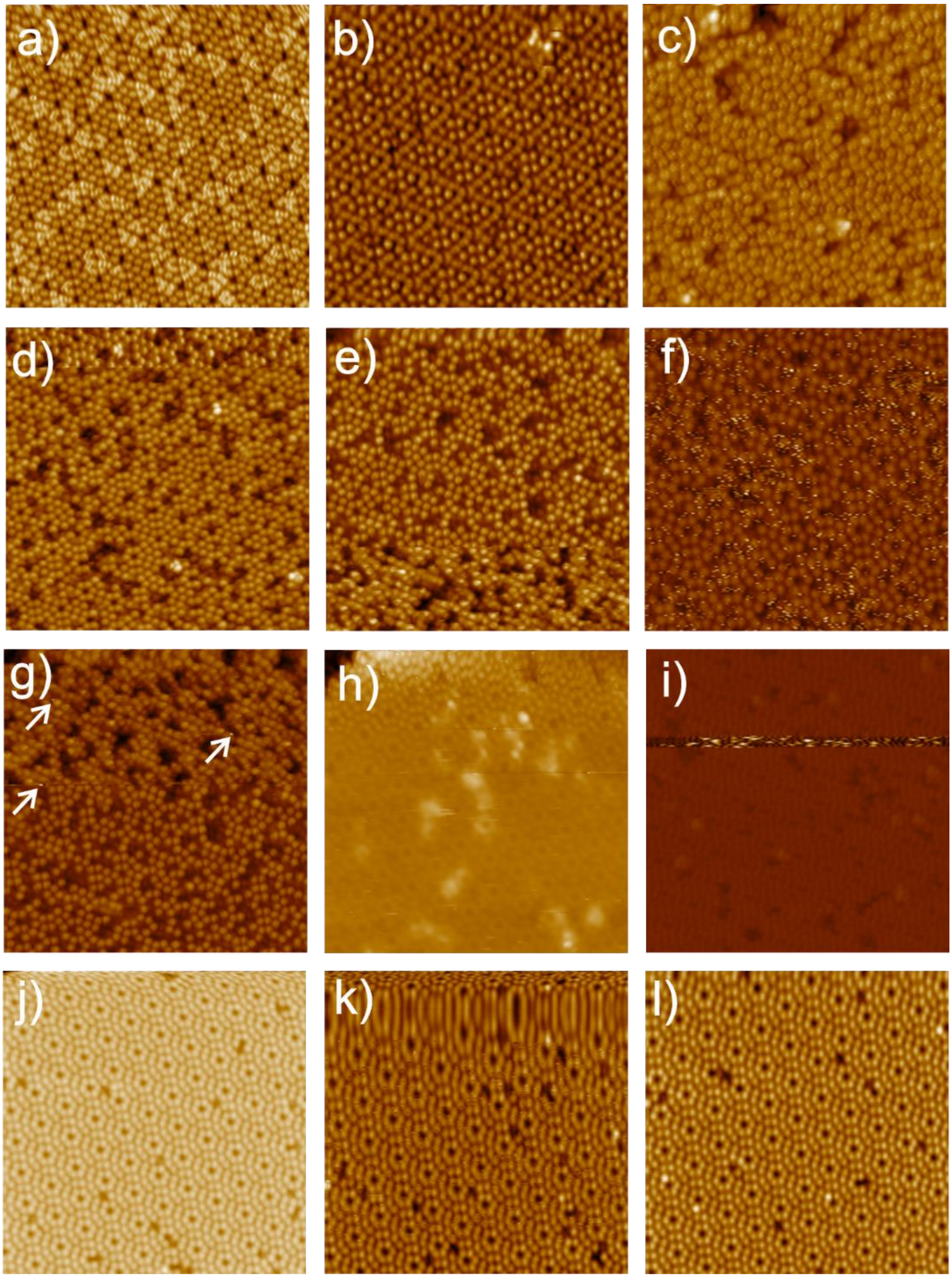

Figure 30: Example STM images of the Si(111)-7x7 surface, each 25 nm in size. a-c: Different tip states, d-e: changing tip states, f: noisy STM image, g: pulses indicated by the arrows to return to a stable imaging tip, h: deposits from high voltage imaging, i) bouncing motion from a feedback loop set too fast, j-k: piezo creep at the top of each image from movement of the scan window and l: a stable image after drift tracking.

4.7 Gas Dosing

Before gas dosing, it must be ensured that the sample flashing and imaging processes do not result in contaminants on the surface, as these also image as dark spots. The silicon surface is scanned and the 25 nm image typically has a contaminant level between 0.03-0.1 contaminants per unit cell.

Toluene molecules are manipulated in this thesis, which also require cleaning to ensure that dosing only releases pure toluene into the system. Liquid toluene is syringed into a test tube which is clamped onto the STM, but contaminants can be dissolved into this liquid and the 'freeze-pump-thaw' method is used to purify the solution, illustrated in Figure 31. For this process the TMP must be running with V8 and V9 open to pump down the remaining gas line.

1) A cup of LN2 and a cup of luke-warm water are poured, being careful to handle the LN2 with cold shield gloves.
2) The toluene test tube is dunked repeatedly into LN2 until it turns cloudy and frozen.
3) V11 is opened slowly to pump the gas in the remaining section of the test tube, and then shut again.
4) The test tube is dunked in the water to begin melting the frozen toluene. Due to Henry's law and different partial pressure, the dissolved contaminant gases bubble out from the toluene solution.
5) The process is repeated, freezing the toluene to enable the newly released contaminant gas to be pumped away. This cycle is repeated until no more bubbles are released from the toluene solution.
6) To verify the toluene purity, gas can be dosed into the prep chamber via the leak valve LV1. For this to happen V6 and V7 must be shut and the TMP turned off and vented as in section 4.3. V11 can be opened to release toluene gas vapour into the gas line before stepper motors are opened to release toluene gas into the chamber, controlled by a LabVIEW code. The mass spectrometer detection of toluene is show in Figure 24.

A typical dose for manipulation is 0.8 L at a pressure of $5x10^{-9}$ mbar, which can be seen from Figure 32b, where the dark spots are toluene molecules and the bright spots are silicon atoms. The image was taken at 1 V and 100 pA.

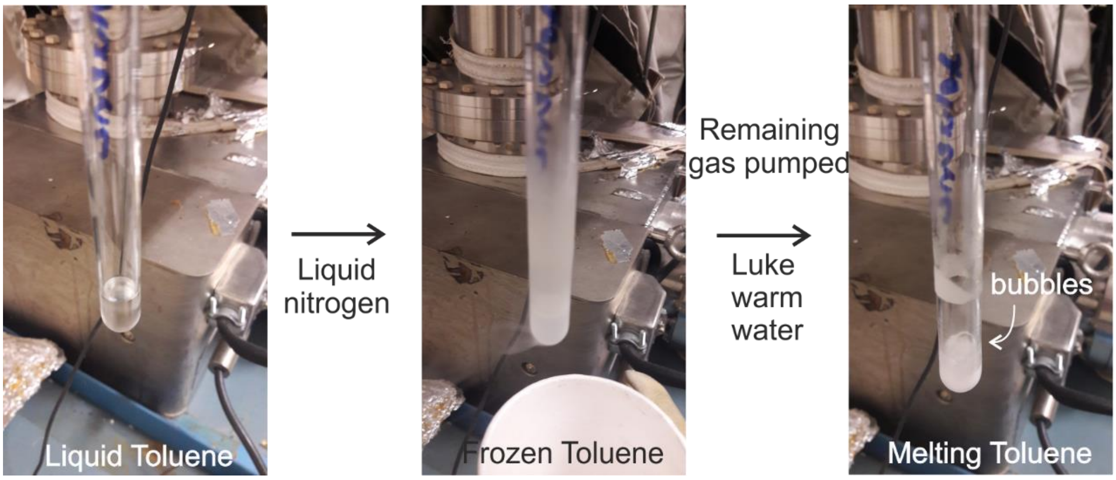

Figure 31: Freeze-Pump-Thaw process for cleaning toluene liquid prior to dosing the surface.

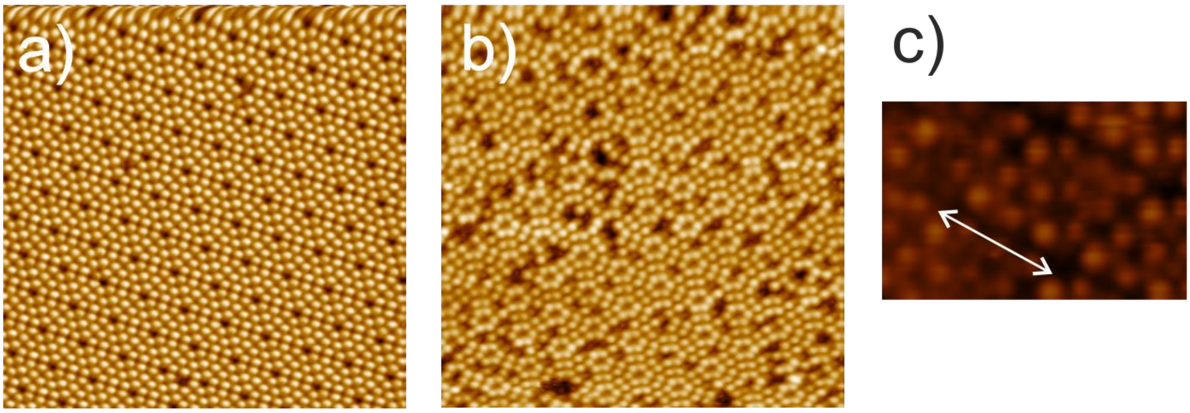

Figure 32: 25nm STM images of clean Si(111)-7x7, a), and of this surface dosed with toluene molecules b). c) Silicon surface imaged at -1 V, 100 pA to identify the faulted and unfaulted half of the unit cell. Arrow highlights the edge of the unit cell, 2.69 nm for scale.

4.8 Silicon Surface

4.8.1 Surface Reconstruction

To obtain a Si(111)-7x7 reconstruction the bulk crystal is cleaved along the (111) plane. This leaves new 'surface' atoms without their favoured number of nearest neighbour atoms (4 in bulk silicon), resulting in a high density of unsaturated dangling bonds which is energetically unfavourable. Consequently, the top layer of the crystal re-orientates to form a new atomic structure in order to minimise its surface energy, with the unit cell reducing from 49 to 19 dangling bonds. The new reconstructed unit cell is formed from 7x7 unit cells of the bulk silicon 1x1 primitive unit cell. [49, 50]

The Si(111)-7x7 reconstruction is illustrated in Figure 33, and is best described by the 'dimer-adatom-stacking-fault' model (DAS) [51]. The unit cell consists of 12 adatoms on the upper most layer, saturating 36 dangling bonds in the layer below. The second layer contains 6 rest atoms each with a remaining unsaturated dangling bond. The third layer is formed from 9 dimers around the outside of the unit cell. The unit cell contains one corner hole, a vacancy in the three surface reconstruction layers. Between the third and the fourth layer of the unit cell is a stacking fault, resulting in the unit cell being split into two triangular halves: faulted and unfaulted. Here the unfaulted half aligns with Si(111) bulk beneath, whereas the faulted half is shifted slightly (60° rotation) [52]. Each half of the unit cell can be identified with a -1 V image as seen in Figure 32c), as the faulted half has a higher charge density so images brighter than the unfaulted half [53]. [49, 50]

Each of the 12 adatoms in the unit cell are identified by the schematic in Figure 34. From Figure 32c), it can also be seen that the -1 V image results in brighter corner adatoms on both halves of the unit cell. These corner adatoms have a higher charge density and charge is transferred from the middle adatom sites [53].

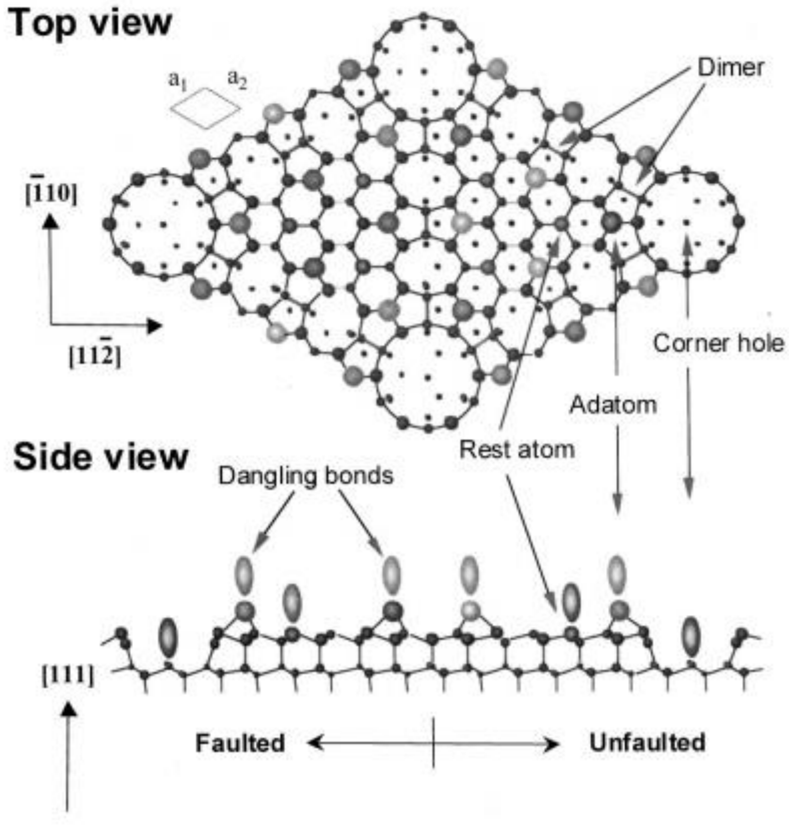

Figure 33: Schematic of the top and side view of the Si(111)-7x7 unit cell, from [54].

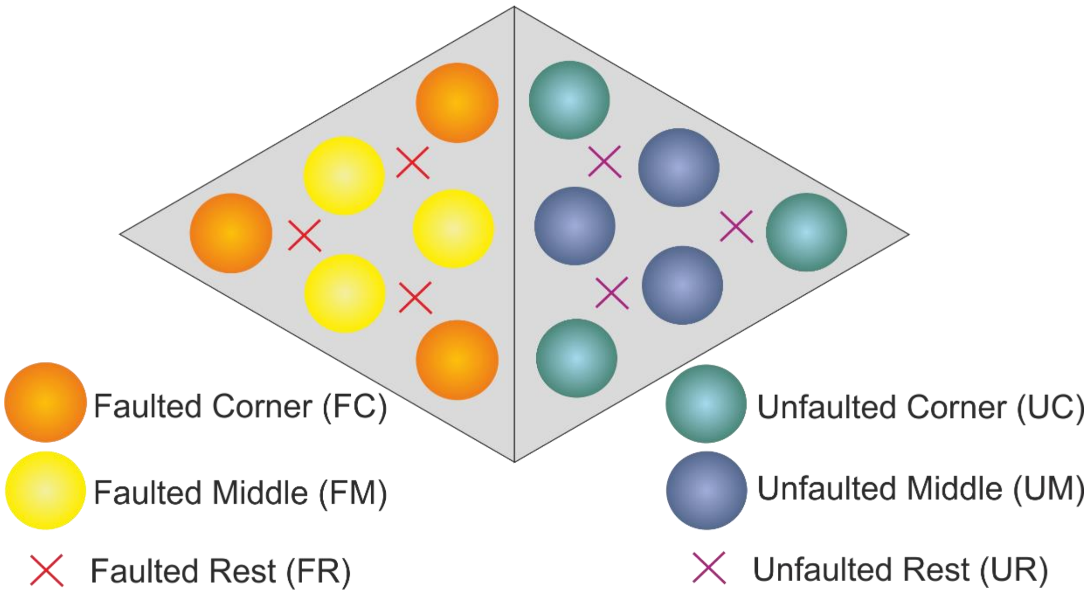

Figure 34: Schematic of the Si(111)-7x7 unit cell with adatoms labelled with circles and rest atoms labelled with crosses.

4.8.2 Electronic Structure

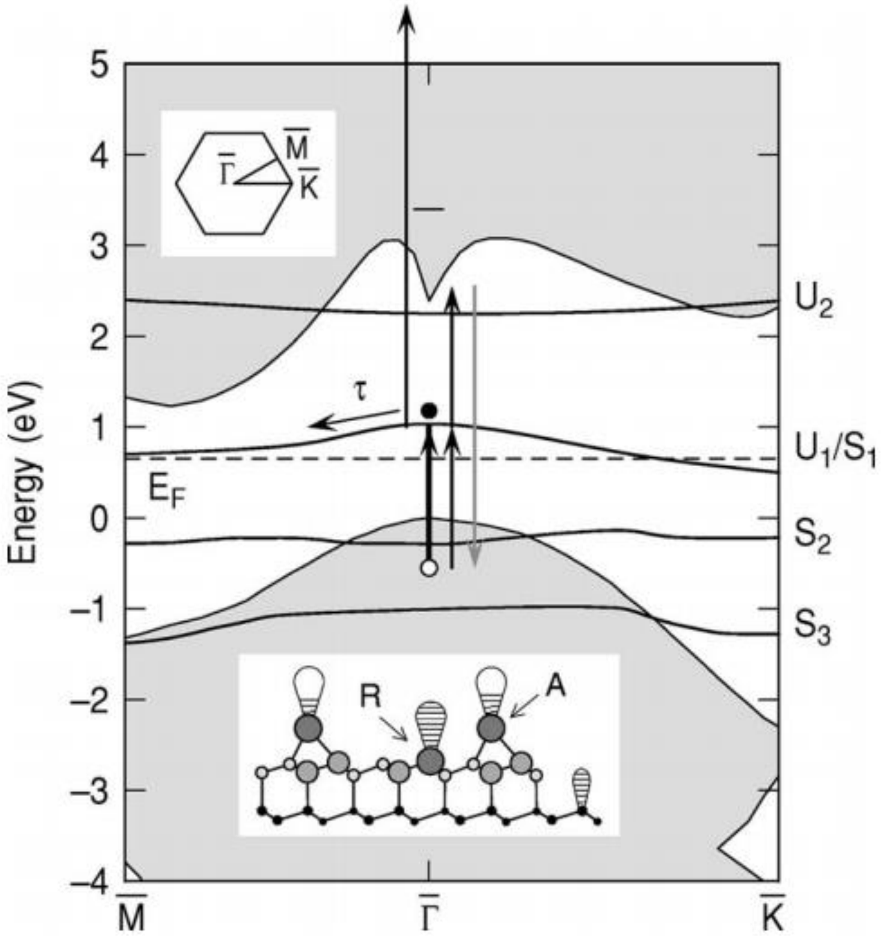

Figure 35: Electronic structure of Si(111)-7x7. U_x states denote unfilled surface states, and S_x states denote filled surface states. The shaded regions are the projected bulk bands. E_F shows the pinned Fermi energy with the energy measured with respect to the valence band maximum. The inset shows a side view of the Si(111)-7x7 reconstruction with a filled rest atom dangling bond and 5/12^{ths} filled adatom dangling bonds [13].

The electronic structure of the Si(111)-7x7 reconstruction is shown in Figure 35 [13]. Si(111)-7x7 is metallic owing to the partially filled surface state U_1/S_1 that crosses the Fermi energy. This results from the 12 adatoms in the unit cell donating seven electrons, six to the rest atoms and one to the corner hole. This leaves five electrons on the remaining 12 adatoms, each being 5/12 saturated, as seen in the inset of Figure 35 [13]. The S_x labelled states are filled surface states, and the U_x labelled states are unfilled surface states. S_2 corresponds to the saturated rest atom dangling bonds and S_3 and U_2 correspond to the saturated and unsaturated back bonds of the adatoms in the underlying layer respectively [13]. The shaded region shows the bulk projected states and a degenerate surface resonance exists when a surface state crosses into this bulk band projection. These surface states are imaged in Figure 36 at their corresponding voltages [55].

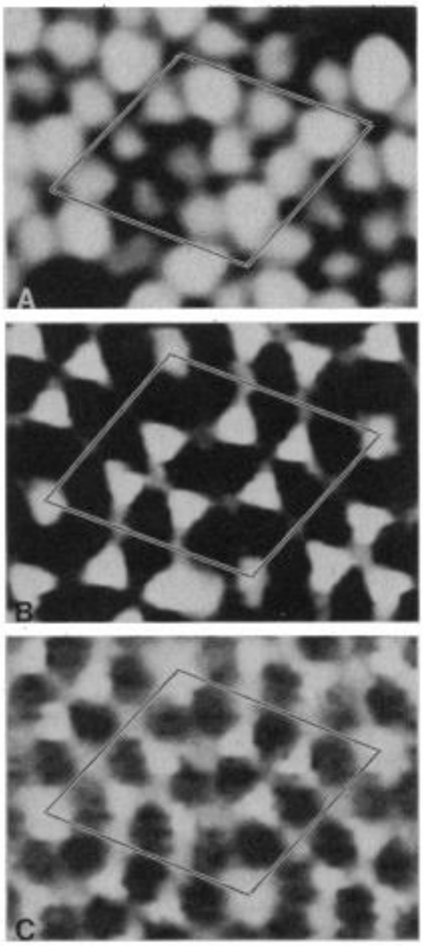

Figure 36: STM images obtained at A: -0.35 V, corresponding to the U_1/S_1 state, B: -0.8 V, corresponding to the S_2 saturated rest atom state and C: -1.7 V corresponding to the U_2/S_3 state from the adatom back bonds (each voltage is measured with respect to E_F) [55].

The existence of a state at the Fermi energy results in the Fermi level being pinned at ~0.65 eV [13,56]. The samples used in this thesis are n-type doped, meaning within the bulk, phosphor donor atoms situated below the conduction band minimum can donate electrons to the conduction band. The bulk silicon Fermi energy is therefore considerably higher than the Fermi energy of the surface due to the half-filled surface state. Consequently, at the near-surface region where the bulk and surface electronic structures are in 'contact' there is a mismatch in the Fermi level. To compensate for this, electrons are transferred from the higher lying level of the bulk, to the lower lying surface level until the Fermi level of the bulk and surface state are in equilibrium, pinning the Fermi energy. This resulting accumulation of negative charge at the surface and positive charge in the near-surface region gives rise to an electrostatic potential. This repels further electrons being transferred from the bulk to the surface, requiring energy for this movement and resulting in band bending in an upwards direction. This is illustrated in a schematic in Figure 37, with the mismatch between Fermi levels shown in a) and the resultant band bending in b). This Fermi-level pinning occurs regardless of the density of bulk dopants [57, 58].

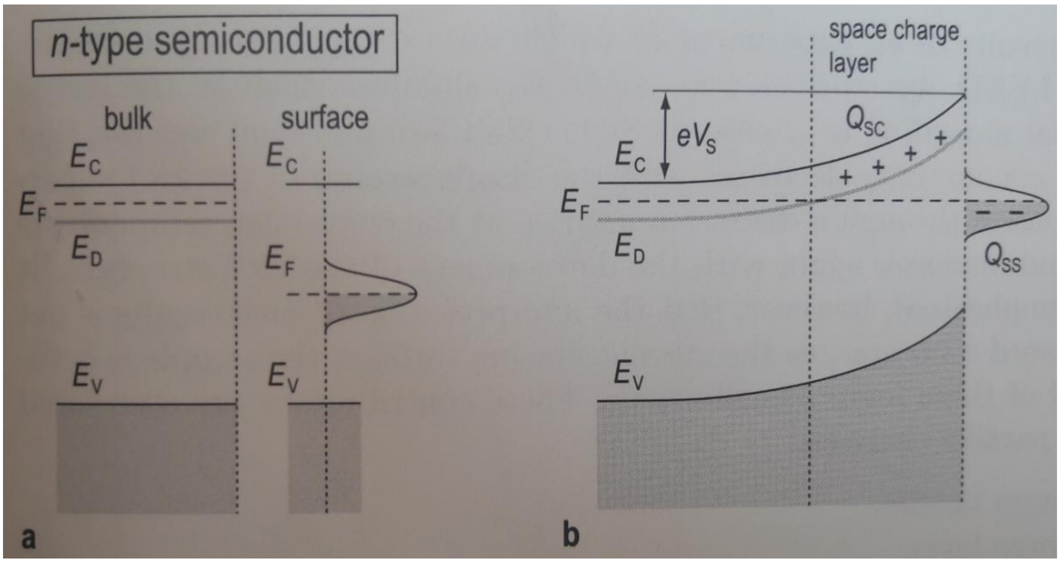

Figure 37: Schematic of Fermi energy pinning and band bending for an n-type semiconductor. a: Illustrates the metallic-like structure of Si(111)-7x7 from the half-filled surface state at the Fermi energy (E_F), and the Fermi energy mismatch between the bulk and the surface following the donor atoms at E_D. b: Illustrates the equalised Fermi energies via the transfer of charge from the bulk to the surface, with band bending occurring as a result. [57]

The presence of the tip can induce further band bending with the electric field perturbing the electronic structure of surfaces. However, at room temperature on the Si(111)-7x7 surface, the tip induced electric field is screened by states at the Fermi energy and no further tip-induced band bending occurs and so it is not discussed further in this thesis [59]. Further evidence for the absence of tip induced band bending is documented by Mysliveček *et al.*, where STS data of the Si(111)-7x7 surface taken at room temperature is independent of the start point current and voltage, and hence tip height above the surface [60]. Should tip induced band bending occur in this system, higher starting currents and therefore smaller tip-sample separation distances would result in this band bending effect. Different STS spectra would therefore be expected as the voltage is swept, as some of the voltage would be lost over the space charge layer.

The type of doping has also been investigated for its influence on the manipulation process, with the desorption yield of chlorobenzene on both p-type and n-type Si(111)-7x7 measured as a function of sample bias [61]. The yield for both samples reveals the same threshold voltages for both electron and hole injection and the yield follows the same trend. The manipulation process must therefore be independent of the doping type and dependant only on the surface states of the silicon. Therefore, doping is not further discussed in this thesis.

4.9 Molecular Bonding

The adsorbate chosen for manipulation is molecules of toluene, chosen because both this and other aromatic molecules such as chlorobenzene and benzene have been widely studied by both the Atomic Manipulation group here at Bath and by others [6, 42-44, 61, 62, 65, 75, 85]. This molecule readily adsorbs to the Si(111)-7x7 surface and is stable at room temperature. Its sensitivity to the tunnel current indicates that it has a long excited-state lifetime, suitable for current induced manipulation experiments.

A toluene molecule has the chemical formula $C_6H_5CH_3$ and has the structure shown in Figure 38a), with a distance of 2.78 Å between opposite carbon atoms [54]. Work has been done to investigate the bonding configuration of chlorobenzene, a similar aromatic molecule, on the Si(111)-7x7 surface. Due to the similar structure of these molecules, it is assumed they bond in the same way. Cao *et al*. conclude that the molecule forms two di-σ bonds with the Si(111)-7x7 surface - one to an adatom, and one to an adjacent rest atom in the layer below, illustrated in Figure 38b) [54]. The distance between an adjacent adatom and rest-atom pair is ~4.5 Å, and a Si-C bond is typically ~2 Å and hence bonding can occur without causing significant stress across the bonding site [51, 54].

It is the saturation of these dangling bonds that result in the dark spots on the STM image, as above a molecule it is harder to maintain the required tunnelling current and hence the tip approaches closer to the surface. The formation of these chemical bonds with the surface, chemisorption, is one method by which the molecule can adsorb to the surface. A second method is physisorption, where the molecule is weakly attracted to the surface via van der Waals forces. At room temperature, the residence lifetime of aromatic molecules like benzene on Si(111)-7x7 is ~2000 s [63], and these molecules enter the physisorbed state before undergoing diffusion to a new atomic site or desorption and leaving the surface [75].

A potential energy schematic of bonding is shown in Figure 39, where the chemisorption energy barrier E_C shows the energy required for the molecule to desorb when chemically bonded to the surface. The physisorption energy barrier E_P, is the energy required to leave the surface once the molecule is in the physisorbed state. E_b shows the energy barrier for a physisorbed molecule to chemisorb back to the surface having diffused to a new site [64]. Molecules in the physisorbed state are free to move laterally across the surface and typical diffusion length scales of 23 ± 1 Å have been measured, just under half the length of the Si(111)-7x7 unit cell [63].

Experimentally measured energy barriers for E_C are typically ~1.4 - 1.6 eV for chlorobenzene [75, 65] and ~1 eV for benzene [63, 66, 64]. For E_p, typical energy barriers are ~0.6 eV for chlorobenzene [65] and ~0.4 eV for benzene [64].

Figure 40 schematically shows the energy levels of the Si(111)-7x7 surface states for FC sites and the HOMO (highest occupied molecular orbital) and LUMO (lowest unoccupied molecular orbital) levels of chemisorbed toluene on the silicon surface. The LUMO level is determined from STS spectra above chemisorbed toluene on the Si(111)-7x7 surface [85] and the HOMO level determined from STS spectra obtained above a chemisorbed chlorobenzene molecule [67]. Due to the similar nature of toluene and chlorobenzene molecules discussed above, the HOMO level is assumed to be similar for both molecules.

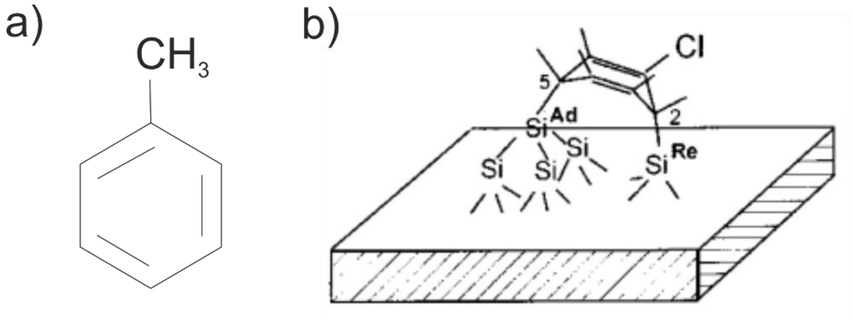

Figure 38: a) Structure of a toluene molecule, b) Schematic of the bonding configuration of chlorobenzene on Si(111)-7x7, which due to their similar nature is assumed as the bonding configuration for toluene [54].

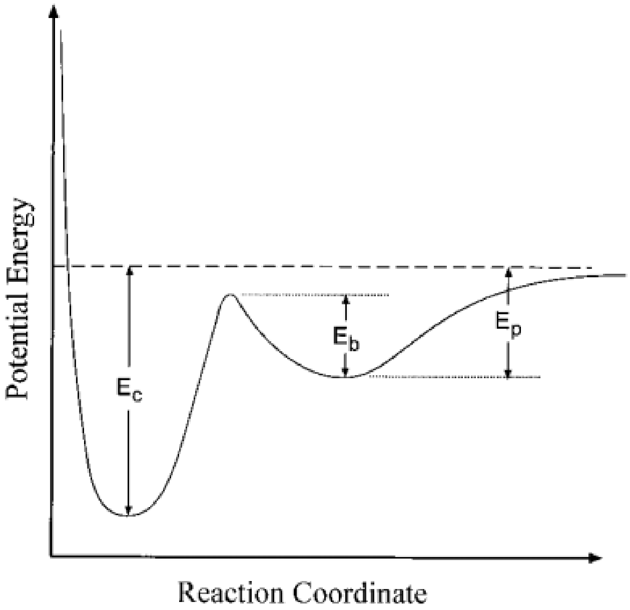

Figure 39: Potential energy curve showing the energy barrier for a chemisorbed molecule to desorb E_C*, for a physisorbed molecule to desorb* E_P*, and the energy barrier for a physisorbed molecule to re-chemisorb onto the surface* E_b*. [64]*

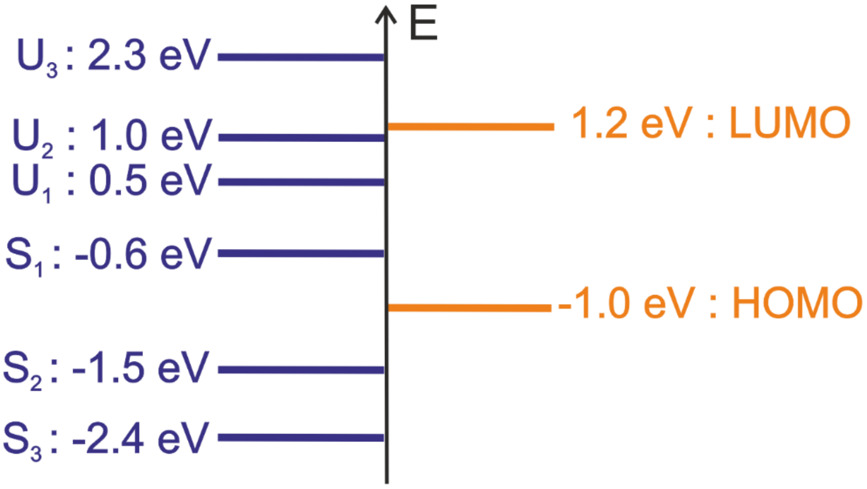

Figure 40: Schematic showing the energy levels of Si(111)-7x7 surface states in blue, and the HOMO and LUMO level of chemisorbed toluene on the Si(111)-7x7 surface in orange.

Chapter 5

Automation Techniques

To obtain statistically significant results from the single molecule manipulation injections, hundreds of manipulation events are measured for each data point at a specific current and voltage. Collecting such a large quantity of data is very time consuming. Consequently, to speed up the acquisition process, many experiments are automated via MATLAB and LabVIEW scripts. This section aims to explain the steps involved in the automation of manipulation injections.

5.1 Background

Nickel *et al.* used 4-acetylbihenyl molecules on Si(100)-2x1 at low temperature, which changes bonding configuration with voltage pulses of -2.7 to -4 V and 50 pA, with a threshold for switching at -2.7 V [68]. Long pulses resulted in multiple switching events of this reversible process. The switching time τ, and hence *R*, the switching rate (τ^{-1}), were extracted from fitting an exponential to the number of switching events as a function of time, plotted in Figure 41.

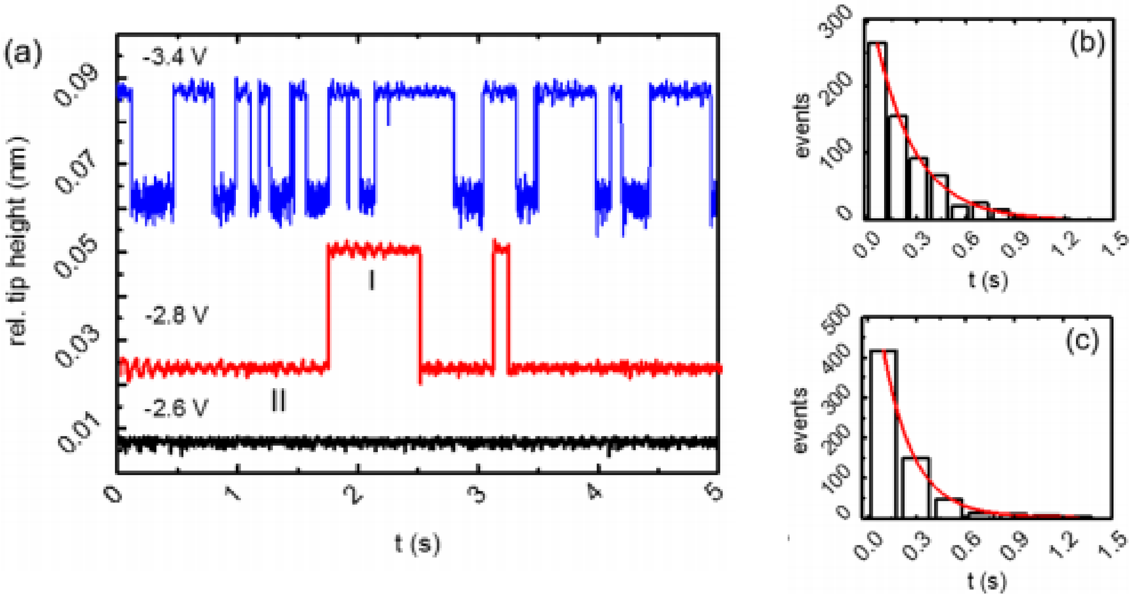

Figure 41: (a) Tip height as a function of time showing switching between bonding configurations of 4-acetylbihenyl molecules on Si(100) at three different voltages. The absence of switching below -2.7 V indicates a voltage threshold. (b) and (c): Binned data showing the exponential trend of the number of switching events as a function of time (state I to II and II to I respectively), allowing τ and R to be extracted from fits. [68]

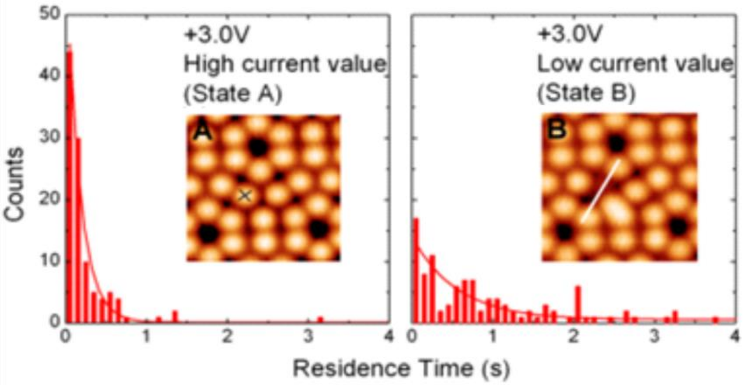

Figure 42: Exponential fitting to counts as a function of time gives the life time of each of these states. [37]

As discussed in section 3.3.1 Sagisaka *et al*. reported another reversible reaction producing multiple data points for each hopping motion of a Si(111)-7x7 adatom. Hence, large volumes of data were collected rapidly to obtain rates, seen in Figure 42 with state A the adatom in its usual Si(111)-7x7 position and state B the adatom hopped to an adjacent site [37].

In contrast, work by Soukiassian *et al.* has investigated the local manipulation of hydrogen on the Si(100)-2x1:H surface, where the tip was located above a hydrogen atom and injected a pulse of 2.5 V and 5 nA [69]. This resulted in an irreversible process where each manipulation event could only occur once. Desorption was identified by a spike in the tunnelling current trace and by a bright silicon atom being revealed, indicating that the removal of a hydrogen atom had occurred. Times-to-manipulation were extracted and binned allowing an exponential fit to obtain τ, and hence the rate of the desorption. This is illustrated in Figure 43 [69].

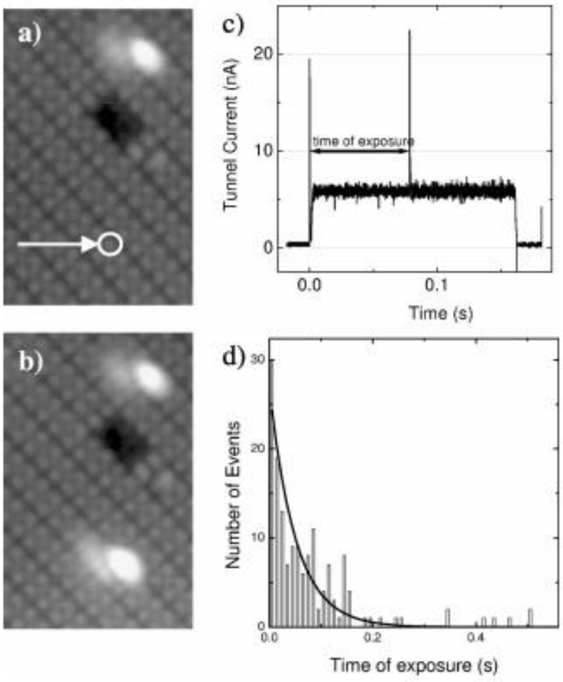

Figure 43: An irreversible process manipulating hydrogen on Si(100)-2x1:H. a) shows a before image with the arrow indicating the hydrogen above which an injection pulse of 2.5 V and 5 nA occurs. b) shows the after image where the hydrogen has desorbed and revealed a bright silicon dangling bond. The tunnel current trace in c) indicates a spike at the point of manipulation and the time-to-manipulation can be extracted and plotted in d). [69]

Similarly, manipulation of toluene on Si(111)-7x7 is an irreversible process with each reaction only providing one value in the data set for any given voltage and current parameters. Without the rapid repeatability of a reversible process, large data sets of hundreds of manipulations need to be carried out to gather enough statistically significant data. Typically, local manipulations such as these inject above a molecule to initiate a reaction and extract the time-to-manipulation. This is then binned and plotted to fit an exponential and a rate of manipulation is extracted, as in the examples above.

The automation techniques employed by our research group allow us to obtain large volumes of data and rates can be fitted directly from exponential plots of each individual time-to-manipulation for every molecule. Work done by Soukiassian *et al.* in Figure 43, highlights the importance of using large data sets to extract valid conclusions [69]. The group measured a reduction in the number of injected electrons required to cause hydrogen desorption from the Si(100)-2x1:H surface. This was previously reported as being 10 – 15 [70, 71] and concluded as 1 in their experiments [69]. Figure 44 shows the data obtained from both this group (black line) and that of the two previous groups (red and green lines). This shows the importance of obtaining data trends over a large parameter space (and including more than two data points), and for each data point in this parameter space to be robust and averaged from large numbers of experimental measurements when there are large error bars. The data points plotted in the black curve consisted of ~1000 measured desorption events [69]. This has allowed the group to conclude a single electron process for desorption in contrast to the multi-electron process required for manipulation concluded by the previous groups, despite the previous groups' data lying within the error bars of Soukiassian *et al.*.

The following section documents the automation process used in this thesis to help obtain large data sets in a shorter amount of time, compared to carrying out injection experiments manually.

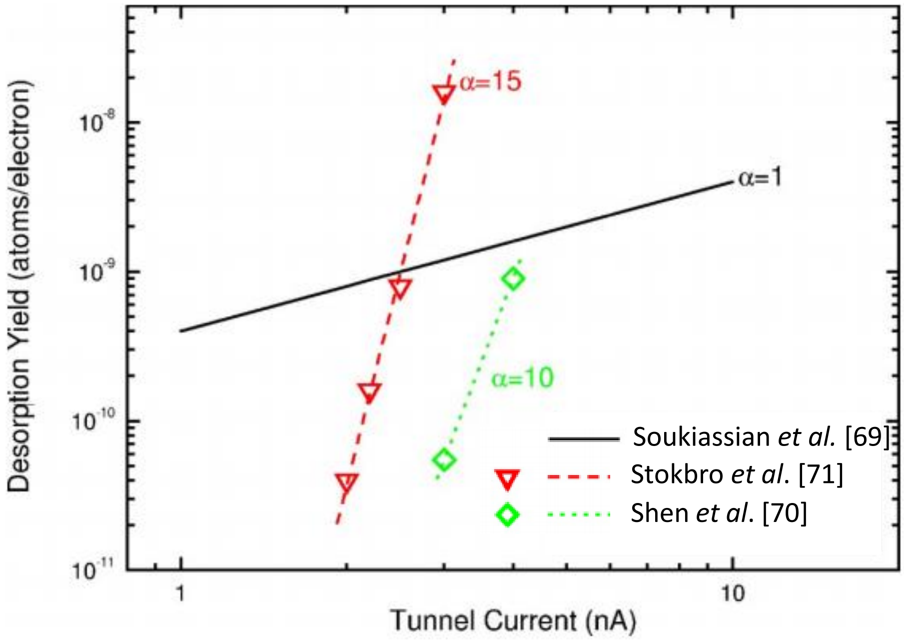

Figure 44: Hydrogen desorption yield on Si(100)-2x1:H as a function of tunnelling current carried out by three different research groups. The number of electrons required for a desorption is indicated by α and emphasises the importance of large data sets spanning a wide parameter space in order to draw accurate conclusions about the system investigated. [69]

5.2 Drift Tracking

As we are concerned with the manipulation of molecules directly below the tip, it is crucial to be sure that the region being scanned is constant. This allows comparison of the 'before' and 'after' image of the same scanned area and therefore the correct identification of the manipulation outcome. Working at room temperature means temperature fluctuations result in expansion and contraction of various STM components and over time the region being scanned can drift, as illustrated in Figure 45. During my MPhys project with Sarah Thomas, and then PhD student Duncan Lock, we wrote a LabVIEW script that deciphers the *x* and *y* shift in two consecutive STM images via a cross-correlation technique.

An initial reference image is taken, then a second consecutive image is chopped into a 3x3 grid. The central third is stepped across the reference image and cross-correlation indicates the location at which these two images best match, illustrated in Figure 46. The *x* and *y* shift from the initial central position to the new best matching location can then be subtracted from subsequent images. This ensures that the tip continues to scan the same region and compensates for the background movement of the surface. Before any experiments begin, this drift tracking software is run until the *x* and *y* shift decreases to less than 1 pixel, corresponding to a distance of 30 to 60 pm. Additional *z* drift compensation was added and an injection could commence once this had decreased to a shift less than 1-2 pm. This process is illustrated in Figure 46, where the drift tracking has been run until the cross-correlation determines an *x*, *y* and *z* shift of 52 pm, 26 pm and 242 fm respectively (an order of magnitude smaller than the size of the molecule).

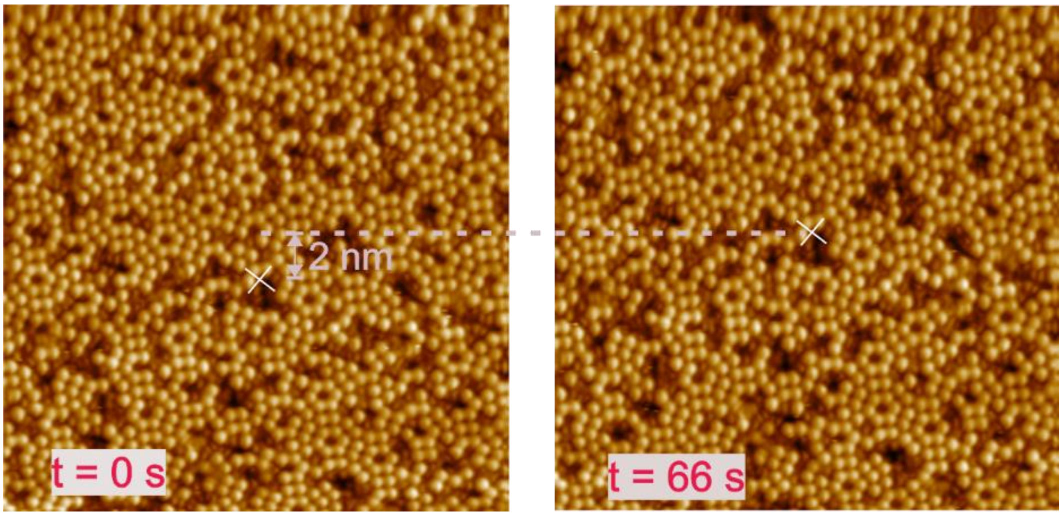

Figure 45: 25 nm STM images of a toluene dosed Si(111)-7x7 surface taken consecutively. Position 'x' drifts by 2 nm in 66 seconds. Image parameters: 1 V and 100 pA.

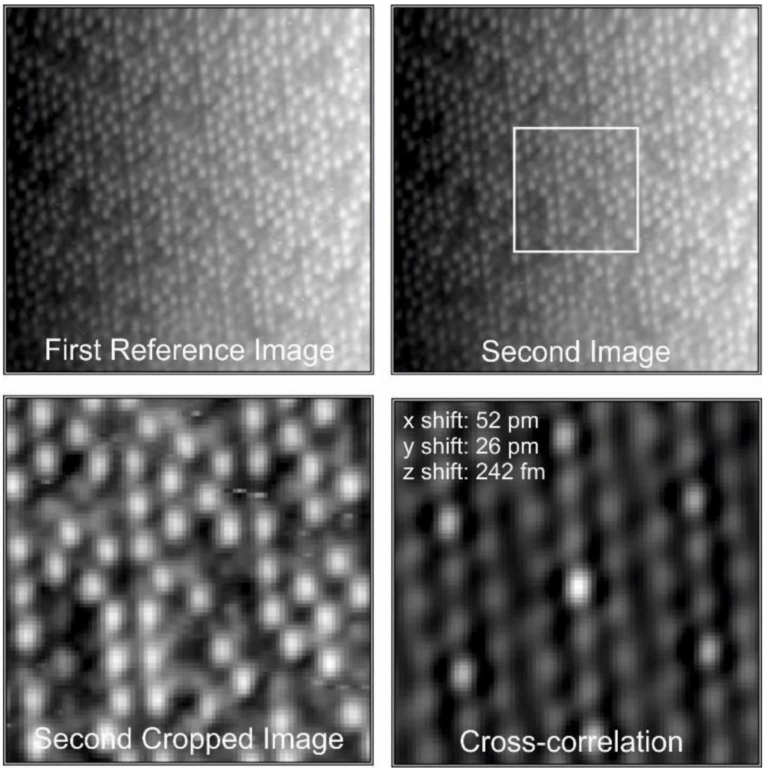

Figure 46: Stages of drift tracking - an initial image is taken, the second consecutive image is cropped and the central third is taken and cross-correlated with the initial image. The cross correlation finds the position of the 'best match' and hence the x, y and z shift can be compensated for.

5.3 Injection

A LabVIEW vi controls all the methods of injection, the stages of which are illustrated in Figure 47 a) – h). The script allows a specific site to be chosen and the injection voltage, current and time to be set. An initial 'before' image (typically 25 nm) is taken at passive parameters of 1 V and 100 pA, in Figure 47a). MATLAB then identifies a corner hole location on this image and knowing the unit cell co-ordinates for each adatom, identifies every adatom (yellow) and molecule (red) within the image, in Figure 47b). From this, a user specified number of molecules (here 5) are selected (blue) as injection sites.

The tip then moves to a molecule site, where further auto-correlation commences on a 3 nm image (Figure 47c) and d)), until a shift of less than 0.7 pixels is detected. This ensures that the correct region of the sample is still being scanned. A 3 nm 'before' image is taken in a downward scan direction, in Figure 47e). The tip then scans upwards, halting mid-scan at the centre of the image directly above the specific molecule where the injection parameters are then activated, in Figure 47f). Once finished, the tip continues its upward scan where a manipulated molecule can be identified by the half-moon shape of a newly revealed silicon adatom in the top half of the image. An 'after' image in Figure 47g) follows, again in the downward motion. It is these 3 nm 'before' and 'after' images that are compared to determine the manipulation outcome of the molecule. A final large 'after' image in Figure 47h) concludes the injection experiment.

The tip height and the tunnel current are recorded for the duration of the injection. When injecting directly above a molecule, the tip retracts upon manipulation as the silicon adatom beneath is easier to tunnel to with a higher LDOS. The retraction step in the recorded tip height trace enables the time-to-manipulation to be identified. Further details on the tips movement and height trace are explained in section 6.2.

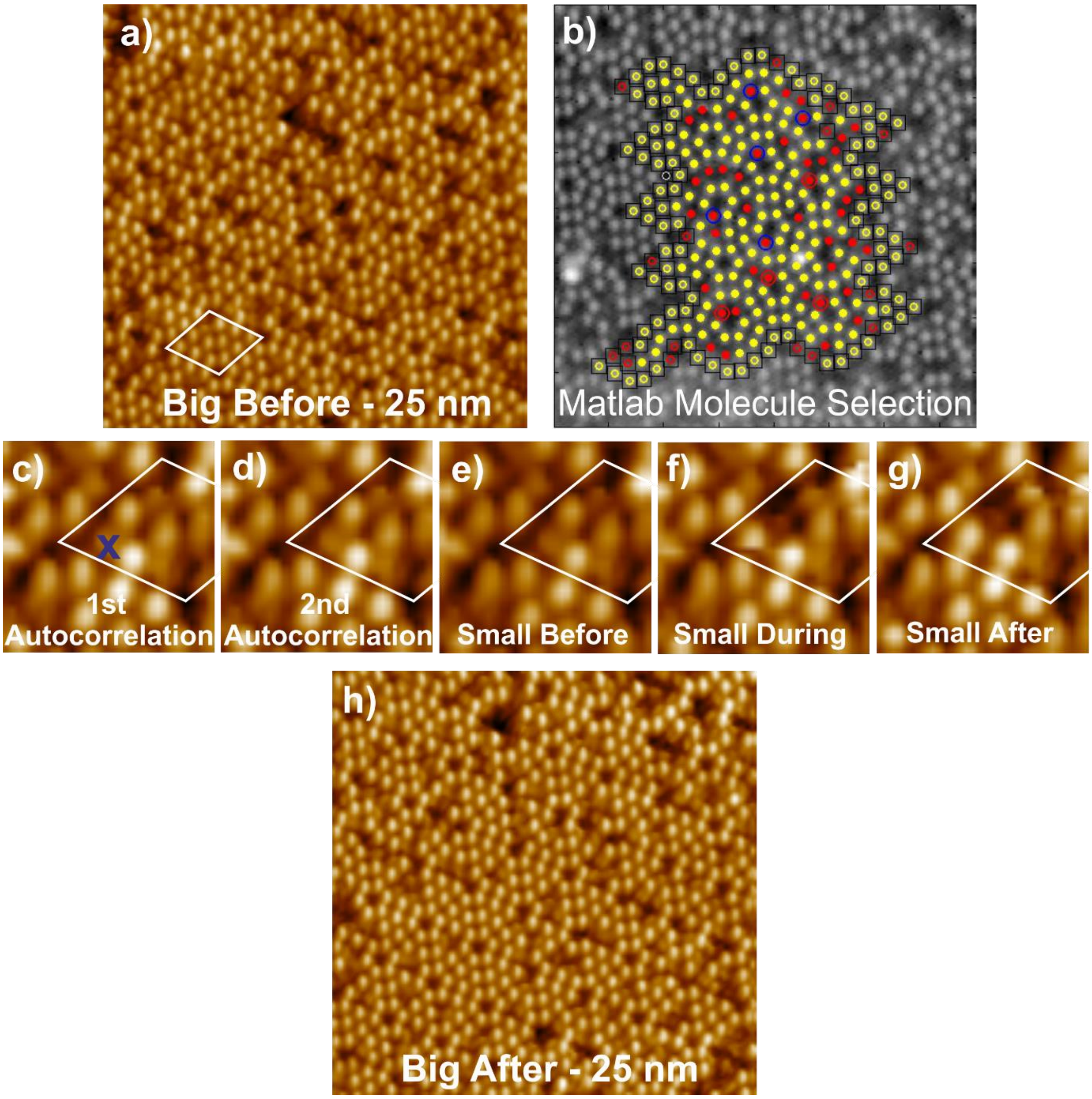

Figure 47: Stages of the injection process. a) A 25 nm big 'before' image is taken, MATLAB identifies a corner hole from this image and uses the unit cell coordinates to highlight every adatom (yellow) and molecule (red) in b). Molecules circled blue have been selected for injection. The tip moves to a selected molecule site and carries out further drift tracking in c) and d) with 3nm images. A small 'before' image follows e), the 'during' image in f) is obtained in the opposite scan direction, bottom to top, and the tip halts above the molecule to carry out the injection at elevated injection voltage and current for the specified injection time. Finally, a small 'after' image is taken in g) and once all molecules selected have been injected, a big 'after' image is taken in h). All images are obtained at passive imaging parameters: 1 V and 100 pA

Chapter 6

Local Manipulation

Tunnel current induced manipulation is a widely investigated method of atomic manipulation. Following on from the work of Stipe *et al*., groups have investigated a variety of molecules on a range of surfaces. A brief overview and examples of local manipulation will be given below, introducing key concepts within this category. This tunnel current induced local manipulation is achievable on a toluene dosed Si(111)-7x7 surface. Work documented in this chapter aims to understand this local process in more detail with the view to investigating the excited-state lifetime of the toluene molecule.

The local manipulation process of a single molecule can be influenced by the energy and position of the injected charge from an STM tip. The desorption process can evolve following the excitation of the molecule by the injected charge and result in manipulation. This chapter aims to address what happens to the excited state itself and how this can be influenced. We find that the close proximity of the tip to the molecule results in a reduced probability of manipulation, occurring from a quenching of the molecules excited-state lifetime by over two orders of magnitude. We propose that this happens due to the creation of a new tip dependant decay channel for the excited state to decay to, prior to its naturally elapsed lifetime. This work has been accepted for publication in *Science* [72].

6.1 Literature Review

Local tunnel current induced manipulation involves manipulating the molecule directly below the tip, causing a manipulation event restricted to within the tunnel junction region, like that seen in the bond dissociation of Stipe *et al*. [5]. The mechanisms behind this method of manipulation are DIET (desorption induced by electronic transitions), or DIMET, with ‘multiple’ electronic excitations. There are two common models used to describe these processes, the Menzel-Gomer-Redhead (MGR) model and the Antoniewicz model. Both models describe an adsorbate-substrate system by two molecular electronic states: an excited and a ground state. These are plotted as a function of the distance between the adsorbate and the substrate (often called the reaction co-ordinate), seen in Figure 48a-c [73]. With the MGR model, the excited state potential is repulsive and results in an increased adsorbate-substrate distance before the adsorbate relaxes back to the ground state. The Antoniewicz model results in a reduced adsorbate-substrate distance when the adsorbate is excited, as the equilibrium bond length is shorter for the excited state compared to the ground state. This Antoniewicz model best describes metal systems, which are stabilised by image charges of the charged adsorbate resonance in the substrate, whereas the MGR model best describes adsorbates on the silicon surface [73].

Incident electrons (or holes) from the STM tip can excite a molecule from the ground state to the excited state. Depending on the lifetime of this excited state, the molecule may be able to overcome the energy barrier to desorption and leave the surface. A short lifetime in the excited state may result in the molecule failing to desorb. The molecule returns back down to the ground state and is said to be vibrationally excited. These are Franck-Condon transitions which occur due to the over-lap of the excited and ground state wavefunctions [73].

The DIET or DIMET processes occur depending on the rates of excitation and relaxation of the molecule, see Figure 48d-e. DIET occurs when a single incident electron (or hole) excites the molecule to the excited state, but the relaxation rate is faster than the excitation rate. Therefore, if the molecule is yet to overcome the barrier to desorption, it returns to the ground state before a second electron arrives. Each incident electron therefore interacts with a molecule in its neutral ground state.

DIMET occurs when the relaxation rate is slower than the excitation rate. It may be that an incident electron excites the molecule to its excited state, however the short lifetime of this results in the relaxation down to a vibrationally excited state when a second incident electron arrives. This excites the molecule back to the excited state again and the cycle is repeated until the molecule is able to overcome the energy barrier to desorption. Each of these processes are illustrated in Figure 48d-e. Typically, for a current of 100 pA the time between tunnelling electrons is ~1 ns compared to a typical excited state lifetime of the order of femtoseconds.

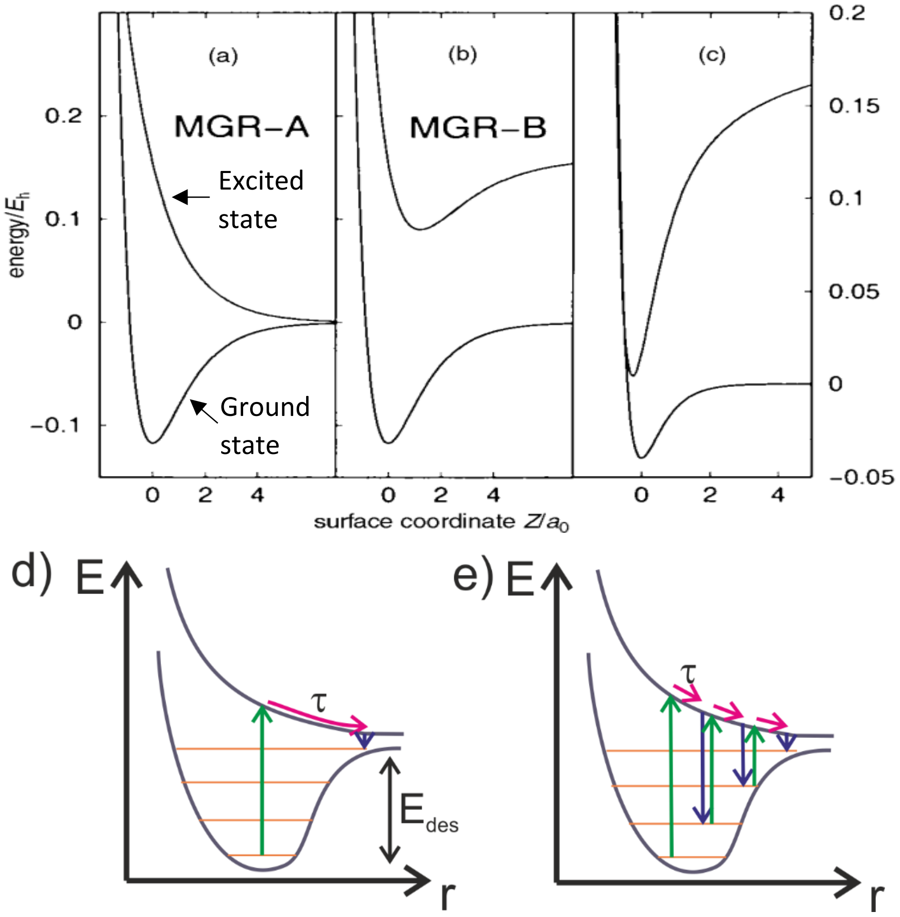

Figure 48: Schematics of the excitation process of a molecule. a) and b) show two excited state types of the MGR model, c) shows an Antoniewicz model. a)-c) from [73]. d) DIET process where an incident electron excites the molecule from the ground state to its excited state (green arrow) in an MGR model. The lifetime of the excited state τ is sufficiently long enough that the molecule can overcome the energy barrier to desorption E_{des}. e) DIMET process, where the lifetime of the excited state is shorter and hence the molecule relaxes back to a vibrationally excited state (blue arrow) when a second electron excites the molecule again. Multiple electron excitations result in the molecule being able to overcome the energy barrier to desorption. Each plotted with energy as a function of the adsorbate-substrate distance.

It is possible to identify the number of electrons involved in the manipulation process by considering the excitation rate, R as

$$R=I/e. \tag{6.1}$$

The probability, P, of transitioning from one vibrational state to the next is therefore proportional to the current, $P(0\rightarrow 1) \propto I$. It follows that multiple excitations between vibrational states up to an *nth* vibrational state result in

$$P = P(0\rightarrow 1) \times P(1\rightarrow 2) \times \ldots \times P(n-1\rightarrow n) \tag{6.2}$$

$$\propto I \times I \times \ldots \times I \propto I^n \tag{6.3}$$

Hence, the probability P and rate R are $\propto I^n$, a power-law current dependence indicating the number of transitions or electrons required for the manipulation [5].

Expanding on the Stipe *et al.* oxygen dissociation example [5], the rate of dissociation was investigated for a range of currents at different voltages and is shown in Figure 49. Fitting to each curve revealed $I^{0.8\pm0.2}$, $I^{1.8\pm0.2}$, and $I^{2.9\pm0.3}$ showing a 1, 2 and 3 electron process for 0.4, 0.3 and 0.2 V respectively, illustrating the difference between a DIET process involving a single electron compared to a 'ladder climbing' effect of multiple electrons in the DIMET process.

Other outcomes of this local manipulation method directly below the tip include tautomerization, a process where typically a hydrogen is moved within a compound to create a new one. The injection of electrons into a porphycene molecule on the Cu(111) surface at 5 K induced this tautomerization process [7]. This molecule bonded to the surface initially in the *trans* tautomer configuration and appeared as a bright molecule with a dark centre when imaged with the STM, seen in Figure 50.

A voltage pulse of -280 mV for 100 ms was applied above the molecule and the 'after' image revealed a new configuration, the *cis* tautomer, with a dark region no longer in the centre of a bright molecule in the STM image. The injected charge had caused the hydrogen to switch bonding location, as indicated in the schematic in Figure 50. Reactions such as this, within a single molecule, present possibilities for creating atomic switches.

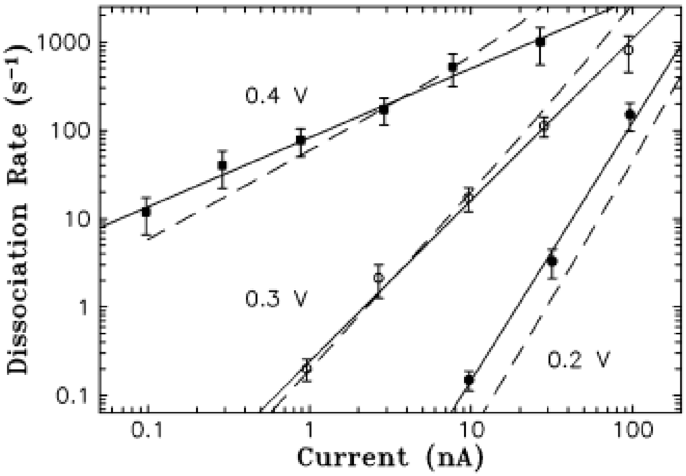

Figure 49: Dissociation rate as a function of current for oxygen atoms on Pt(111) for three different injection voltage pulses. The solid line shows the line of best fit to the experimental data and the dashed line shows the theoretical model. The gradients show a 1, 2 and 3 electron process for 0.4, 0.3 and 0.2 V respectively [5].

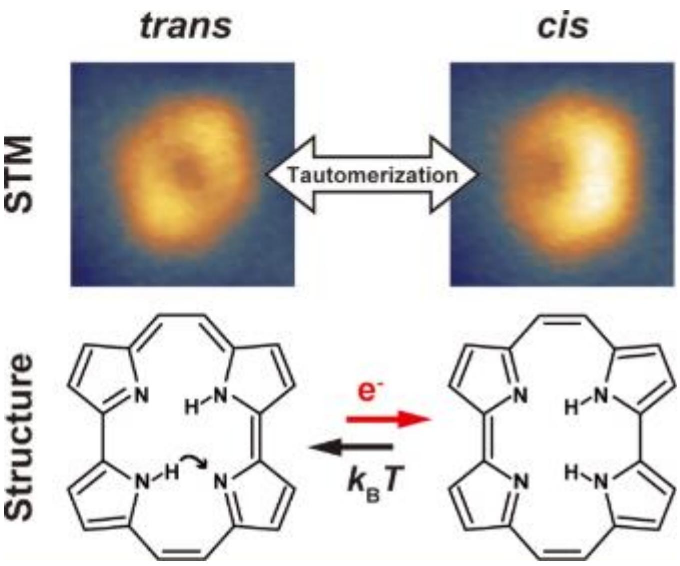

Figure 50: STM images illustrating the difference between an imaged porphycene molecule on Cu(111) in the trans and cis configurations following tautomerization and chemical schematics illustrating the hydrogen switching process. [7]

Molecular rotation shown by the Wilson Ho group is another form of local manipulation outcome. Here, molecular oxygen on the Pt(111) surface was initiated to rotate following a voltage pulse directly above the molecule. A drop in the recorded tunnel current identified the time of rotation [74]. Further imaging revealed that the molecule had rotated its bonding orientation, in Figure 51. A voltage threshold present in the system meant rotation was only observed above 0.1 V, and transitioned from a multiple electron process (DIMET) below 0.15 V injections, to a one electron process (DIET) above 0.15 V.

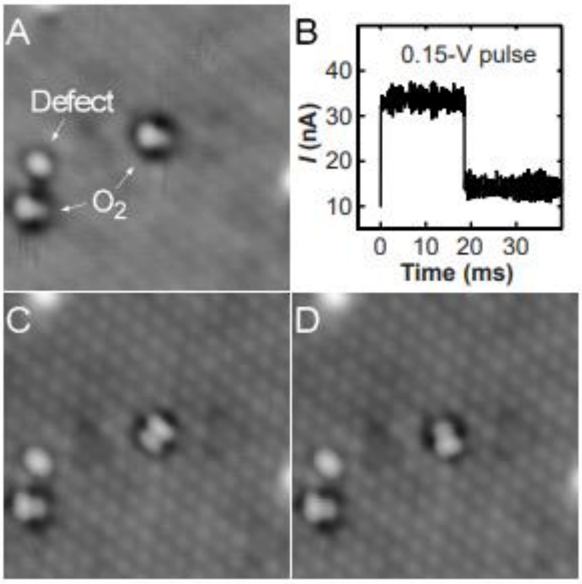

Figure 51: Molecular rotation of an oxygen molecule on Pt(111). A: An STM image of an oxygen molecule, B: a 0.15 V injection pulse above the molecule results in a drop in tunnelling current at the point of rotation. C: Following a voltage pulse the oxygen molecule has rotated, D: a second voltage pulse results in a third orientation. Scan parameters: A: 50 mV and 1 nA, C and D: 50 mV and 10 nA. [74]

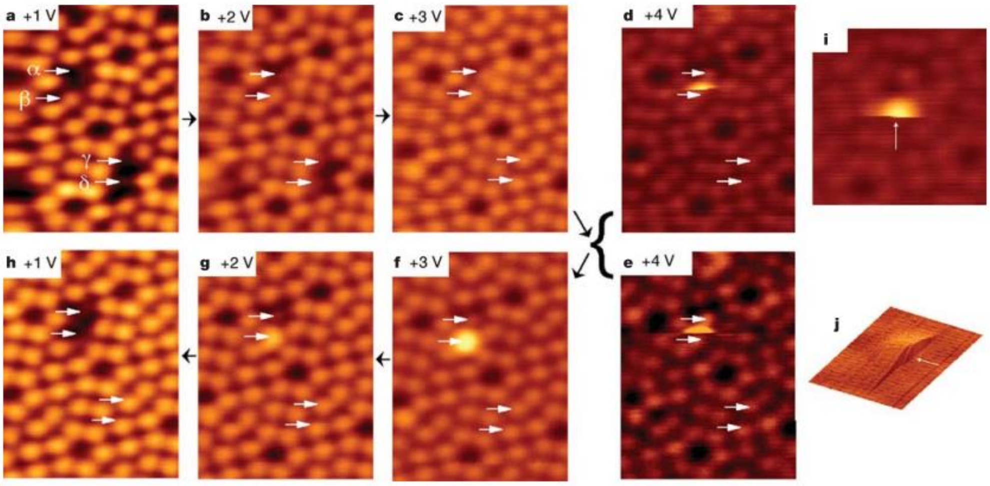

Figure 52: STM images of chlorobenzene dissociation and desorption on Si(111)-7x7 at increasing voltage a – d. a: Passive scan where three chlorobenzene molecules are indicated by α, γ and δ. c: Chlorobenzene molecules γ and δ have desorbed revealing a bright adatom beneath. In d, the presence of a bright half-moon indicates the point of dissociation of the chlorobenzene molecule. i and j showing the halfmoon signature of dissociation in 2D and 3D respectively. f: Shows the dissociation of the chlorobenzene α, where a chlorine atom is imaged at site β. [6]

Typically, these local manipulation events are dependent on the energy of the excitation, evident from the presence of a voltage threshold in these examples. Further energy dependence is seen by the tunnel current induced desorption and dissociation of a chlorobenzene dosed Si(111)-7x7 surface at room temperature, reported by Sloan and Palmer [6]. Here, scanning at voltages increasing from 1 V to 4 V instigated the desorption and dissociation processes, shown in Figure 52. The 1 V scan in Figure 52a allows the chlorobenzene molecules to be identified as dark spots and the underlying silicon adatoms as bright spots. The molecules labelled γ and δ can be seen to desorb and leave the surface once scanned at 3 V in Figure 52c, as a bright silicon adatom has been revealed beneath. Scanning at 4 V in Figure 52d, resulted in the dissociation of a chlorine atom from the molecule, identified by the bright feature in Figure 52f at location β. The exact moment of this dissociation was identified in Figure 52d from the arrival of the bright half-moon region whilst scanning.

The group measured the rate of both outcomes as a function of current, as plotted in Figure 53. For desorption, a linear dependence was seen with an exponent of 0.9 ± 0.1, showing a 1-electron process. In contrast, the dissociation rate had an exponent of 1.8 ± 0.3 at 3 V, indicating a 2-electron process, each showing a DIET and DIMET process respectively.

Two electrons were required for the dissociation as the first attached to the molecule and vibrationally excited it, (so much so that in some cases the molecule desorbed, as seen for γ and δ), a second incident electron caused further excitation whilst the molecule was still excited from the first, which was transferred to the C-Cl bond breaking it off. Therefore, two electrons were required for dissociation to occur.

Position dependence of the STM tip also plays a role in the local manipulation process. Another system of biphenyl molecules adsorbed on Si(100) at low temperatures were induced to switch location when the tip was placed above a molecule and charge injected at -2 V and 0.2 nA [8]. A drop in tunnelling current indicated a switching of the molecules position to a new bonding configuration, shown in Figure 54. The times to manipulation were extracted and the yields (the probability of switching per injected electron) for this switching process were found. This was repeated for three different injection

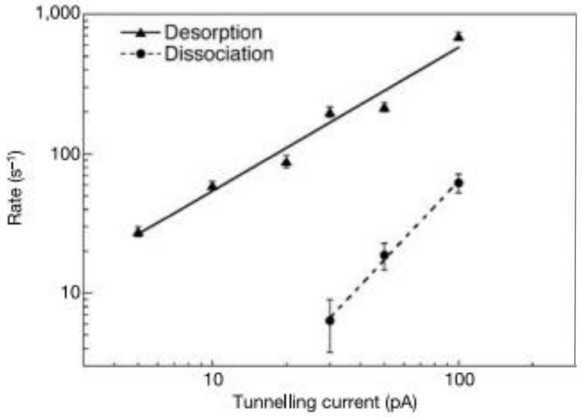

Figure 53: Rate of desorption and dissociation as a function of tunnelling current, gradients show this is a 1-electron process for desorption and a 2-electron process for dissociation. [6]

locations shown in Figure 54E, giving the switching yield for site: $P_1 = 2.7 \times 10^{-12}$, $P_2 = 2.5 \times 10^{-13}$ and $P_3 = 5 \times 10^{-11}$. This revealed a position dependence of the yield between these two bonding configurations greater than two orders of magnitude between sites P_2 and P_3, corresponding to a tip movement of 4 Å towards the molecule [8].

The local manipulation process of single molecules can therefore be influenced by the energy and the position of this injected charge, allowing a DIET or DIMET process to continue following the tunnel current induced excitation of the molecule to be manipulated. What has not been shown is the ability to influence the excited state of the molecule and control the excited state itself. This is the motivation behind the first section of this thesis, opening up the possibility to control reactions at a molecular level, specifically for toluene molecules on the Si(111)-7x7 surface.

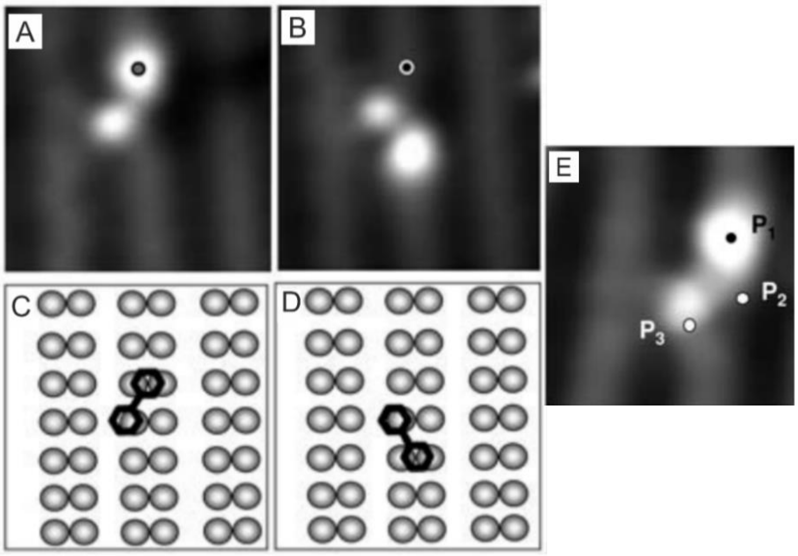

Figure 54: Position dependence of local manipulation. A: STM image of a biphenyl molecule on Si(100) with the injection location marked by a circle. B: Switched bonding configuration following a negative bias injection. C and D schematically show the bonding configurations. E: Injection at three different positions above the molecule P_1, P_2 and P_3 each result in a different switching probability indicating a position dependence for this switching process. Scan parameters: A and B: -2 V and 0.2 nA, 21 Å x 21 Å. E: -2 V and 0.56 nA. [8]

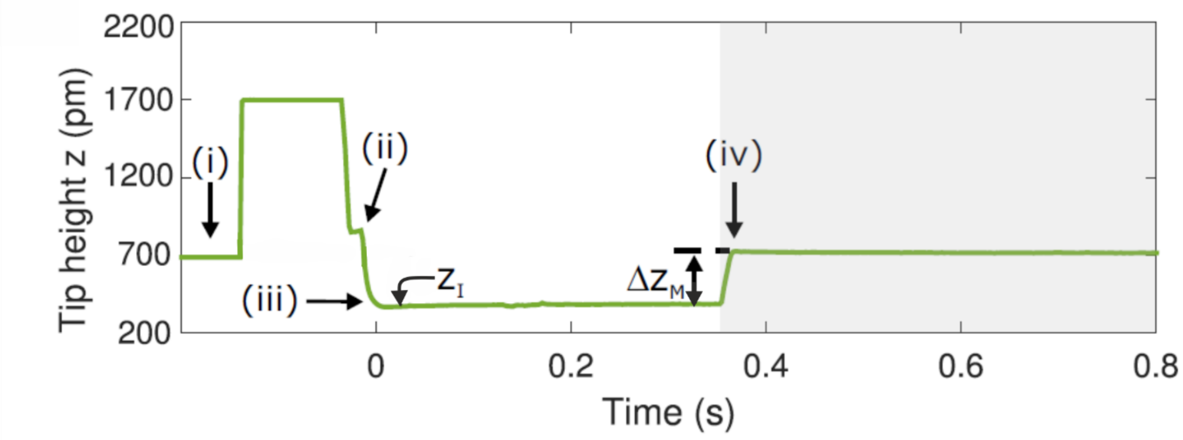

Figure 55: Tip height trace during an injection. (i) The tip height during passive imaging parameters of 1 V and 100 pA. (ii) Tip approaches to achieve 20 pA, and (iii) the feedback loop achieves the elevated injection parameters, at tip height z_I*. (iv) A manipulation event results in a tip retraction to maintain the constant tunnelling current, this* Δz_M *step indicates the time-to-manipulation. The white region shows the time the tip is over a molecule and the grey region highlights when the tip is over the adatom.*

6.2 Detecting manipulation

The injection process is detailed in section 5.3 and during the injection pulse the tip *z* height trace is recorded, shown in Figure 55.

i) At passive imaging parameters of 1 V and 100 pA, the tip is then withdrawn by 1 nm from the surface. The feedback loop is switched off and the voltage and current increased to the injection parameters away from the surface.
ii) The tip approaches to achieve 20 pA, to avoid excess over shoot.
iii) With the feedback loop on, the tip achieves the set manipulation parameters and the injection commences.
iv) The tip detects higher tunnelling current and retracts from the surface to return to the set-value. A manipulation event has occurred. As a guide, the white region indicates the tip sitting above a molecule and the shaded area indicates when the tip is positioned above an adatom, following manipulation.

At the end of the 8 s injection window (not shown on Figure 55), the feedback loop is disabled, the tip is retracted again to return to passive parameters before the feedback loop is enabled and the tip returns to the surface. This is the end of the injection step and an ‘after’ image would follow.

The retraction in step iv) allows us to identify the exact time-to-manipulation, which is extracted from a MATLAB script GUI. This allows the user to identify the start of the injection (iii) and the manipulation event (iv) from each trace and assign the type of manipulation outcome.

6.3 Results

For a given injection current and voltage, hundreds of times-to-manipulation values are extracted following the MATLAB trace analysis explained in section 6.2. For each injection current, we plot the fraction of manipulated molecules N/N_0 as a function of time, for ~120 times-to-manipulation (with *N* being the number of molecules manipulated and N_0 the total number of original molecules), plotted in Figure 56a.

Given a first order rate equation for the time dependant probability that a molecule will remain in its original position,

$$\frac{dP_r(t)}{dt} = -\frac{P_e I}{e} P_r(t) \tag{6.4}$$

where P_e is the probability per electron of manipulation and $P_r(t)$ is the probability of the molecule remaining.

Given the boundary condition that $P_r(0) = 1$ we can write that the probability of a molecule remaining on the surface is

$$P_r(t) = exp\left(-\frac{P_e I}{e} t\right) \tag{6.5}$$

Hence it follows that the time dependant probability of a molecule being manipulated can be written as

$$P(t) = 1 - exp(-kt) \tag{6.6}$$

where $k = \frac{P_e I}{e}$, the rate of manipulation, measured in our experiments. This probability is equivalent to experimentally measuring the fraction of molecules manipulated N/N_0, so the rate of manipulation can be extracted directly from exponentially fitting to the distribution of our measured times-to-manipulation, plotted in Figure 56a.

Figure 56b and c show how the rate of manipulation varies as a function of current for electrons and holes respectively. The rate dependence for electrons in Figure 56b shows a linear dependence, where the rate increases for larger values of tunnelling current. Considering the DIET and DIMET rate derivation from section 6.1, where is $k \propto I^n$, reveals that this is a one electron process for the manipulation of toluene with electrons. Electron data was not taken for any lower currents as very few manipulation events occurred and therefore statistically reliable rates could not be extracted from these.

This trend is mimicked in the hole injection data in the low current regime of 2 to 10 pA (grey region in Figure 56c), again indicating a one-hole excitation process for manipulation. However, the rate plateaus for higher current injections above 10 pA. Following $k \propto I^n$, this appears to indicate a near zero-electron process. Bizarrely, it seems the manipulation process is *independent* of the injected charge for these current injections.

If manipulation within this current regime were to be current independent, then possible causes of the manipulation events could be: thermally induced diffusion and desorption, mechanical interaction with the tip or electric field effects.

6.3.1 Thermal Effects

Work by Lock *et al*. has documented the thermal desorption and diffusion events of benzene, toluene and chlorobenzene on the Si(111)-7x7 surface, by time-lapsed STM imaging [75]. Images were taken 12 minutes apart to minimise the surface's exposure to the tip. Molecules desorbing from the surface were tracked and the rates of manipulation were determined. These rates were 10^{-4} times smaller than

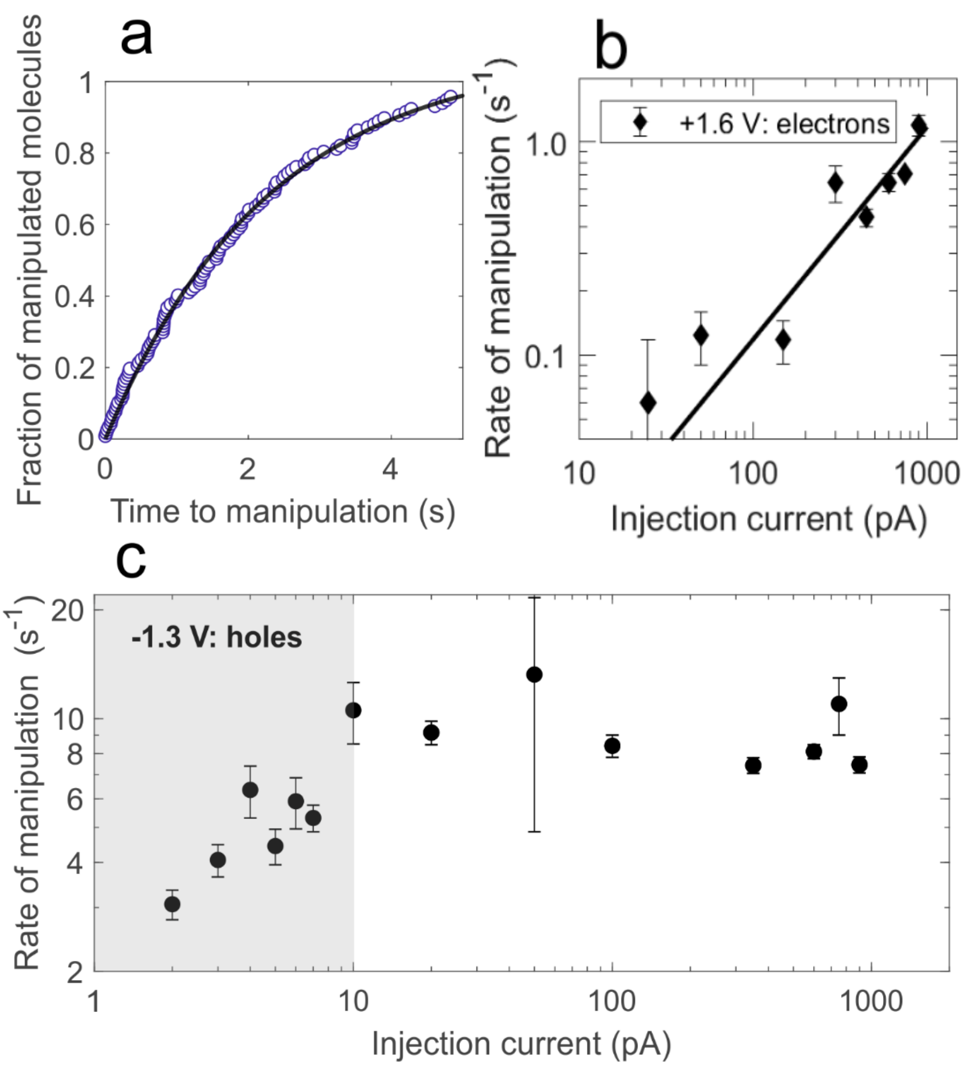

Figure 56: a: Fraction of manipulated molecules as a function of the time taken to be manipulated, fitted with a first order reaction probability P(t) = 1 - e^{-kt} *to extract the rate k. (Data from 1.6 V, 400 pA injections into 117 molecules.) Rate of manipulation k, as a function of current is shown for electrons in b, with a linear relationship indicating a 1-electron process. The rate of manipulation for holes is shown in c, with a linear relationship in the low current regime in the grey region. This rate plateaus with injection currents above 10 pA.*

the rates determined in Figure 56 and hence the tip is required for these manipulation events to arise. If it is a true, zero-electron process and the tip is not the source of the current, what is the role of the tip in this invariant rate of manipulation region?

6.3.2 Mechanical Tip Interaction

To determine whether the tip is interacting with the system to cause manipulation, injections were carried out with 0 V and 0 pA to ensure no tunnel current was present. Injections were achieved in the same way as described in section 5.3 with a recorded tip height trace similar to that in section 6.2. This injection process was modified at stage (iii) where the tip was instead moved to a user specified distance before the 0 V, 0 pA injection commenced.

All injections begin with passive imaging parameters in (i) and hence the tip always begins at the same height. The retraction height (Δz_M in Figure 55) is also extracted from the post injection MATLAB analysis. The tip height used and referred to herein is the initial tip height z_I, when the tip has achieved the injection parameters above a molecule. This is measured with respect to the centre of the bonding silicon adatom.

Injections for a 200 to 900 pm height range were carried out above toluene molecules. Completing the analysis described above, the rates of manipulation were used to find the corresponding probability of mechanical manipulation, seen in Figure 57b. An increase in the manipulation probability occurs when the tip approaches to within 600 pm of the sample. The tip height was deduced from force spectroscopy with a qPlus STM by Majzik *et al.,* where an increase in repulsive force from the Pauli Exclusion Principle occurred when the qPlus STM tip was approached within a 600 pm distance of benzene on the Si(111)-7x7 surface [76]. Due to the similar nature of these aromatic molecules, this 600 pm height was correlated to the increase in probability in this mechanical manipulation experiment. However, the distance corresponds to the centre of the tip apex atom to the centre of the bonding silicon adatom and hence, the true gap distance between the tip and the molecule will be smaller.

This 600 pm threshold indicates that at distances this close to the molecule, the STM tip can influence the system being probed. The potential energy landscape of the surface is modified and hence lowers the energy barriers to both desorption and diffusion, reportedly reduced by ~100 meV, making it easier for molecules to be thermally excited and leave the surface [77].

Plotting our data with the tip height as a function of tunnel current in Figure 57a, shows that as expected, the tip height decreases as the tunnel current increases because the tip approaches closer to the sample to achieve the set tunnelling current. The dashed lines mark the 600 pm separation and Figure 57a indicates that for all the manipulation injections undertaken, the tip is at distances greater than this from the sample. Therefore, mechanical manipulation can be ruled out as a source of the plateau seen in Figure 56c, also due to the linear relationship between the current and tip height in Figure 57a suggesting we are not yet in contact with the molecule [26].

6.3.3 Electric Field Effect

To assess whether the electric field is aiding the manipulation process, an experiment where only the electric fields presence is experienced by the molecule on the surface was carried out [97]. The electric field was estimated for all the currents probed in our experiment using $E=V/d$, where d is the tip height above the surface. To verify this parallel-plate capacitor field assumption, the electric field has been modelled between two spheres separated by a distance of $2z_0$, where the sample surface lies halfway between, defined as $z=0$. The z dependence of this field has been mapped and assumed to change by less than 10% across the gap and solved for a gap distance of 700 pm. This suggested a tip radius of 4.6 nm, whereas a typical tip radius for our STM tips are tens of nanometres and hence larger than the radius required for a field change less than 10% [72]. Therefore, the parallel plate capacitor electric field $E=V/d$ assumption holds. Figure 57c shows that as expected, for increasing current the closer proximity of the tip to the sample results in larger electric fields within the tunnel junction.

In order to maintain an equivalent electric field at the adsorption site, the tip was retracted by a set distance and a voltage of -10 V used with 0 pA so no charge is injected, altering stage (ii) in Figure 55. Injections were then carried out and analysed in the same way with the results shown in Figure 57d for a range of electric fields. Following injection, most molecules remained at their adsorption site with

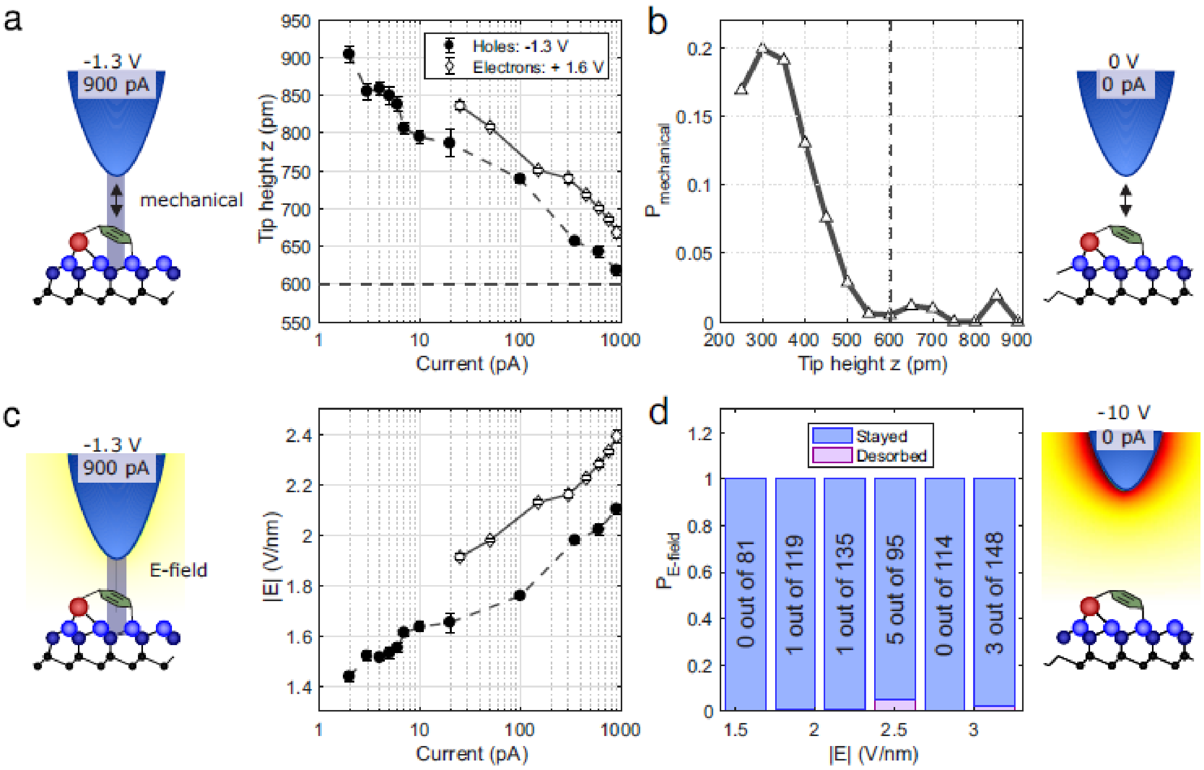

Figure 57: Mechanical a-b and electric field interactions c-d. a: Tip height as a function of injection current for both the hole (solid circles) and electron (blank diamonds) data taken in this experiment. b: Probability of mechanical manipulation as a function of tip height during 8 s injections of 0 V and 0 pA. c: Electric field within the tunnel junction as a function of tip height for both the hole (solid circles) and electron (blank diamonds) data taken in this experiment. d: Probability of desorbing or remaining on the surface as a function of the electric field during 8 s injections with a retracted tip at -10 V and 0 pA.

a negligible number of desorptions induced. Therefore, it is concluded that the electric field due to the presence of the tip cannot be a factor in this plateau region of the rate of manipulation.

6.4 Discussion

There is also no evidence of intra-molecular bond breaking [6] and initial investigations probing the branching ratio (the ratio of desorption to diffusion manipulation events) shows that for the range of currents probed, the ratio is roughly constant. (The following chapter discusses the branching ratio in more detail.) Therefore, it is assumed that the same manipulation mechanism must be occurring for both the low and the high current regimes. The rate dependence in Figure 56b and c can be recast in terms of P_e, the probability per injected charge of manipulation, plotted as a function of tip height in Figure 58a and b. For electrons in Figure 58a), the probability of a manipulation event is considered constant for the range of tip heights, as expected for a 1-electron process. However, for holes in Figure 58b), as the tip height reduces the probability of manipulation per hole decreases. To decipher the physics within this situation we must refer back to the DIET process of Figure 48a) and consider the lifetime of the excited state.

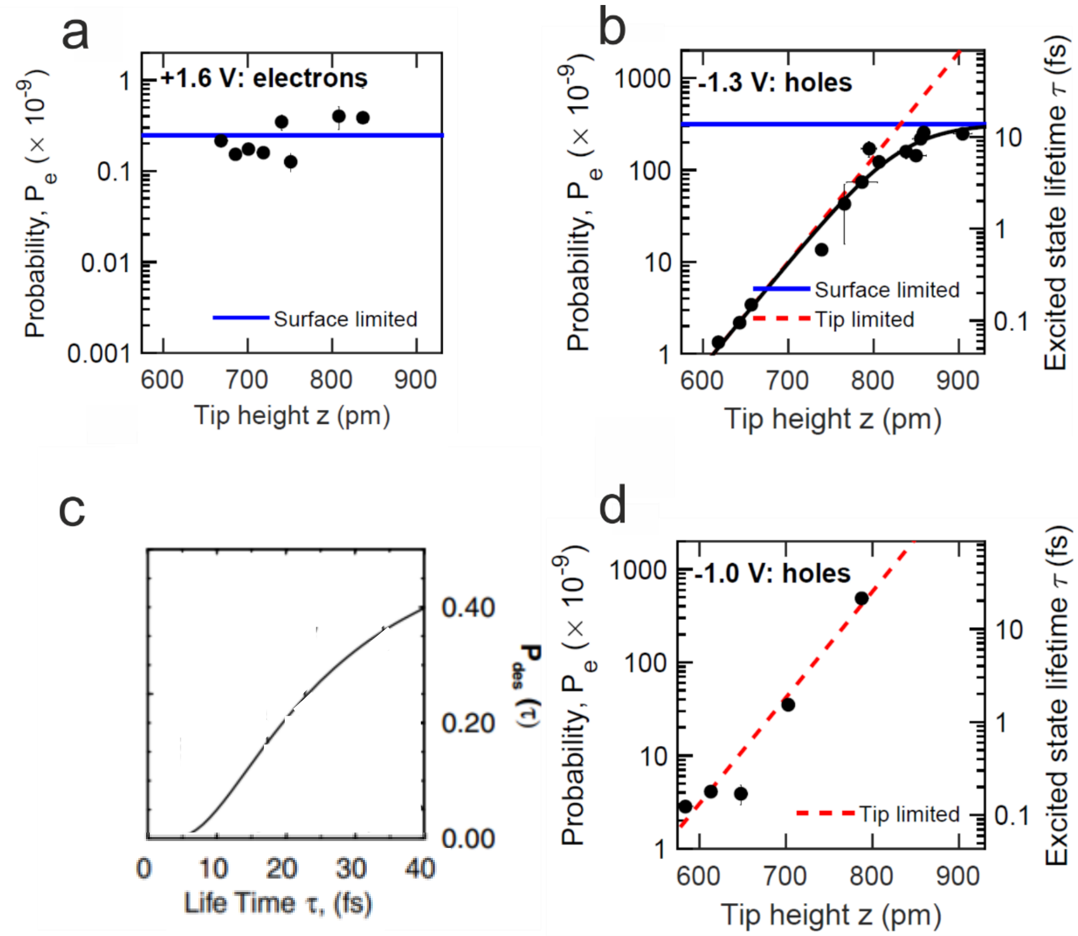

Figure 58: Probability of manipulation per injected electron as a function of tip height for electrons (1.6V) in a, and for holes (-1.3 V) in b. The electron probability is constant across the tip heights measured. For holes in b, the probability drops as the tip height above the molecule reduces. c: Probability of desorption as a function of the excited state lifetime τ of benzene on the Si(110) surface adapted from [78]. d: Probability per injected electron as a function of tip height for hole injection at -1 V, this displays a reduction in probability as the tip height reduces in a purely tip limited regime. b and c show the excited state lifetime mapped from the surface limited excited state lifetime found in [78].

The manipulation process can be broken down into three stages [14]. *Capture*: An injected hole attaches onto the toluene molecule. *Dynamics*: the excited molecule then follows its excited state potential. *Detachment*: this state decays leaving a vibrationally excited neutral molecule [14]. During this final stage the di-σ bonds can be broken providing enough energy for the molecule to enter the physisorbed state and move on the surface, or to completely leave.

For the electron probability in Figure 58a), the change in tip height does not result in a change in the probability, therefore we suggest that the ‘spot size’ illuminated by the injected charge is not significantly changing with tip height. Therefore, there must be a constant proportion of the injected charge captured by the molecule and for this reason, it is assumed that the first stage of the manipulation process, *capture*, must be consistent for all injections carried out. The constant branching ratio suggests a common final stage, *detachment* (discussed further in chapter 7). Therefore, the unusual plateau behaviour in the rate of manipulation must be influenced while the molecule follows its excited state potential, the *dynamics* step.

The probability of manipulation is influenced by the excited state lifetime [73]. This relationship has been measured by Alavi *et al*. shown in Figure 58c. The group have investigated the local desorption of benzene on Si(100) and theoretically modelled this desorption and 'relocation' (diffusion) mechanism on potential energy surfaces of the system [78]. The longer the lifetime, the greater the probability of observing a desorption event with a roughly linear relationship (Figure 58c) [78]. This schematically makes sense in the DIET model in Figure 48a, as the longer the molecule lives in the excited state, the more chance it has of overcoming the energy barrier to desorption before it drops back down to a vibrationally excited state.

Alavi *et al*. measured the excited state lifetime of benzene on Si(100) to be 10 fs [78]. We relate this to our system of toluene on the Si(111)-7x7 surface corresponding to our maximum hole probability (320 ± 10) x10^{-9} and mapping linearly to the probability by $P_e = \beta\tau$, with $\beta = 32\ x10^{-9} fs^{-1}$. Hence, the excited state lifetime is reduced by over two orders of magnitude, down to less than 0.1 fs, as shown by the second axes on Figure 58b and d.

Another similar system was studied by Ryan *et al*. with 1,3 cyclohexadiene on the Si(100) surface, another carbon ring based molecule adsorbed by di-σ bonding [81]. The group modelled the tip/molecule system with DFT (density functional theory) and measured PDOS (partial density of states) maps of charge above a carbon atom in a carbon-carbon double bond of 1,3 cyclohexadiene, to understand the electronic distribution due to the proximity of the tip to the molecule. As the tip approached closer above the molecule, the distribution of π, π^* states broadened and it was seen that an interface state labelled Ψ_2 on Figure 59 emerged at 0.2 eV, just above the Fermi level. This generation of an interface state would open up a new tip-dependant decay channel for the excited state of the molecule.

We propose that in our system of toluene molecules on the Si(111)-7x7 surface, the relaxation rate R of the molecule from the excited state must consist of two contributions: a rate due to the sample $R_s = 1/\tau_s$, and a proposed rate due to the presence of the tip $R_t = 1/\tau_t(z)$, where $R = R_s + R_t$, and τ_s and $\tau_t(z)$ are the sample dependant lifetime and the tip dependant lifetime respectively. The decay channel to the sample must be constant as this route would be the same for any charge injected into toluene on Si(111)-7x7, measured as 10 fs by Alavi *et al*. [78].

The R_t, tip related decay channel must change depending on the proximity of the tip to the molecule, as this provides an alternative decay route through the creation of an interface state when at close proximity [78]. Following from Fermi's golden rule for transition rate, or transition probability per unit time, this term must be dependent on the LDOS of the final state of the transition, that is the density of states of the interface state $\rho_i(z)$.

Jelínek *et al*. have derived a relation between the chemical force and the tunnelling current above an atom using a wavefunction overlap argument of the tip and atom, where $F \propto I^m$, with m between 1 to 2 [79]. This model is similar to the perturbative physics resulting in the formation of this new interface state, so we make the connection that $R_t(z) \propto \rho_i(z) \propto I^m \propto exp(-2\kappa z)^m$. This allows us to write the lifetime of the excited state τ as,

$$\tau = \frac{1}{R} = \frac{1}{R_s + R_t(z)} = \frac{1}{\tau_s^{-1} + Aexp(-2\kappa z)^m} \tag{6.7}$$

where A is a proportionality constant, and τ_s is the 10 fs excited state lifetime as measured by Alavi *et al*. [78]. Returning to the linear mapping of the probability per injected charge, $P_e = \beta\tau$, we can write

$$P_e = \frac{\beta\tau_s}{1 + A\tau_s exp(-2m\kappa z)} \,. \tag{6.8}$$

At large z separations we must return to the $P_e(z_{large}) = \beta\tau_s$ case, and we define a length scale z_0, so that $P_e(z_0) = P_e(z_{large})/2$. This gives the proportionality constant $A = \tau_s^{-1} exp(2m\kappa z_0)$, resulting in the probability per injected charge,

$$P_e = \frac{\beta\tau_s}{1 + exp(-2\kappa m(z - z_0))} \,. \tag{6.9}$$

The equation of this form shows that at larger z tip heights, the constant sample contribution dominates the probability. In contrast, the smaller tip height values with larger tunnelling currents are dominated by the tip contribution. This reduces the probability roughly linearly and therefore the tip limited and sample limited regions are highlighted on Figure 58b in red and blue respectively.

A similar analysis has been carried out by Paul *et al*. measuring the excited-state lifetime of spin states of iron atoms of MgO films [80]. This excited state lifetime is also influenced by the presence of the STM tip above an iron atom, reducing the lifetime by seven times when at close proximity, in a tip limited regime. At further distances the lifetime plateaus by a sample dominated contribution, as measured in our experiments.

Figure 58d shows that for hole injection at -1 V, the probability of manipulation remains in the tip limited regime for all the tip heights probed. This voltage is achieved at closer distances to the molecule and hence the tip does not reach a far enough distance from the molecule for the sample contribution to dominate and a plateau to be observed. The rate for this -1 V experiment is (18 ± 4) s^{-1} compared to (9.5 ± 0.7) s^{-1} for the plateau region of the -1.3 V injection and hence this suggests that the plateau behaviour does not occur because of experimental constraints within our experiment.

We propose that this indicates that the presence of the tip is quenching the excited state lifetime of the molecule by the creation of an interface state at the Fermi energy, as suggested by the work of Ryan *et al*. [81]. The onset of this new interface state, we propose, offers a new tip dependant channel for the excited state of the molecule to decay to, therefore quenching the natural lifetime of the molecules excited state. In the paper written and submitted to document this work, fitting to equation (6.9) with κ = 1.17 ± 0.06 $Å^{-1}$ (the decay constant in the tunnel junction found for hole injection from Figure 57a), gives m = 1.1 ± 0.1 and z_0 = 830 ± 20 pm corresponding to the distance at which the tip limited regime switches to the surface limited regime [72]. Given that at small separations in the tip limited regime the probability tends to a $1/I^m$ dependence, returning to the plateau in k, with its definition from equation (6.6), this now simplifies to $k \propto I/I^m$ during this regime. Hence, hole injection results in a constant rate with $k \propto I^{(-0.1\pm0.1)}$ giving a roughly constant plateau for this tip limited regime. This fitting is shown in Figure 60 [72].

The ability to influence this excited state opens new methods of controlling matter and probing and controlling reactions at the molecular level. It also suggests that it may be possible to influence manipulation outcomes if the excited-state lifetime can be controlled by the presence of the STM tip and not just left to evolve naturally. Hence, it may be possible to favour a particular outcome event.

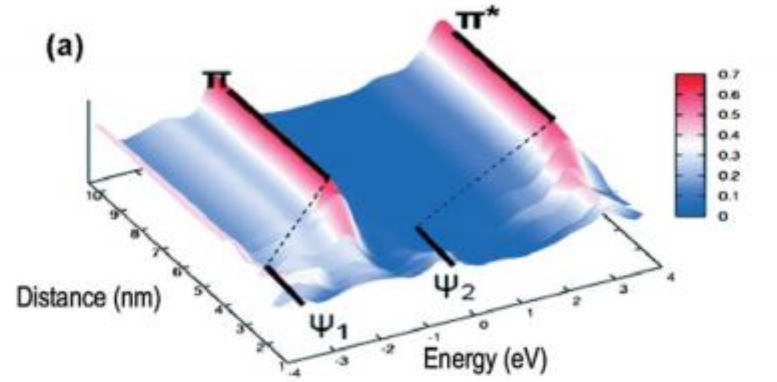

Figure 59: Partial density of states map of charge above a carbon atom in a carbon-carbon double bond of 1,3 cyclohexadiene on Si(100). As the distance between the tip and molecule reduces, the π and π states broaden and a new interface state ψ_2 emerges. [81]*

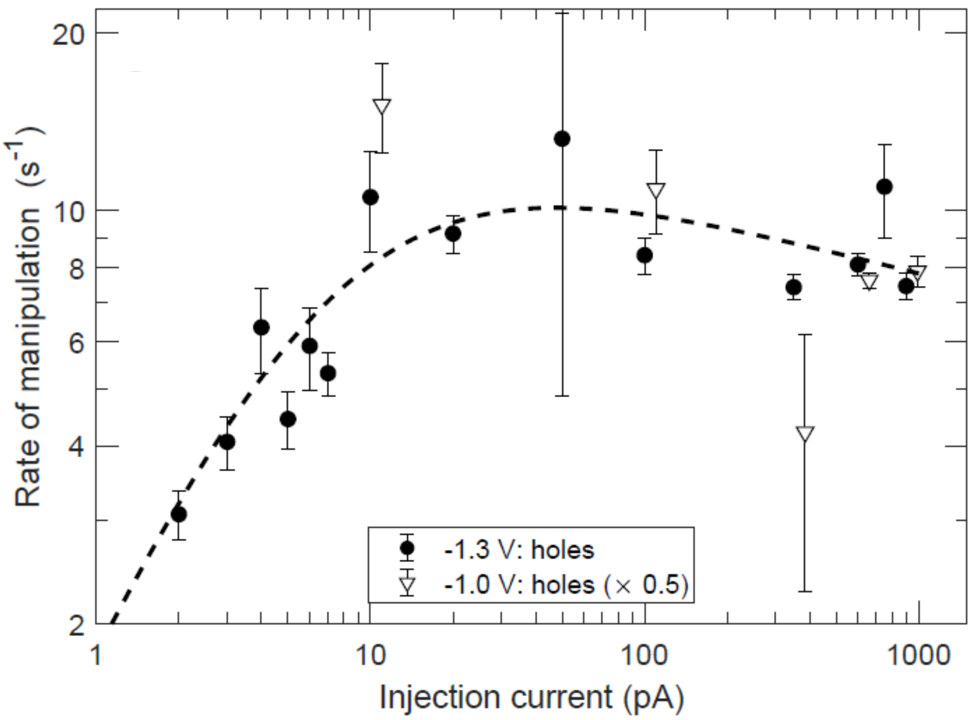

Figure 60: Rate of manipulation of toluene molecules on the Si(111)-7x7 surface as a function of the injection current for both -1.3 V (circles) and -1.0 V (triangles) hole injection. The dashed line indicates the fitting to equation(6.9) with $\kappa = 1.17 \pm 0.06$ Å^{-1}, m = 1.1 ± 0.1 and $z_0 = 830 \pm 20$ pm, following a $k \propto I^{(-0.1\pm0.1)}$ trend with a roughly constant rate above 10 pA injections. [72]

Chapter 7

Branching Ratios

The ability to influence the excited-state lifetime as documented in chapter 6 suggests that it may be possible to influence the outcome of the reaction. Not only do we want to detect whether a manipulation event *did* or *didn't* happen, we'd like to measure *what* happened and *how*. Work done in this chapter investigates the branching ratio of manipulation event outcomes (the ratio of diffusion to desorption events), to see if they can be influenced, including a literature review of groups that have also investigated branching ratios and how this can be influenced within their experimental system.

The branching ratio is investigated for toluene molecules on the Si(111)-7x7 surface as a function of voltage and is found to be invariant. This ratio is explored as a function of other experimental parameters such as tip height and position and remains constant. This suggests that the final stage of the manipulation process must be common for each outcome across all the voltages probed in the experiment.

7.1 Literature Review

Anggara *et al*. have reported on the bond-selectivity of meta-diiodobenzene (mDIB) on Cu(110) [82]. At low temperature, 4.6K, this molecule physisorbs on the surface in a diagonal orientation, shown in Figure 61a. One of the C-I (carbon-Iodine) bonds is along the copper row (AL) with the second C-I bond 126^{0} clockwise from the first, noted as across the Cu row (AC) [82].

The STM tip was positioned above the midpoint of these two lobes, at *x*, with a bias ≥1 V and two outcomes were observed. In Figure 61b the AL bond is broken and then in Figure 61c, the AC bond. Out of 139 reactions, only 1 bond was broken each time, predominantly the AL bond with 99.3% probability. The resultant parts of an iodine atom and IPh molecule recoiled along the row by 4.7 Å.

When compared to a second configuration of physisorbed bonding, in a 'row' orientation, there was no preference in the bond breaking and hence the bond selectivity demonstrated here was concluded from the asymmetric bonding configuration of the mDIB on the Cu(110) surface. A linear rate as a function of tunnelling current shows this was a 1-electron process, with DFT revealing that the addition of an electron on the iodine atom breaks the AL bond. For the AC bond, an additional electron did not break the AC bond as this is further from its nearest neighbour copper atom and hence has an altered binding energy, therefore the AL bond breaking was favoured.

This is an inherent preference due to the energy make-up of this particular system favouring one type of bond breaking. Although the STM instigates a manipulation, the branching ratio is set by the bonding configuration of the molecule, which cannot be user controlled. Other groups have looked at manipulation where an outcome can be actively preferred from user actions of the STM, Pascual *et al*.

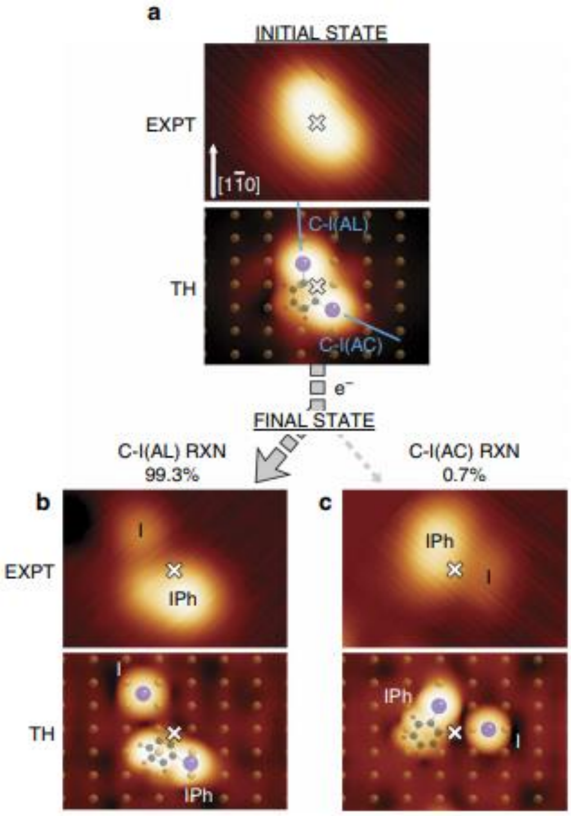

Figure 61: Manipulation of mDIB molecules on Cu(110) at 4.6 K. a) The molecule physisorbs in a diagonal orientation on the surface with an experimental STM image and theoretical schematic shown. When the tip is located above the middle of the molecule at 'x' and injects at ≥1 V, two outcomes are seen: b) the AL bond is broken along a Cu row, or c) an AC bond is broken across a Cu row. [82]

are an example [83]. The group used ammonia molecules on the Cu(100) surface at 5 K. They observed both diffusion and desorption of the ammonia with a threshold charge injection. With injected tunnel current <0.5 nA, diffusion resulted as a consequence of a 1-electron process, whereas higher tunnel currents resulted in desorption, as a consequence of a 3-electron process. These thresholds were concluded to correspond to exciting different vibrational bonds of the molecule. When injecting below 0.5 nA the ratio of the two outcomes was one third, compared to three when injecting at greater currents, corresponding to the two different modes. These different branching ratios are observable by injecting at a different user specified current, but are still set by the molecule/substrate system.

Another system where user specified STM conditions can control reactions is the system of PH_3 molecules on Si(100) [84]. Here the group have controlled the dissociation of the PH_3 molecule between 5 different configurations, illustrated in Figure 62, by the injection of different voltages for differing injection times. The solid lines show common reactions induced by different voltage pulses and the dotted lines show more infrequently observed reactions. In some cases (2 and 6) the PH component is manipulated as an entity, whereas in other cases (4 and 9) all P-S and P-H bonds are broken. To measure the reaction times, again the tunnelling current was monitored above the molecule until a drop was detected, indicating a manipulation event. Using this, the dissociation rate was found from the inverse of the dissociation lifetime. The group concluded the dissociation methods for each situation using 1st principle calculations to decipher the vibrational modes responsible for the dissociations. Here, user controlled reactions, whereby different voltage and duration pulses can induce a certain outcome, are exploited to control the manipulation outcome of this PH_3 on Si(100) system. Ultimately the specific voltage and time required to break a bond is set by the systems itself.

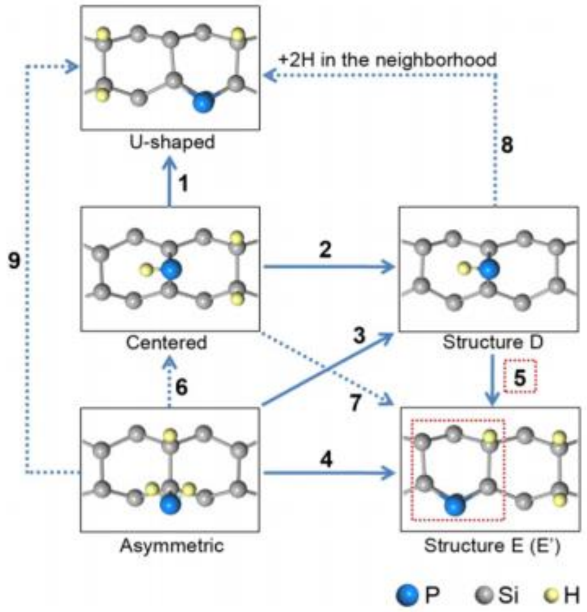

Figure 62: Schematic of all the reactions of PH_3 molecules on Si(100) induced by different lengths of voltage pulses. The solid lines show the most commonly occurring reactions following a voltage pulse. [84]

Finally, as mentioned in section 6.3.1, work by Lock *et al*. has looked at the thermal energy required for desorption and diffusion of benzene, chlorobenzene and toluene on Si(111)-7x7 by time-lapse STM at room temperature [75]. To minimise any tip influence on the system, images were taken every 12 minutes meaning each atomic site was exposed to the tip for 10 ms every 10 minutes.

Each molecule was tracked in the image until it desorbed or until the time-lapse ended. This allowed the group to determine the site dependant rates of chemisorbed molecules leaving their atomic sites via the physisorbed state. The physisorbed state is a weakly bound precursor state to desorption where the molecule can diffuse across the surface. Figure 63 shows a schematic of the energy barrier to both the chemisorbed and physisorbed states. At room temperature the lifetime of the physisorbed state was estimated as 1 μs and is therefore too short lived to be imaged [75], however this has been achieved using low temperature STM.

Time dependant population and Arrhenius plots enabled conclusions on the site dependant rates for chemisorption to be drawn, with rates of FM>FC>UC>UM for toluene molecules. The physisorbed state was investigated indirectly by looking at the number of molecules that left into the gas phase and the number of new molecules that appeared in the images, hence comparing the outcomes of the physisorbed state as this cannot be imaged directly at room temperature. In other words, this was the number of molecules that desorbed (into the gas phase) compared to the number that diffused (new molecules in the image).

By looking at the Arrhenius rate equations for these two outcomes, the energy difference between the barrier to desorption compared to diffusion from the physisorbed state was seen to show an energetic preference to chemisorption, hence molecules diffuse to a new site. Therefore, the barrier to diffusion must be lower than the barrier to desorption from the physisorbed state, as can be seen from Figure 63, where E_β is smaller than the barrier to reach the gas phase from the physisorbed energy well, E_λ.

For this reason the branching ratio of toluene on Si(111)-7x7 was explored. Changing the injection voltage will alter the energy of the injected electrons and hence at lower voltages it is predicted that

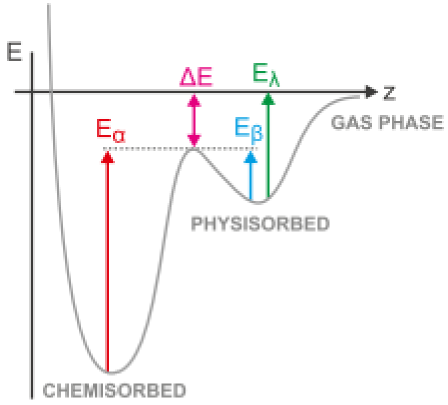

Figure 63: Energy barrier schematic illustrating the energies required to chemisorb, physisorb or fully leave the surface into the gas phase. [75]

we should be able to preferentially select the diffusion of toluene molecules once injections are below the energy barrier to desorption. Therefore, we investigate whether can exploit the toluene on Si(111)-7x7 system to control the outcome observed by providing enough energy to initiate only diffusion, an energy barrier parameter set by the molecule/substrate system.

7.2 Experimental Improvements

7.2.1 Site Injection

All the work done in chapter 6 was carried out on faulted middle sites. The di-σ bonding of toluene molecules on silicon to one rest atom and one adatom, as explained in Figure 38b, illustrates that on this binding site there are two crystallographically equivalent bonding configurations [85]. This arises from two equivalent rest atoms that can form the second bond for any given FM adatom, as shown schematically in Figure 64.

Rusimova *et al*. has reported that the expression of these two binding sites becomes apparent when looking at the fraction of manipulated molecules as a function of time (a decay curve, as in Figure 56a – note, the paper reports the fraction of molecules that remain rather than the fraction of molecules manipulated) in Figure 64d) [85]. These manipulation injections were carried out slightly off centre from directly above the bonded adatom. Indicated by the red star, these off-centre injections differentiate between these two binding configurations, one directly above the bonded molecule and the other, into the bonded adatom.

The two bonding sites manifested themselves in effectively two different populations of bonded molecules and hence the decay curve fits with a double exponential rather than a single, one for each population [85]. This can be written as,

$$\frac{N(t)}{N_0} = \frac{N_0^A}{N_0} exp\left(-\alpha_A \frac{It}{e}\right) + \frac{N_0^B}{N_0} exp\left(-\alpha_B \frac{It}{e}\right) \tag{7.1}$$

where *N(t)* is the number of molecules that remain after time *t* and injection current I. N_0 is the total number of manipulated molecules, N_0^A and N_0^B are the initial number of molecules of populations *A* and *B* respectively, with the probability of manipulation α_A and α_B for each population [85]. One exponential corresponds to a fast decay and the other, slow. Using low temperature injection data

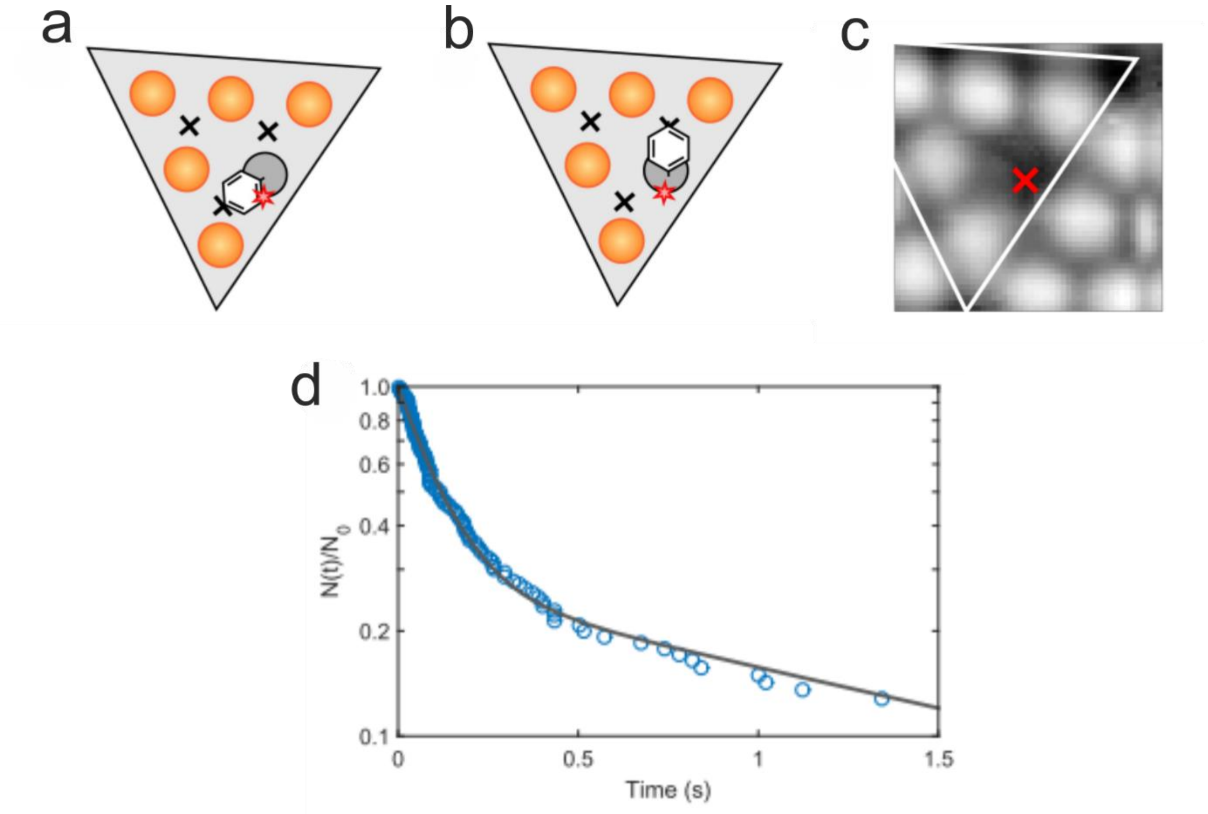

Figure 64: a) and b) show the two crystallographically equivalent bonding configurations of toluene on Si(111)-7x7. c) shows a 5 nm STM image of a toluene molecule on a faulted middle site. The star indicates the injection location which differentiates between these two bonding configurations. d) shows the fraction of molecules that remain on the surface as a function of time, which exhibits a double exponential for the two populations corresponding to the two bonding configurations. [85]

at 77 K that induces adatom hopping (as seen in [36]), found a similar decay rate for both molecule injection and bare adatom injections. The slow rate was therefore identified as corresponding to the adatom injections and the fast decay rate to the molecule site injections. See reference [85] for a more detailed discussion. This motivates the work I have carried out on the FC sites, which have only one possible bonding orientation, as shown in Figure 65a and b. For injections carried out at -1.2 V and 20 pA, it can be seen from Figure 65c) and d) that single exponential behaviour is confirmed in comparison to the double exponential behaviour on the FM sites. The goodness of fit for single: 0.97768, and for the double: 0.9162.

7.2.2 Injection Accuracy Improvements

Further steps taken to increase the accuracy of the injection location include altering the scan speed for the 'before', 'during' and 'after' scans for each injection. To minimise the shift between the forwards and backwards scan direction, a 15 nms^{-1} scan speed was chosen. This corresponds to a shift of ~0.44 Å, seen from Figure 66, plotting the forwards and backwards scan shift as a function of the scan speed. This shift distance is smaller than the diameter of the molecule.

When carrying out injections, additional autocorrelation is carried out on each injection site with 3 nm images, prior to the 'before' scan starting. This ensures that any further drift since the large 'before' image is compensated for.

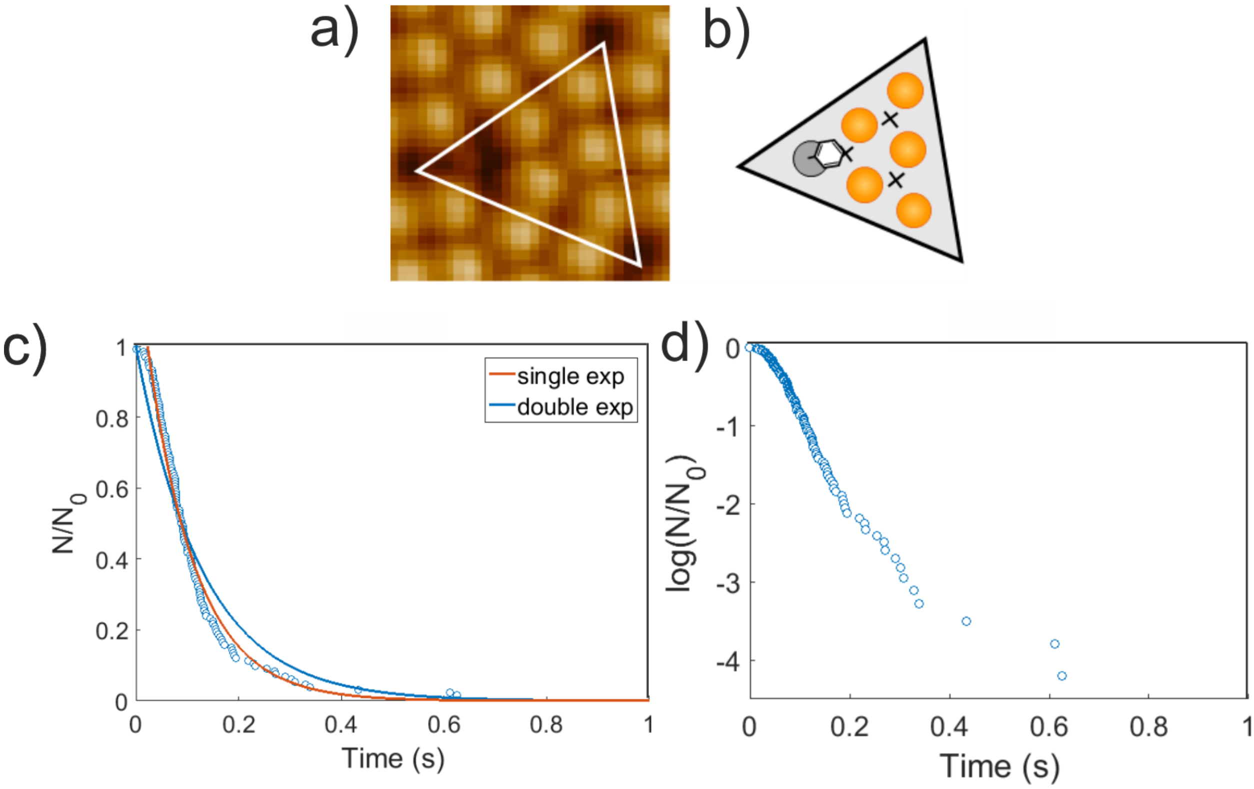

Figure 65: a) 5 nm STM image of a toluene molecule adsorbed onto a FC site and b) the schematic bonding configuration for this site. c) shows the fraction of molecules manipulated as a function of time for -1.2 V and 20 pA injections on FCs and the data displays single exponential behaviour. This data is plotted again on a logarithmic y axis in d) showing the single exponential behaviour as a function of time.

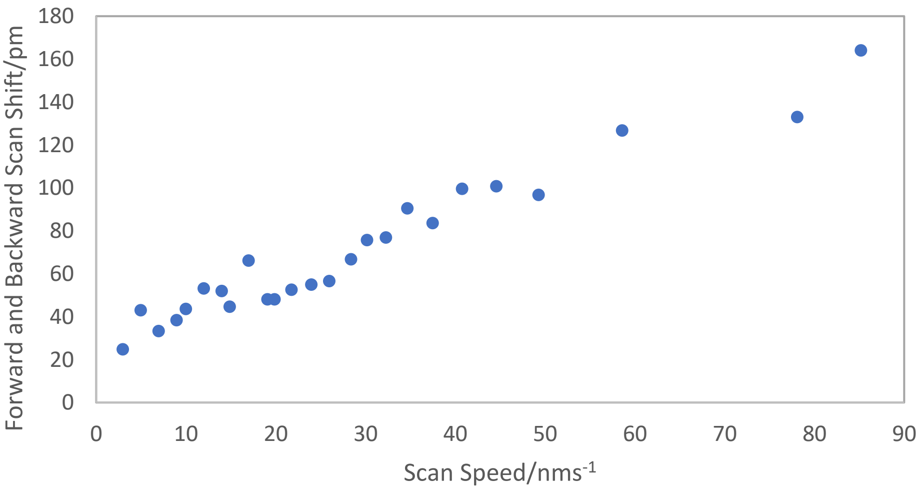

Figure 66: Shift between forwards and backward line scans as a function of the scan speed.

7.2.3 Stopping Injections

As has been discussed, the adatoms can undergo manipulation themselves [36]. As documented by Rusimova *et al*. [85], manipulation occurs by populating the back-bond state of the silicon adatom peaking at 2 V. This results in manipulation for all voltages probed in the paper when injecting into the bonding adatom, as can be seen from the adatom scanning tunnelling spectroscopy (STS) data in Figure 67b, where the shaded blue state peaks at 2 V, but extends across the 1 to 2.2 V range plotted. STS measurements allow the local density of states of the sample to be found as a function of voltage. From equation (2.20), it follows that

$$\frac{dI}{dV} \propto g_E(z, E_F) \tag{7.2}$$

The tip is held at a fixed height positioned above a location of the sample and the tunnelling current measured as a function of bias voltage. The gradient of the I-V curve obtained is then used to determine the LDOS of the surface as a function of voltage. Further details of this analysis technique can be found in [86] where Feenstra documents a variable height STS technique to enhance the signal from low voltages without having to increase the acquisition time of the measurement. This variable height STS technique was the method used for obtaining this STS data, and the other STS plots presented in this thesis [97].

When injecting directly above the molecule, the voltage thresholds determined by Rusimova *et al*. reveal that molecular manipulation only occurs above 1.4 V [85]. The STS data in Figure 67a reveals that the lower lying 1.2 V state is molecularly inactive and does not result in manipulation, until injection above 1.4 V, where the 2 V back-bond state can again be populated from charge injection. It is concluded that it is the electronic excitation of the silicon adatoms that ultimately results in the manipulation of toluene molecules on the Si(111)-7x7 surface for electron injection [85].

It is this reason that suggests why the quenching behaviour explained in chapter 6, was only present in the hole injection data. For electron injection, the excitation occurs in the surface, when the 2 V state is populated [85], whereas for hole injection, the molecule itself is excited to induce manipulation [43]. Hence the tip approaches closer distances to the molecule excitation resonance for hole injection than to the sample resonance for electron injection at high tunnel current values, meaning the quenching behaviour is only observed for hole injection. Consequently, the branching ratio is investigated for electron injections so we are not perturbing the system, but just observing the natural outcomes following electron injection.

All the manipulation injections discussed in this thesis so far, have involved an 8 s injection time to capture the manipulation events for the voltages probed. If it is the excitation of the underlying surface that results in these manipulation events, then to truly investigate the branching ratio of the manipulation outcomes, the injection must be halted immediately after the manipulation in order to prevent further electrons impinging on the injection site.

The automated LABVIEW vi for manipulation injections was altered to increase the sampling rate to 10,000 Hz and minimise wait times within the script to increase the passing of information between the *Nanonis* electronics and the computer to every 25 ms. The process of injection from section 6.2 was improved by altering step (ii) so the tip no longer initially approaches to 20 pA to avoid over shooting, but instead, the feedback loop is reduced following the tips retraction by 1 nm from the surface. This allows the tip to approach the required injection parameters smoothly to start the injection. Every segment of 25 ms sampling time, the LabVIEW program calculates the average *z* height

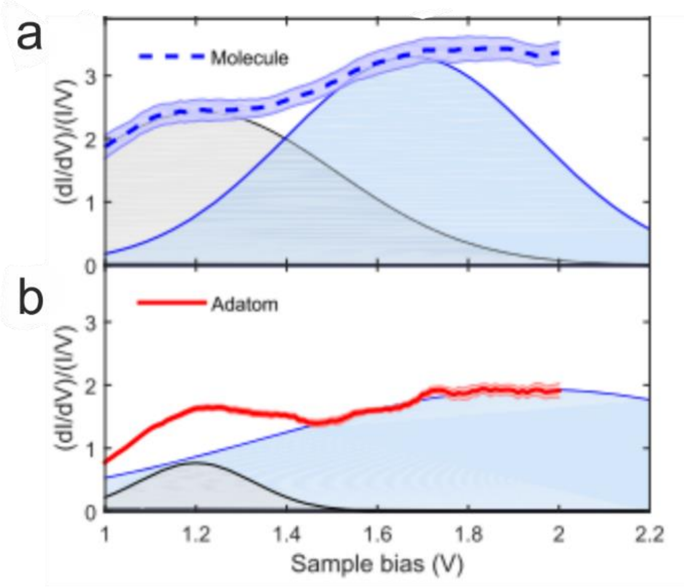

Figure 67: Scanning Tunnelling Spectroscopy data above a molecule (a) and an adatom (b) from [85].

for that time segment and compares it to the average *z* height for the very first 25 ms of the injection to find Δz_M on Figure 55, the height of the tip retraction during a manipulation event. If this Δz_M value is larger than the user specified delta *z* trigger, then the injection halts as a manipulation event has been detected. The current is then set to 5 pA while the feedback loop is turned off and the tip is retracted 1 nm away from the surface. The current and voltage are then re-set back to passive imaging parameters of 1 V and 100 pA as before.

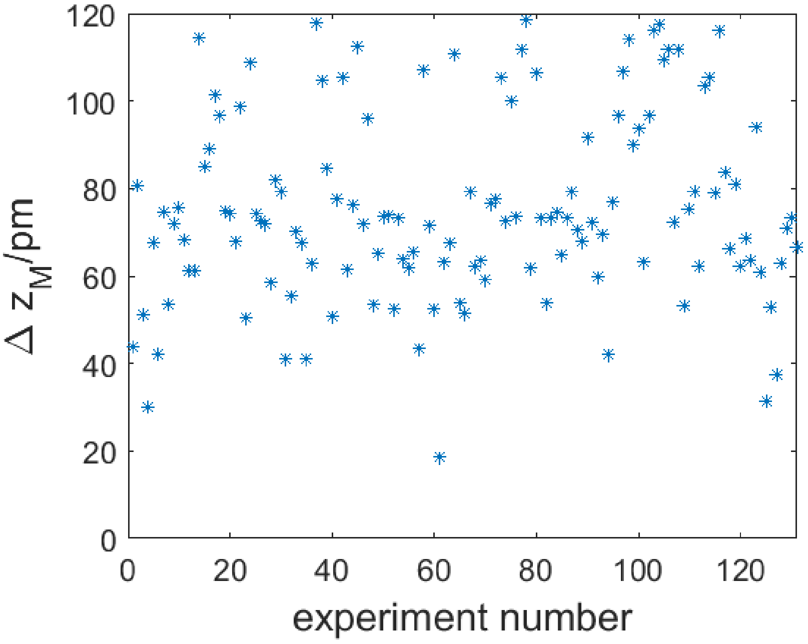

Figure 68: Change in z height of the tip at the point of manipulation, Δz_M for each -1.2 V and 20 pA injection.

Using the -1.2 V, 20 pA injection data, the Δz_M heights were extracted and plotted in Figure 68 revealing 30 pm as an appropriate value at which to trigger the stopping of the injection. The variation in these points may occur from different tip states or from slight variation in the injection site position still occasionally present during injections.

7.3 Results

To accurately measure the branching ratio, we want to identify the very first manipulation event, and only consider the time-to-manipulation providing that the injection was halted as fast as possible following the Δz_M retraction. This allows us access to assign the outcome to the time-to-manipulation, whereas in previous injections, the remaining injection time could cause further manipulation and hence the after image would reveal a different outcome to the outcome that corresponds to the first tip height retraction. To ensure that the injection was halted as fast as computationally possible, the time-to-manipulation step was only counted providing the time of the 5 pA section was of equal time duration as the tip height following the retraction, i.e both occur as fast as the feedback loop and recording measurements allow. An example of these are shown in Figure 69: **A** shows a manipulation induced tip retraction of equal length to the 5 pA section, the ideal tip height trace. **B** shows the manipulation induced retraction for a much longer duration than the 5 pA section, as indicated by the arrow, therefore this trace would not be counted as further manipulation could be induced from the excess injection of charge following the initial manipulation. **C** shows the tip retraction from multiple manipulation events too small in height to trigger the halting of the injection, therefore this trace would also not be counted as the ‘after’ image refers to the outcome following three manipulation events, not the initial event.

To achieve reliable cut-off of the current, the Δz_M values were altered for the different voltages. Low voltages used Δz_M of 10 pm which was decreased to 2 pm for the larger voltages injected as the tip is further away from surface and so a smaller retraction is seen. To ensure these small tip height retractions were visible on the trace, the drift tracking software that runs prior to the injection automation was left until an x and y shift of 30 to 60 pm, and a z shift of 1 – 2 pm.

7.3.1 Voltage dependence

This new ‘inject and stop’ program was used for 750 pA injections at FC sites in a voltage range of 1.4 to 2.2 V. Over the voltage range probed in Figure 70A), the branching ratio of outcomes can be considered constant (0.27 ± 0.03), with an error calculated by binomial probability. Injections were also done at 1.2 V and 1.3 V, however in the maximum injection time of 8 s, very few manipulations were observed for 1.3 V and even less for 1.2 V and hence no further investigations were carried out at these low voltages. Voltages above 2.2 V were also probed but as this enters the non-local regime above 2.1 V [85, 87, 96] many manipulation events were occurring very rapidly. This, combined with the tip achieving higher voltages at distances further from sample, meant a delta z value of 1 pm was required to trigger the stopping of the injection (when detecting a Δz_M retaction) which became lost within the background shift or noise in the height trace signal.

The probability per injected electron of causing a manipulation P_e, for the same voltage range increases exponentially with increasing voltage in Figure 70B). Although the probability of a manipulation occurring increases for larger injection voltage, the ratio of the observed outcomes remains roughly constant, despite the increase in energy of injected charge.

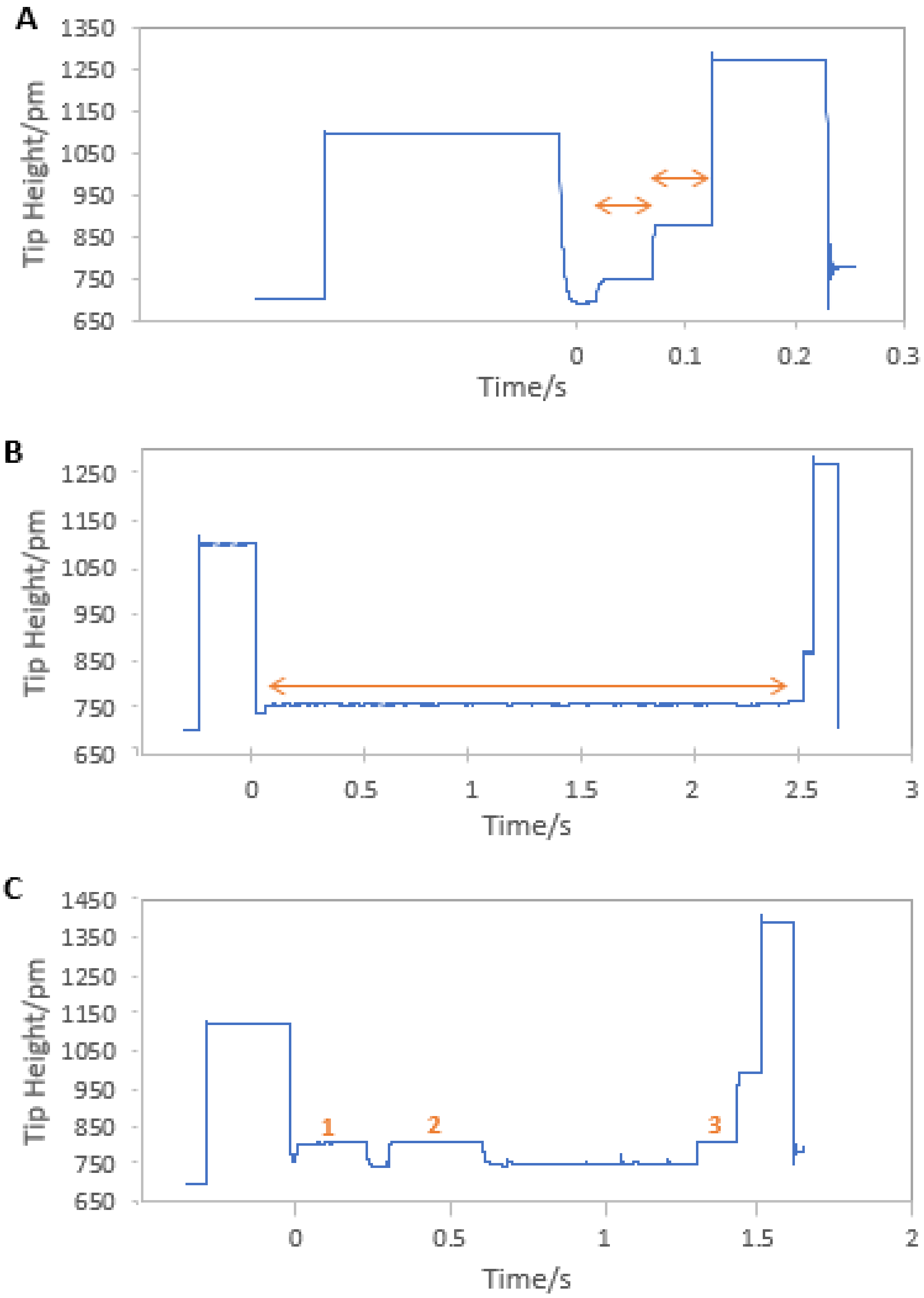

Figure 69: Example tip height traces during injection. Ideally, the trace should have a retraction step at the point of manipulation of equal length to the 5 pA retraction as this shows that the feedback loop has operated as fast as computationally possible, halting the injection as soon as the manipulation event has been detected. This is seen in A, where the arrows indicate steps of equal length. B shows a trace where the manipulation step highlighted by the arrow was much larger than the 5pA step, and hence other manipulation events could be occurring here as the injection was not halted fast enough, therefore this trace would not be included as a data point. Similarly, in C, two other manipulation events are also visible that were not large enough retractions to trigger the stopping of the injection until a third event. Therefore, this trace would also not count towards a data point as multiple events occurred during the injection.

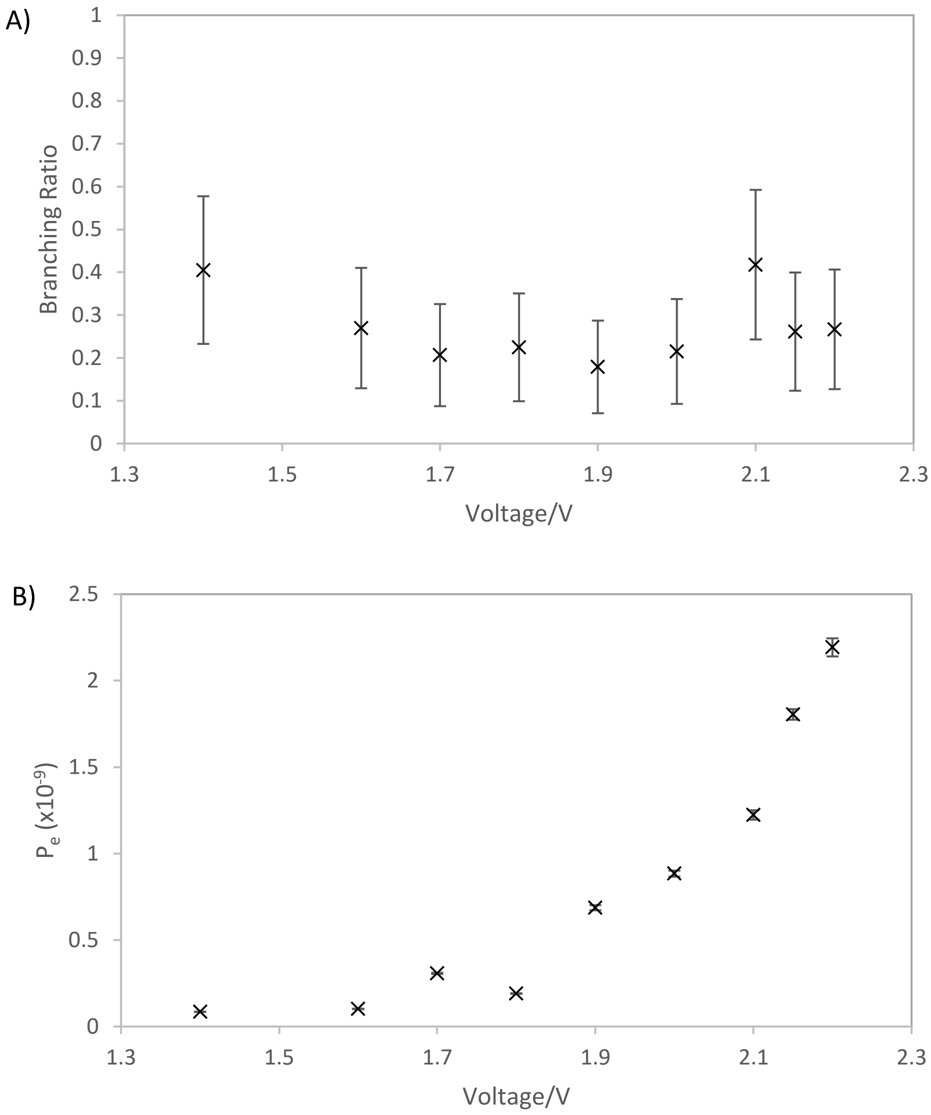

Figure 70: A): Branching ratio, the ratio of diffusion to desorption outcomes as a function of injection voltage. The branching ratio appears to be invariant to the injection voltage. Manipulation wasn't seen below a voltage threshold of 1.4 V. B): Probability per injected electron of causing a manipulation P_e, as a function of injection voltage. The probability increases exponentially as the bias increases.

7.3.2 Tip height dependence

Recasting the data plotted in Figure 70, as a function of the tip height z_I above the molecule can be seen in Figure 71. In Figure 71A) the branching ratio remains constant for tip heights probed within this voltage range. It is also noted that the tip remains at a height greater than 600 pm throughout the experiment and hence, as in section 6.3.2, the tip remains far enough away from the surface so as not to perturb the potential energy landscape of the system. The probability per injected electron is shown in Figure 71B) and increases for larger tip separations.

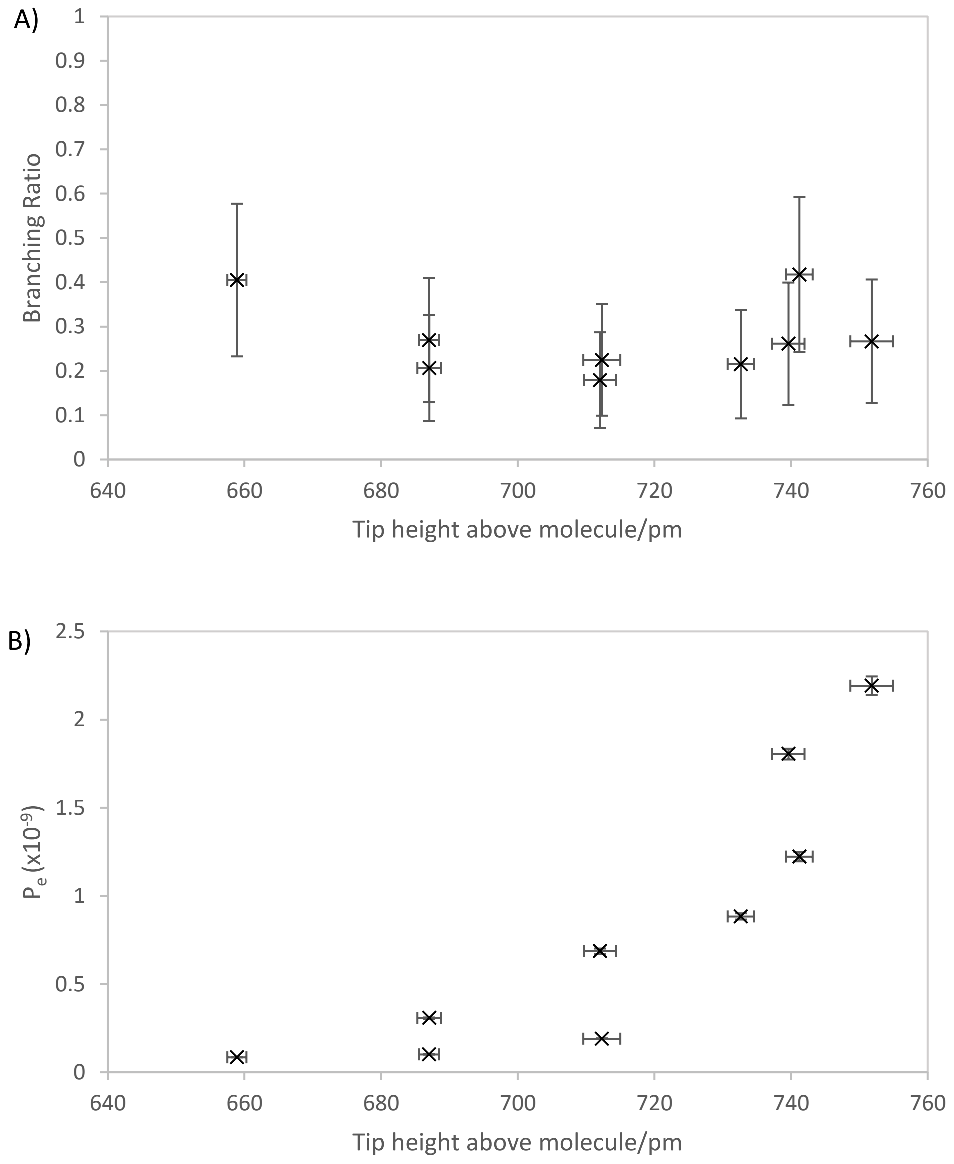

Figure 71: A): Branching ratio and B): Probability per injected electron, as a function of the tip height z_l *above a molecule.*

7.3.3 Electric field dependence

As in chapter 6, the tip height data in section 7.3.2 can be used to plot the electric field dependence, seen in Figure 72. For the corresponding electric fields of the voltage range probed, the branching ratio can again be considered constant in Figure 72A) and the probability increases exponentially in Figure 72B).

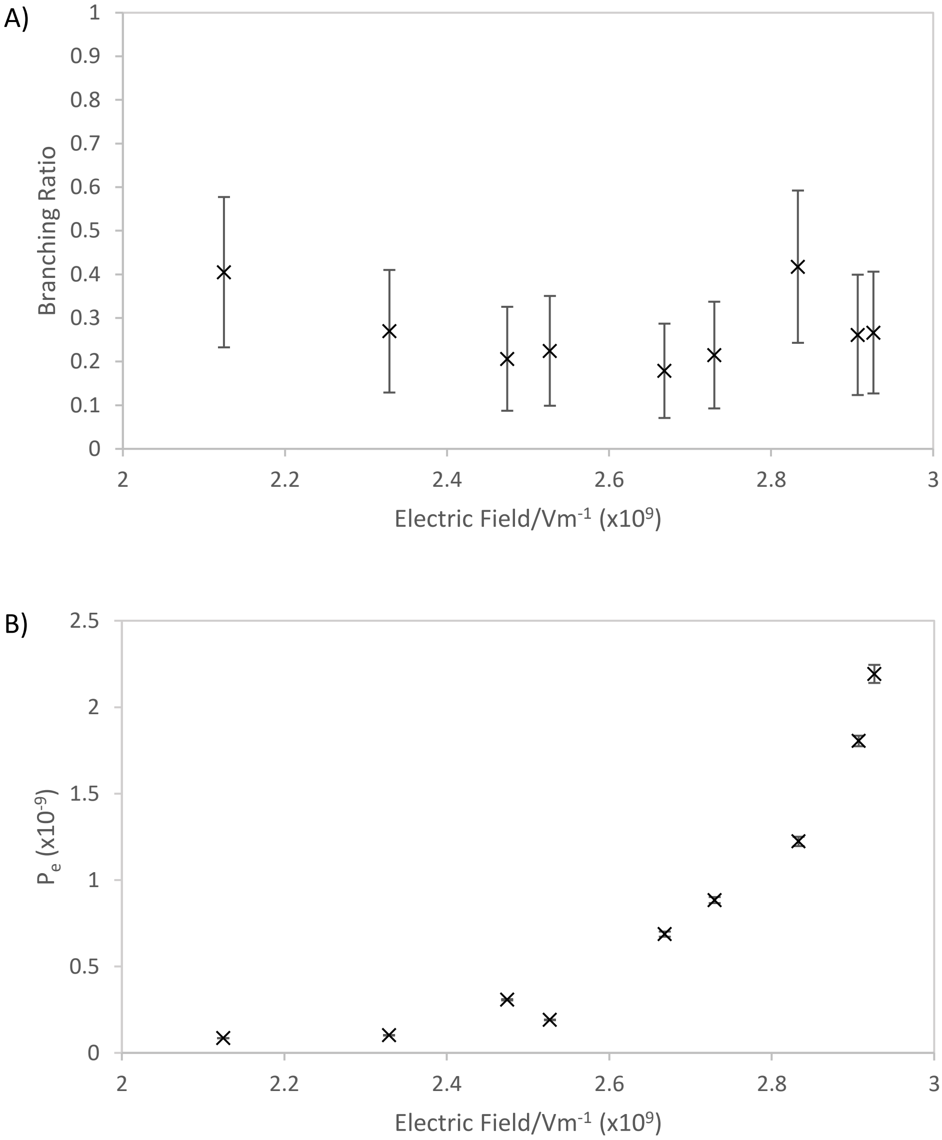

Figure 72: A): Branching Ratio and B): Probability per injected electron as a function of Electric field within the tunnel junction.

7.3.4 Position Dependence

Alongside the current and voltage, the final variable over which we have control is the position of the injection. The injection data taken so far in this chapter has been with the tip positioned directly above the silicon adatom to which the toluene molecule is bonded. Injections were carried out above the rest atom of the bonded molecule and the mid-point between the bonding rest and adatom to compare with the adatom site injections, for an injection voltage of 1.8 V and 750 pA. The branching ratio across these three sites can be seen in Figure 73A and is considered constant, 0.18 ± 0.02. Figure 73B) shows the probability per injected electron as a function of the three injection sites across the molecule, revealing that the probability of manipulation drops when the tip is positioned above an adatom.

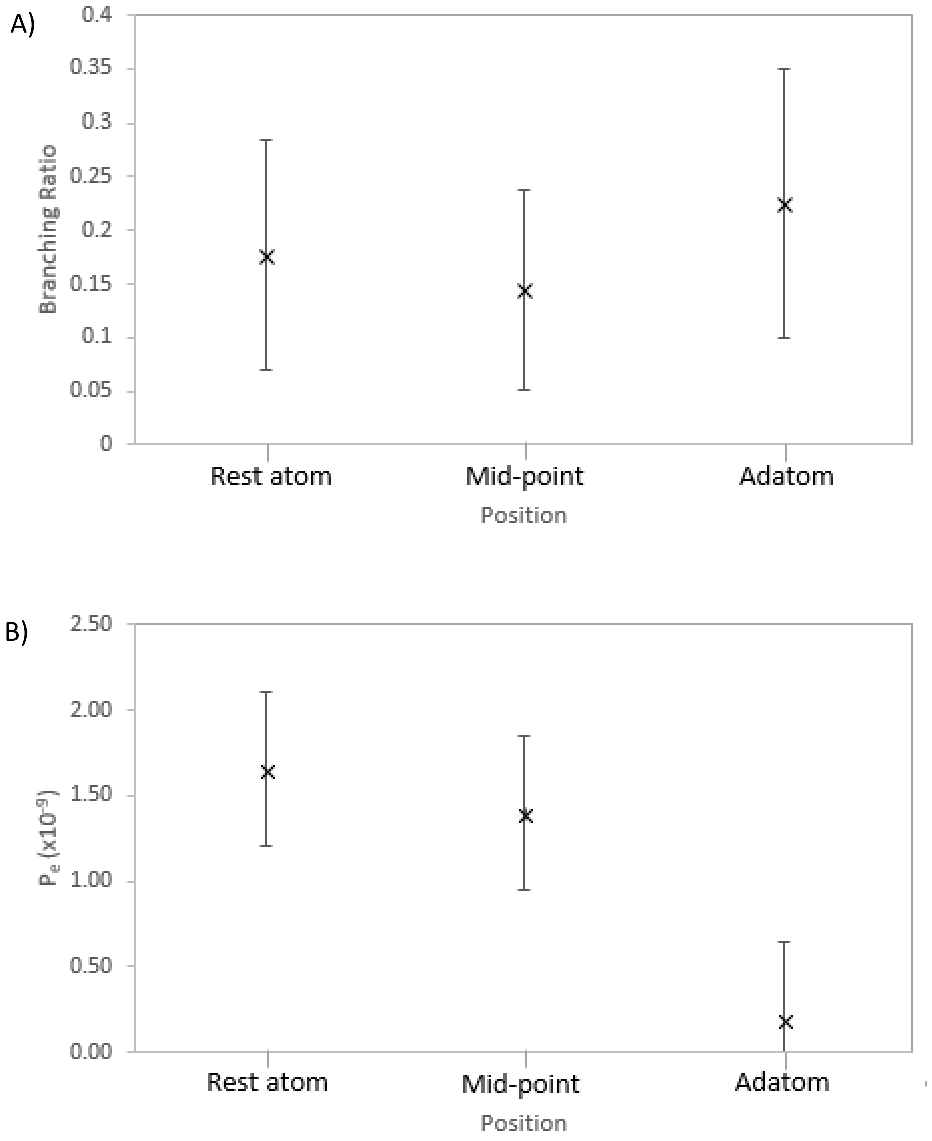

Figure 73: A): Branching ratio as a function of injection position, showing that across the molecule there is a roughly constant branching ratio of manipulation event outcomes. B): The corresponding probability per injected electron for these three injection locations.

7.4 Discussion

Figure 74 shows that the branching ratio is constant as a function of the probability per injected electron P_e to induce manipulation.

The results in Figure 70 to Figure 74 show that the branching ratio for this system of toluene molecules on the Si(111)-7x7 surface remains constant for the voltage range probed and the corresponding change in tip height and electric field and for position dependent injections. Following the 3-stage manipulation process discussed in chapter 6, the *capture* stage must be consistent for all injections, as discussed in section 6.4. In Figure 71 the tip retracts from the surface within a 660 to 760 pm range, encompassed by the range of separation in Figure 58a, where the constant probability in Figure 58a suggested that the ‘spot size’ illuminated by the injected charge must change by an insignificant amount. Therefore, the proportion of charge captured by the molecule within this voltage range for electron injection must also be constant.

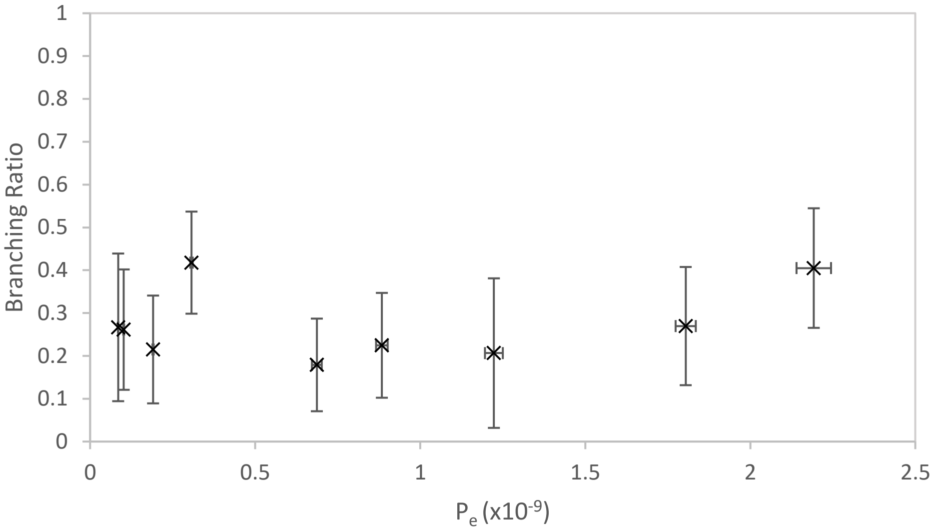

Figure 74: Branching ratio as a function of probability per injected electron for inducing manipulation. The branching ratio remains roughly constant.

Given that electron injections have been carried out, the work discussed in chapter 6 reveals that we are not influencing the excited state of the molecule. For electron injection, the resonance for the excitation is located in the surface and not the molecule as discussed in section 7.2.3, meaning the tip cannot approach close enough to the surface to initiate an interface state [85,81]. Hence, the *dynamics* stage of the manipulation process must also be consistent for all injections. Therefore, we suggest that the constant branching ratio of 0.27 ± 0.03 implies that the final stage of the manipulation process, *detachment*, must be common for all manipulations.

We propose that, as with the non-local manipulation mechanism [43], the injected charge must undergo an ultra-fast relaxation so that the same excited state form triggers the manipulation, hence the branching ratio remains constant. The injected charge similarly must lose energy via non-radiative decay mechanisms such as phonon or electron scattering [43]. Other forms of ultra-fast relaxation have been investigated by Mauerer *et al*. using both second-harmonic generation (SHG) and two-photon photo emission (2PPE), suggesting that electron-electron intraband scattering is a source of ultrafast relaxation in their Si(111)-7x7 system [13].

The proposed manipulation mechanism is illustrated in a schematic in Figure 75. The injected electron undergoes rapid relaxation until it reaches 1.4 V, the minimum voltage required to tunnel into the 2 V back bond state of the system, the same threshold measured by Rusimova *et al*. [85]. The manipulation process occurs when the injected charge then inelastically transitions to a lower lying surface state. In this way, all injected electrons above 1.4 V relax to this point and hence the ratio of outcomes observed is constant for all, as they are all initiated with the same energy electron. This contradicts with our initially proposed theory that we should be able to favour a diffusion outcome due to its lower energy barrier.

The increase in the probability per injected electron of causing a manipulation is explained due to the increased number of electrons that are able to tunnel into the silicon back-bond state at greater voltage injections and therefore can have the opportunity to cause manipulation once they have relaxed to the corresponding 1.4 V energy. The probability therefore rises because *more electrons* can cause manipulation, rather than the electrons now having more energy to be able to cause *more manipulations*. The manipulation is only initiated once the electron has relaxed to 1.4 V. The apparent influence we have on this probability is the voltage, when in fact we propose that the ability for manipulation to occur solely depends on the states in the system probed, just as Anggara *et al*. and Pascua *et al*. [82, 83] have seen within their systems. In this case of toluene molecules on the Si(111)-7x7 surface this manifests itself in manipulation when injecting electrons above 1.4 V, allowing tunnelling to the silicon back-bond state that peaks at 2 V. Any increase in voltage beyond this will result in more electrons undergoing an ultrafast relaxation down to 1.4 V before causing manipulation. Aligning with our proposed mechanism for non-local manipulation [43].

The position dependence of both the branching ratio and probability of manipulation is shown in Figure 73. The constant branching ratio across the three injection locations probed further suggests that the manipulation is initiated with the same energy electron having undergone relaxation in the 2 V state to 1.4 V. The probability however appears to drop when the injection location is above the adatom site, in Figure 73B). Given that the electron resonance is located in the silicon surface [85], it was expected that the mid-point location should exhibit different behaviour to both the rest and adatom site injections, as this mid-point site is not located directly above a surface atom. The charge injected directly above the body of the molecule when injected at the mid-point must couple to the surface in order to excite the resonance and allow manipulation to occur once it has relaxed to 1.4 V and is able to transition from this state. This may suggest that for mid-point injections, the charge couples via the rest-adatom to excite the surface resonance, giving these two injection locations a similar probability per electron of manipulation occurring.

The probability of manipulation across our injection locations above toluene molecules in Figure 73B) correspond to a roughly 1 order of magnitude decrease when above the adatom position. In contrast, as described in section 6.1, the position dependant manipulation of biphenyl molecules on the Si(100) surface documented by Lastapis *et al*. was measured to have a probability difference of 3 orders of magnitude [8]. Huan *et al*. have obtained STS spectra above a naphthalocyanine molecule on an alumina layer on a NiAl(110) substrate, Figure 76 [88]. This highlights the possibility of different surface states being present at different locations above a molecule, however within our system of toluene on Si(111)-7x7 the constant branching ratio measurement suggests that the manipulation process must be the same for each site location, initiated from injected electrons transitioning from the 2 V back bond state once they have relaxed to 1.4 V .

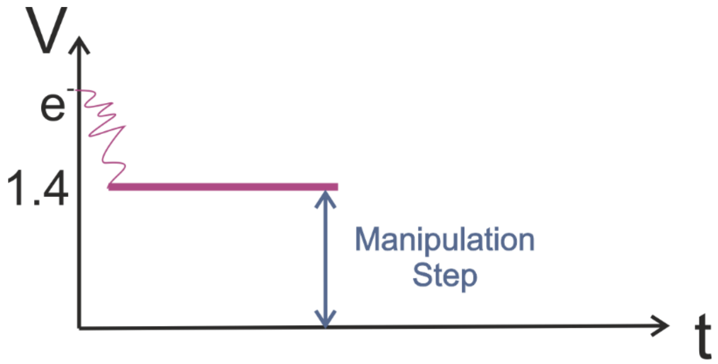

Figure 75: Schematic of voltage as a function of time for the proposed mechanism of local manipulation. The injected electron undergoes an ultrafast relaxation down to the 1.4 V state from which it can induce manipulation.

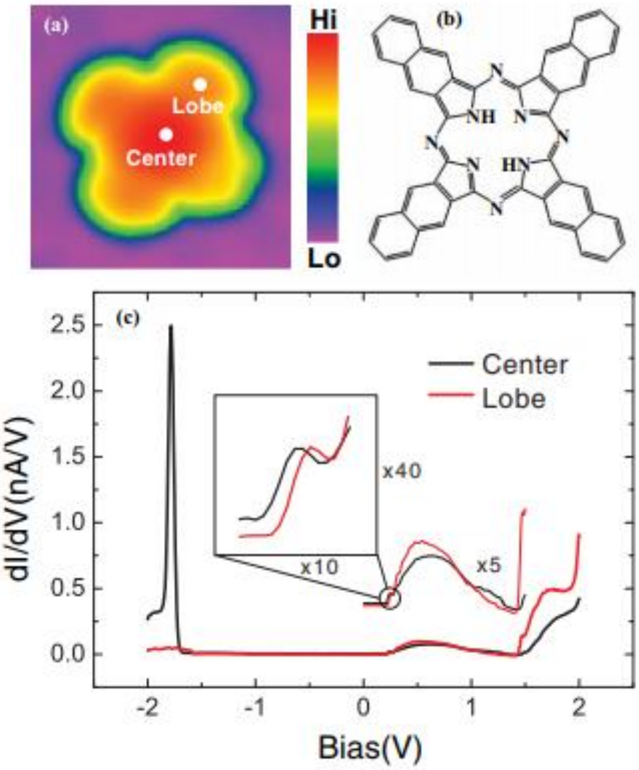

Figure 76: (a): STM image of a naphthalocyanine molecule on an alumina layer on a NiAl(110) substrate obtained in constant current mode with image parameters: 1.3 V and 60 pA. (b) Schematic of the molecule. (c) STS spectra above two locations within the molecule, the centre (black) and lobe (red). [88]

7.5 Future Work

To further extend the work on position dependence of molecular manipulation, a more extensive map of the molecular site and the surrounding region could be undertaken. Adapting the LabVIEW code which positions the tip at these three injection sites could be modified to cover a region over the molecule, to more accurately measure the probability per injected charge of manipulation as a function of position. This would further our understanding of the excitation mechanism of local manipulation.

A second experiment could be to try and quench the manipulation of molecules both locally and non-locally. As documented in [85] the proposed manipulation mechanism is via the population of the 2V surface state with its onset at 1.4 V. If the Si(111)-7x7 surface is dosed with oxygen molecules, this is known to distort the Si(111)-7x7 reconstruction and prevent transport across the surface [89]. Repeating these manipulation investigations with an oxygen dosed surface should prevent the manipulation of any molecule as the tunnelling charge cannot enter the 2 V state and therefore cannot transition from this to cause manipulation. This would strengthen the proposed mechanism for atomic manipulation. Manipulation may instead exhibit a higher voltage threshold corresponding on the onset of a higher lying surface state and as a result, the branching ratio would be measured at a different constant value corresponding to the charge relaxing to the bottom of this new higher lying state.

Chapter 8

Light Emission

As indicated in section 3.3, it is not purely locally that the injected tunnel current can induce manipulation, but also non-locally, at a distance away from the injection site. The indication by Rusimova *et al*. that the non-local effect is dependent on the ability of electrons to tunnel to and transition from high lying silicon surface states to lower states to cause wide spread desorption events has prompted the concept of light detection [43]. From undergraduate physics level, the concept of electrons transitioning from different energy levels and emitting a photon as a result is well known. We therefore test whether there is photon emission to accompany this non-local charge transport process.

This chapter documents the initial work done to detect light emission from the Si(111)-7x7 surface. We show that light is detected from the tunnel junction of the STM when in tunnel contact with the Si(111)-7x7 surface. Investigating the voltage dependence of this light emission reveals a ~2 V threshold matching that of our non-local manipulation work. We propose that both light emission and non-local manipulation have the same origin of charge relaxing to the bottom of a surface state before transitioning between Si(111)-7x7 surface states via two different inelastic decay channels. Transitions between these surface states match the light emission observed in this thesis and are used to re-interpret the results for previously published light emission papers. This work is currently being drafted for submission to ACS Nano.

8.1 Literature Review of STM Light Emission

Light emission (sometimes called STML: Scanning Tunnelling Microscopy Luminescence) has been detected from STM systems with a wide variety of tip materials and substrates, at both room and low temperature. Many different mechanisms by which this light is generated are suggested in the literature. A common suggestion for metallic material tips is the decay of a plasmon. A plasmon is the oscillation of free electrons in a metal, which can couple to resonances between the tip and sample creating localized modes with a sharp STM tip. These are called tip-induced plasmons, inelastically excited by tunnelling charge which decay in the following three different ways. They can couple to surface plasmon polaritons or excite electron-hole pairs in metal, both of which are non-radiative decay routes. Alternatively, the plasmon can couple to light, resulting in photon emission. The details of plasmons and plasmon induced photon emission are more extensively covered in a review article by Kuhnke *et al*. [90].

Downes and Welland investigated the Si(111)-7x7 surface with a tungsten tip for light emission [9]. The substrate was not fully heated and hence contained silicon carbide regions, Si(111)-7x7 and Si(111)-7x7-W regions, the latter two regions the only ones to emit photons. The group discuss the plasmon emission process by an inelastic tunnelling electron exciting a plasmon and hence losing energy ħω. The plasmon is confined below the tip and extends both into the tip and across the tunnel gap to decay exponentially in the sample. It has a gaussian shape laterally which determines the resolution in photon maps and then decays into a photon of equivalent energy, is dampened, or loses its energy via interband transitions [9].

Iwami *et al*. suggest plasmons as the emission mechanism for their silver tip on the Si(111)-7x7 surface at 77 K, following a good match between experiment and theory, as shown in Figure 77a [91]. An emission peak was found at 2.25 eV, invariant to room temperature and sign of injection bias and modelled theoretically by a sphere and plane surface with the associated dielectric and work function of both the tip and sample. Repeating this calculation for a tungsten tip found an emission efficiency reduced by three orders of magnitude, confirming the absence of emission when measured experimentally [91].

Returning to the silver tip and observing atomic resolution whilst looking at emission shows that peak photon intensity coincides with adatom positions. Figure 77b) shows a line scan of the tip height as a function of position (top curve) and the photon intensity as a function of position along the same line scan (bottom curve) [91]. The dashed lines indicate when a peak in the photon intensity corresponds to a peak in the height line scan (an adatom site). Hence, the group conclude that the mechanism for manipulation must be plasmons within the 7x7 reconstruction layer enhancing emission, with the corner hole regions above the bulk silicon showing reduced emission.

Berndt *et al*. measured emission from tungsten (W), silver (Ag) and gold (Au) tips on Ag(111) and Au(110) surfaces [92]. Comparisons between emission spectra of a W or Ag tip on the Ag(111) surface show tungsten resulted in a broad emission peak with a low intensity, compared to a Ag tip with distinct emission peaks, see Figure 78. The differences between these two were attributed to the dielectric properties of the tip materials. Their theoretical model mimicked these structures and from this they concluded that W tips have no plasmon modes within the energy range measured, whereas Ag tips have plasmon resonances within this range and so couple to plasmon modes in the Ag surface when the tip is close to the substrate. This evidence that W tips do not display any plasmon modes detectable at this energy range suggests that other forms of emission mechanisms must be occurring in some systems [92].

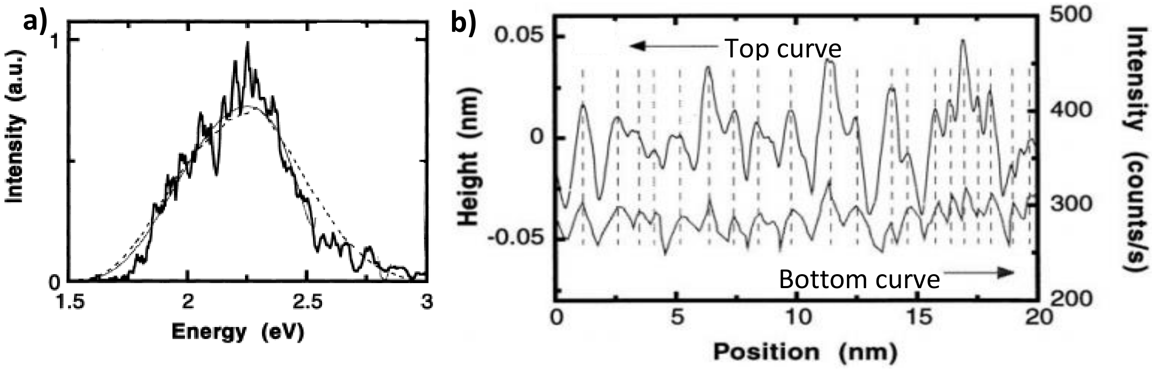

Figure 77: a) Photon energy spectrum measured experimentally at 3 V (thick line) with a broad emission peak at ~2.25 eV matches well with theoretical curve (dashed line) calculated using the dielectric function of the tip and the surface. b) Tip height line scan as a function of position, and photon intensity as a function of position along the same line scan. Dashed lines indicate when the peak intensity corresponds to a peak in the tip height scan at an adatom site. Scan obtained at -2 V and 1 nA. [91]

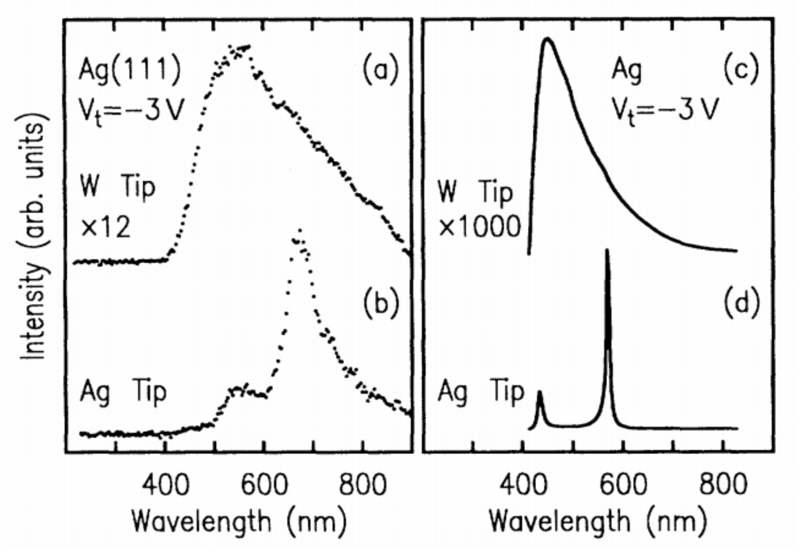

Figure 78: Photon intensity spectrum as a function of wavelength for different tip materials on the Ag(111) surface. (a) and (b) show experimental results for a W and Ag tip respectively at -3 V, and (c) and (d) show the corresponding theoretical model. [92]

Abraham *et al*. have explored emission from GaAs/AlGaAs heterostructures with a W tip [93]. The mechanism from this system is the recombination of injected electrons recombining with holes, resulting in emission. Electrons injected into the conduction band recombine with holes in the valence band and reveal information about band gaps and the layers within the heterostructure from the photon emission energy.

A 'novel mechanism' for emission was reported by Thirstrup *et al*. with charge transitions between tip and sample states [94]. They used a system of Si dangling bonds induced from hydrogen desorption on the Si(001)-3x3-H surface, at room temperature with a tungsten tip. The dangling bonds emitted more photons than hydrogen atoms for both positive and negative bias. They investigated the photon intensity and threshold to emission for a range of voltages and deduced that electron-hole recombination was unlikely from the low quantum efficiency measured. Plasmons were discarded as sources as the photon emission observed was at a different energy range and the W tip did not have any plasmon modes to couple. Optical transitions with the charge transitioning between states in the substrate causing emission were also eliminated. Instead, the suggested mechanism was indirect dipole transitions - when tunnelling electrons transition between tip states and dangling bond states, resulting in photon emission [94].

The work of Imada *et al*. was key in our motivation to investigate photon emission on the silicon surface [10]. They showed that photon emission was possible on the Si(111)-7x7 surface with a molybdenum tip coated in silver to enhance emission (*5,000-50,000* times compared to a tungsten tip) [10]. Mirrors both internal and external to the UHV system were used to focus the light on a photomultiplier tube for mapping, or with a spectrometer and CCD camera. A schematic of emission can be seen in Figure 79, where the tunnelling electrons emit photons (red) enhanced by radiating 'localised surface plasmons' (LSP) [10].

Photon intensity as a function of photon energy for both a sharp and blunt tip, with a tip apex radius *~20 nm* and *~60 nm* respectively, was investigated in Figure 80. The fitting process revealed that each spectrum was made up of the same constituent photon energies, indicating that the photon-emission was sample and not tip dependant. The greater count rates for the blunt tip were claimed to confirm previous theoretical work where larger tip areas result in a higher photon count.

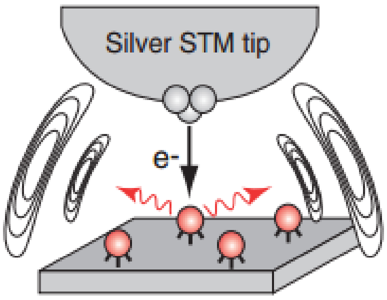

Figure 79: Schematic of the emission process, where electrons tunnel from the STM tip to the sample and emit photons (red arrows), enhanced by radiating LSPs. [10]

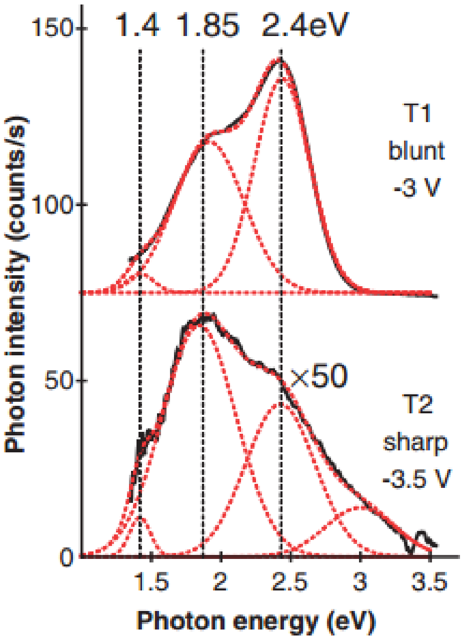

Figure 80: Photon intensity spectra as a function of emitted photon energy for a blunt and sharp tip (60 nm and 20 nm respectively), showing the same constituent emission energies in both cases. [10]

The voltage dependence for this photon emission signal can be seen in Figure 81 [10]. A single peak was observed at *1.4 eV* following a hole injection at *-1.6 V* and a second peak tends to *1.85 eV* for voltage injections between -1.8 V to -2.3 V. A third peak was detected at 2.4 eV for injections between -2.4 V and -3 V. Each of these photon energy peaks were only visible above these voltage thresholds and were stated to match those of other surface sensitive spectroscopy techniques [10].

A similar experiment was repeated for electron injection as seen in Figure 81c), revealing intensity peaks at the same energy values. In both the electron and hole injection experiments, decreasing the injection voltage to more negative values resulted in the peak photon energies remaining at the same energy.

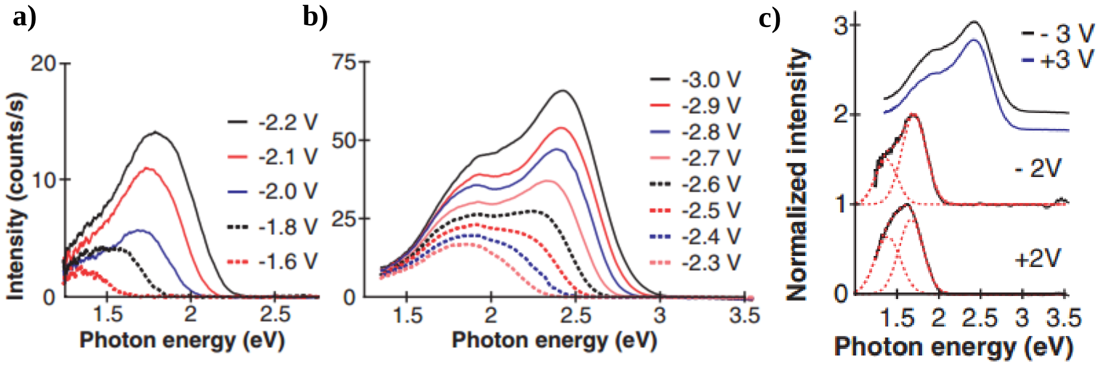

Figure 81: a) and b) show photon intensity as a function of voltage, indicating the onset of peaks at 1.4, 1.85 and 2.4 eV. c) Photon intensity as a function of energy for both electron and hole injection. [10]

Therefore, it was concluded that the mechanism of emission must be different to the previously accepted concept of transitions between the tip and sample states, like that concluded by Thirstrup *et al. [94]*. Instead they deduced the mechanism to be the decay of these LSPs after having been excited by tunnelling electrons [10]. They modelled this theory, but failed to reproduce peaks at the expected energy positions and infer this to be because only bulk silicon was modelled, without the Si(111)-7x7 surface structure. They suggest that an alternative mechanism for photon emission could also involve 'inherent electronic transitions' due to the fixed energy values of the emission peaks and the independence of the tip size [10].

As can be seen from this brief literature review, multiple different mechanisms are suggested for photon emission. Typically, it appears that the decay of a plasmon is a common mechanism on metal systems with a metal tip that supports plasmon modes and can couple to plasmon resonances in the surface. For the Si(111)-7x7 surface, multiple mechanisms have been suggested as the emission source. Given that the use of a tungsten tip cannot support plasmon modes, it seems most probable for emission to occur via charge transitions. Both tip to sample and electronic state transitions within the sample are tentatively suggested.

From this we began investigating whether it would be possible to detect any emission from the Si(111)-7x7 surface with our tungsten tip, using a highly sensitive camera to detect any emitted photons. On this system of a Si(111)-7x7 surface probed with a tungsten tip, our research group has investigated non-local manipulation of toluene molecules, as detailed in section 3.3. The injected charge undergoes an inflation step expanding from the injection site before diffusion occurs and the injected charge can decay to a lower lying surface state. During this transition, molecules on the surface can be manipulated [43]. For this reason we decided to investigate whether light emission was detectable from our system and whether this could occur via the same mechanism of transitions between surface states, as occurring for non-local manipulation.

8.2 Preliminary Investigation

To investigate light emission properties from this Si(111)-7x7 surface, the same room temperature STM 1 system was used and adapted to include an *Andor Luca R* camera attached to the STM chamber - an electron multiplying CCD camera (charge-coupled device). This was fixed directly above the STM head and focussed on the tunnel junction at 80˚ to the surface normal and approximately 20 cm from the tunnel junction, pictured in Figure 82a). *Micro-manager* software allows images to be taken of the tunnel junction, showing the photon counts for each pixel in the image. The *Andor Luca R* camera has

1004 x 1002 active pixels, with each pixel 8 μm x 8 μm. The following sections detail the data taking process and results found from voltage dependence experiments of this photon emission.

To detect emission, preventing excess light from entering the camera was paramount. This was achieved by concealing the camera within a black aluminium foil lined box which was then covered by blackout material. Experiments were only undertaken once the room lights and ion gauge were switched off.

To determine the relevant exposure time for acquiring an image, the camera gain was set to its maximum of 1000 with the STM scanning at 3 V and 1 nA. Camera images were taken at increasing exposure times to determine the maximum time before saturating pixels in the camera, which corresponded to 40 s.

To establish the required gain for adequate amplification of the detected signal, a 40 s exposure with 3 V and 1 nA STM parameters were tested for a variety of different gains from 20 to the camera maximum of 1000. The tunnel junction region was identified by first taking a camera image with the room lights on, at a low exposure time of 150 ms and 2 gain, seen in Figure 82b) where the sample and tip are highlighted in orange and purple respectively (best viewed in colour online). Images could then be acquired with the STM tip scanning (emitting a tunnelling current), and with the STM tip retracted from the surface by 5 nm, hence no tunnelling current. Pairs of these on-off current combinations were taken randomly for the range of gains investigated.

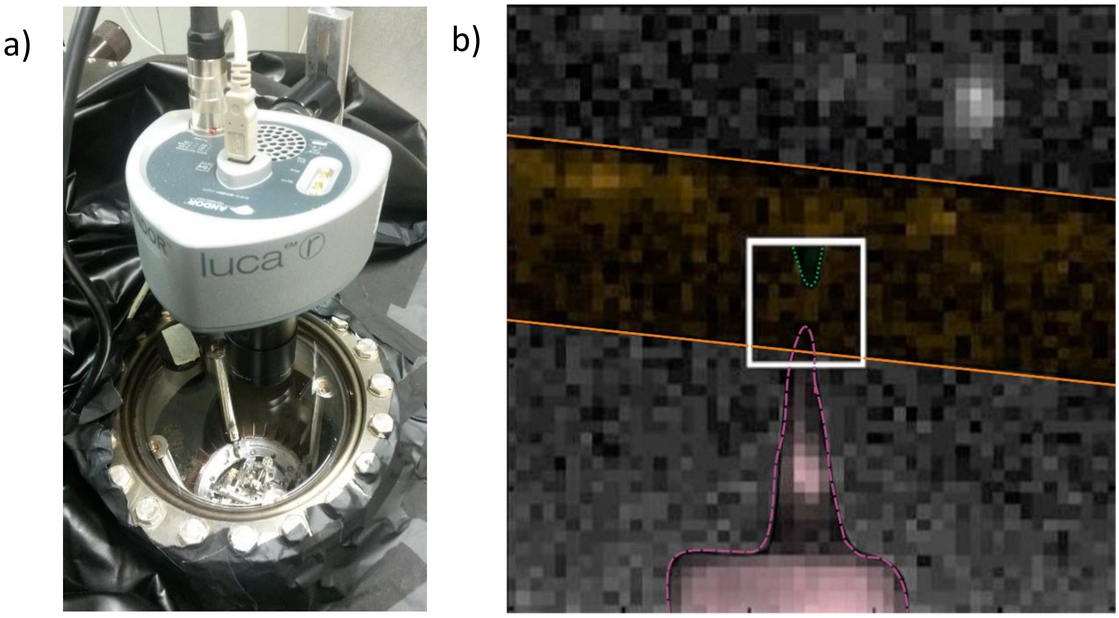

Figure 82: a) Photo of the STM light emission experimental set-up. The Andor Luca R camera is mounted above the STM head and focussed on the tunnel junction. b) Camera image of the tunnel junction, with the sample outlined and shaded orange, the tip outlined and shaded purple and the reflection of the tip in the sample outlined and shaded green (easiest to see in colour online). The white box highlights the region of interest of the tunnel junction for investigating emission.

8.2.1 Data Analysis

Each image obtained is cut to the relevant tunnel junction region, highlighted by the white box in Figure 82b), this includes the tip apex and its reflection in the sample. Each of the 'on' images cropped to this region are shown in Figure 83. The framed image shows the tunnel junction region of the 'lights on' image. Here the bright pixels at the top and bottom of the image correspond to the reflection and apex of the tip respectively.

All the 'on' images and all the 'off' images are summed together before subtracting the total 'off' from the total 'on'. This can be seen in Figure 84 along with the tunnel junction region highlighted in the 'Room lights on' tip image for clarity. A bright pixel with a high count value in the subtraction image indicates that photon emission is occurring. The high count value of this pixel arises when the STM is in tunnelling contact to the sample, and occurs within the tunnel junction region close to the reflection of the tip apex in the sample, an appropriate place to expect emission to be occurring. This is identified as the emission pixel, which is in the same location for all gain values used within this given experiment. This emission pixel is tracked during each image 'on/off' pair and compared to a non-emission pixel located at a distance from the identified emission pixel, plotted in Figure 84e) and f) respectively. There is an obvious increase in the count value for the emission pixel when in tunnelling contact, with an average 'on' count of 1435 ± 98 counts compared to 642 ± 48 counts for the 'off' images. In comparison, the non-emission pixel maintains approximately the same count values for both 'on' and 'off' images, 606 ± 46 and 660 ± 73 counts respectively. The errors calculated here are the standard error of the mean and the fluctuations in value may be due to tunnelling at 1 nA, which can cause the tip to be unstable and change tip state.

To identify the optimum gain for measurements, the mean value of the emission pixel was calculated for each gain and a ratio taken with the mean value of the emission pixel for the 'off' case. This ratio was also repeated for the standard error of the mean for the 'on' and 'off' measurements, both of which are displayed in Figure 85. From this, a gain of 833 gives the highest on-to-off counts for a relatively low standard error ratio and hence this value was chosen as the optimum gain for experiments. All photon experiments now taken use the parameters of 40 s exposure and 833 gain.

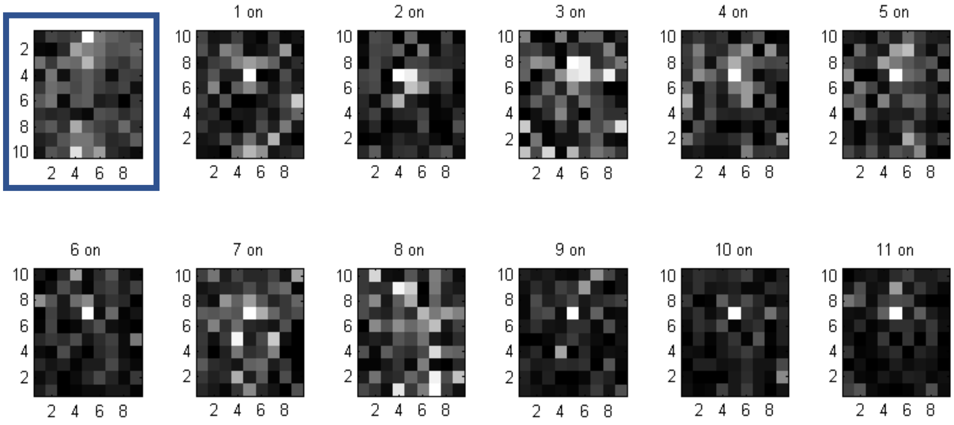

Figure 83: Cropped camera images of the STM tunnel junction region. White pixels indicate a high photon count and dark pixels indicate a low count. Each image labelled '1 on' – '11 on' was obtained with the STM tunnelling at 3 V and 1 nA. The image boxed in blue shows the tunnel junction region of the 'lights on' image, the bright pixels at the top and bottom of the image show the tips reflection and apex respectively.

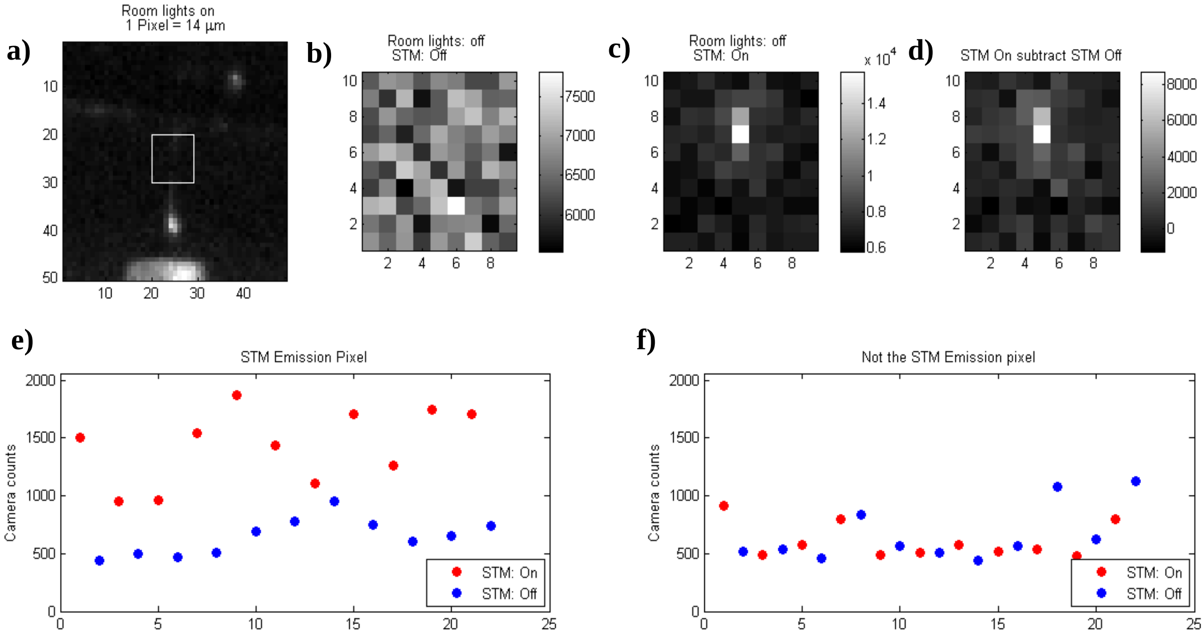

Figure 84: a) A 'lights on' image of the STM tunnel junction with the tunnel junction region highlighted by a white box. The tunnel junction region is shown in b) and c) with the summation of all the 'off' and 'on' images respectively. These are subtracted in d) to reveal an emission pixel with a high number of photon counts (white in colour). This emission pixel is tracked in all the 'on' and 'off' images and its count value is plotted for each image in e), the same is repeated for a non-emission pixel in f). This reveals a high count for the emission pixel during every 'on' image and consistently low counts for the non-emission pixel in all cases.

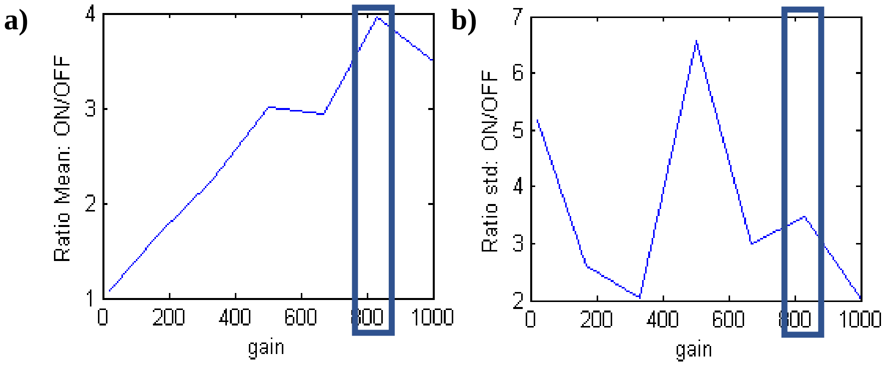

Figure 85: a) The ratio of 'on' divided by 'off' counts for the mean value of the emission pixel as a function of gain. b) Standard error of the mean for the 'on'/'off' ratio as a function of gain. 833, highlighted by the blue box has the highest 'on' count compared to 'off' for the smallest difference in standard error hence this was chosen for the experiment.

8.3 Results – Voltage Dependence

8.3.1 Electrons

Following previous non-local work as summarised in section 3.3, injection voltage appears to play a role in whether manipulation is seen and to what extent. This voltage dependence of light emission was investigated for the Si(111)-7x7 surface by an initial voltage sweep, suggesting a threshold in the region of 1.5 V to 2.0 V above which a large count rate is detected.

A repeat experiment was carried out with a 0.1 V step size between 1.5 to 3.0 V, to identify the position of the threshold. Manually checking the analysis for each voltage indicated that the emission pixel fluctuated between two adjacent pixels. To reliably encompass all this emission count information in further experiments, the MATLAB code was altered to consider all the pixels surrounding the emission pixel identified at 3 V. A schematic of this can be seen in the inset of Figure 86 where the camera count value for the sum of 9 pixels surrounding the emission pixel over the voltage range probed is plotted. This reveals that the threshold to photon emission arises at 1.9 ± 0.3 V from fitting with a linear threshold law as done in [8]. No light emission is detected below this voltage and there is near monotonic increasing emission detected above 1.9 V.

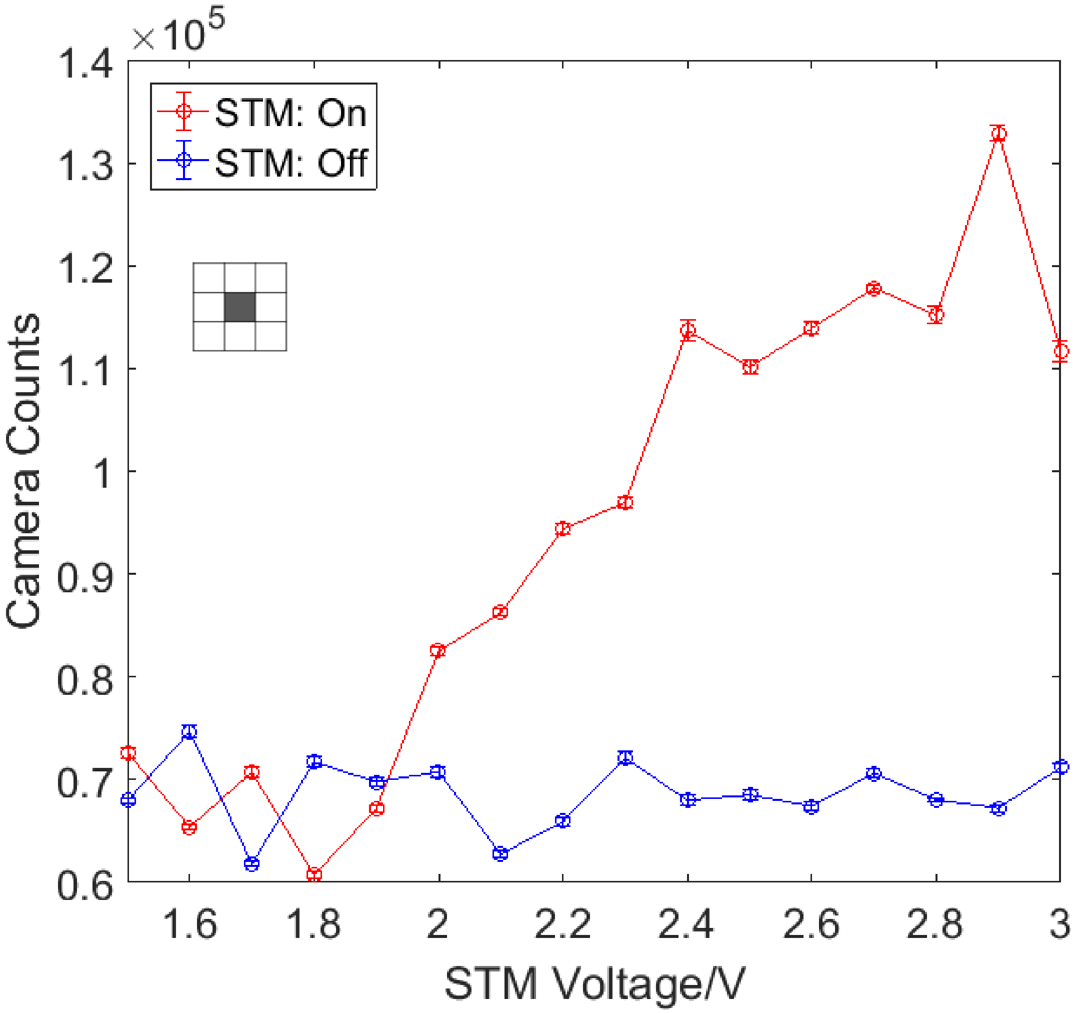

Figure 86: Mean camera counts of the emission pixel and its surrounding pixels, as a function of bias voltage in 0.1 V increments and 1 nA. The emission pixel is identified from the 3 V image and is highlighted in the inset.

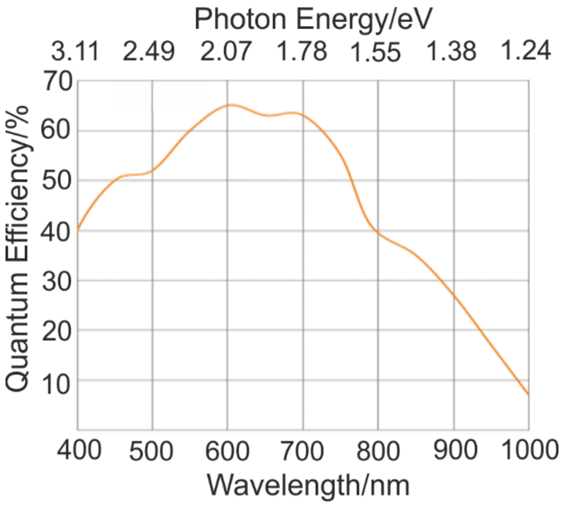

Figure 87: Andor Luca Camera Quantum Efficiency as a function of wavelength and photon energy. This indicates the sensitivity of the camera to detect wavelengths in the range 400 to 1000 nm, adapted from [95].

To confirm that this threshold occurs as a result of something physical within the system imaged and not as an artefact of the camera, the camera quantum efficiency curve can be seen in Figure 87. This corresponds to the sensitivity of the camera for photon detection at different wavelengths. Assuming a tunnelling 1.9 V electron would create a ~1.9 eV photon, the threshold in this data corresponds to a wavelength of ~654 nm. Around 600 – 700 nm the quantum efficiency of the camera is at its highest. Therefore, the distinct rise in the photon intensity corresponding to ~654 nm does not occur because the camera is poor at detecting at wavelengths above 654 nm and good at detecting at wavelengths below this. Instead it is assumed to be for a physical reason within this system.

8.3.2 Holes

The experiment was repeated with negative voltages from -0.5 V to -3.0 V to detect photon emission as a result of hole injection. There was no significant difference between the 'on' and 'off' counts and no light emission was detected. Rusimova *et al*. documented that the non-local measurements were only seen for injection voltages below -1.2 V [43]. Using the same assumptions as 8.3.1 this corresponds to a wavelength of ~1035 nm. At this wavelength the camera quantum efficiency is $<$ 10%, beyond the detection range of the camera and suggests why emission may be undetected in this regime [95].

8.4 Discussion

Our understanding of this observed photon emission threshold for electron injection mimics our proposed mechanism of non-local manipulation for holes, as explained in section 3.3. For electron injection, the threshold to observe non-local manipulation is 2 V, with the STS data and relevant theoretical model parameters shown in Figure 88 [87]. In a similar manner to Figure 17 for non-local manipulation of holes, Figure 88 shows β, the probability of manipuation per injected electron increases monotonicaly above a 2 V threshold, matching that observed in the photon emission. Within this 2 V to 2.8 V voltage range there is a constant diffusion length scale λ, equal to 7 ± 1 nm, and an increasing supression region *R,* shown in Figure 88B and C respectively. Above 3 V, STS data above a

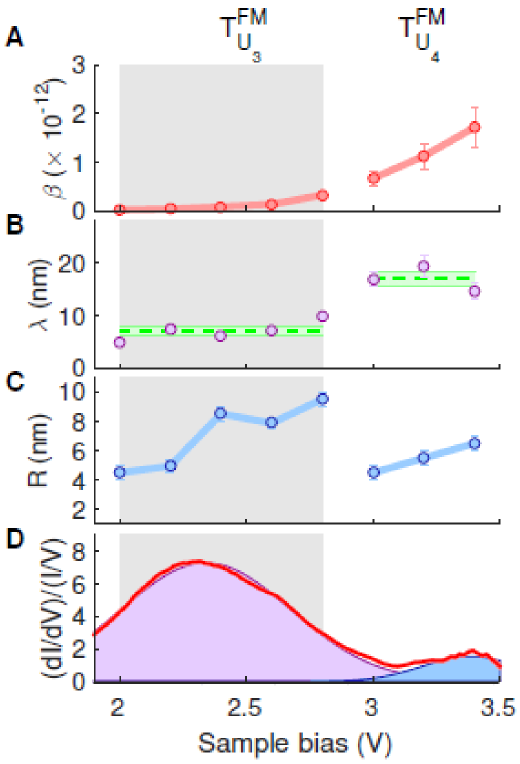

Figure 88: Non-local manipulation model parameters as a function of injection bias. A: Probability per injected electron increases with increasing bias. B: The diffusion length scale is constant between 2 to 2.8 V and step change is seen at 3 V. C: The suppression region displays a saw-tooth trend, increasing with sample bias and resetting at 3 V. D shows STS data obtained above a FM site [87].

FM site in Figure 88D reveals the onset of a new surface state, this corresponds to the voltage at which the supression region resets and a new constant diffusion length scale is measured as 17 ± 2 nm.

In the same way as we propose for hole injection [43], the injected electrons tunnel to a silicon surface state and the wavepacket undergoes an inflation step expanding from the injection site. The electron thermalises to the bottom of the surface state before undergoing 2D diffusion for ~200 fs [96], where it can then inelastically transition out of this state to a lower lying one. During this transition the manipulation of a molecule can occur, at a distance from the injection site [43]. This provides the decay channel of the electrons from the diffusion model.

We propose that it is this transition between states that not only results in manipulation, but also results in the emission of photons, providing two different inelastic decay channels for the injected electrons. No light emission, or molecular manipulation is observed below the ~2 V threshold as it is not possible for electrons to tunnel into the 2 V state at this energy. Above the 2 V threshold, greater numbers of photons are observed as more electrons can enter the 2 V state at these higher voltages. Therefore, more transitions occur and hence greater photon emission counts are seen.

Similar to the schematic in Figure 75, Figure 89 illustrates how we propose that the non-local manipulation mechanism and photon emission mechanism have a common origin. This highlights the ultra-fast relaxation down to the bottom of the U_3 state to 2 V before the charge transitions. Manipulation or photon emission events therefore occur with transitions from and to the same surface states regardless of the initial injection voltage, providing the injection is above the 2 V threshold. When the injection voltage is large enough that the tunnelling charge has access to tunnel to a higher energy surfaces state (3 V in this case for electron injection) the same mechanism occurs with the charge relaxing to the bottom of this new surface state before transitioning.

This corresponds to the two constant values of λ, the diffusion length scale in the non-local model. This shows that once above this 2 V threshold the injected charge is transported in the same way until injections at voltages greater than 3 V, when the charge can tunnel into the next surface state. Transitions from the 2 V or 3 V state would emit photons with two corresponding energies and wavelengths. Imada *et al*. report this in Figure 80 where both a sharp and blunt tip emit photons of the same energy, and each of these energies is visible above a certain voltage threshold in Figure 81 [10].

This proposed mechanism can enable us to view previously published data in a new light, specifically the work by Imada *et al*. detailed in section 8.1 [10]. The voltage dependence for the onset of each new photon energy peak seen in Figure 81, we propose, aligns with the onset of a Si(111)-7x7 surface state and therefore results in a new energy/wavelength of photon emission. STS data taken at each atomic site of the Si(111)-7x7 surface is shown in Figure 90 [97]. Following that Fermi's golden rule for the probability of transitioning between states per unit time is proportional to the density of states of the final state of the transition, the change in energy can be deduced for transitions from the bottom of each surface state to the peak of a lower lying state. Each unfilled surface state is denoted by U_x, and the filled surface states by S_x, as seen in Figure 35. For electron transitions we must consider the U_x states, with the non-local electron induced manipulation threshold occurring at the onset of the U_3 state, as seen in Figure 88.

The bottom of the U_3 and U_4 states are measured as 2.0 ± 0.1 V and 3.0 ± 0.1 V respectively from Figure 88 [87]. From Figure 90, the peak of each state is determined by fitting a gaussian curve beneath each peak in the STS data, in the same way as Figure 88D where a purple and blue gaussian is fitted beneath each STS peak. A table of each possible surface state transition and its energy difference are shown in table 1, each with an associated error calculated from the HWHM (half-width half maximum) of each

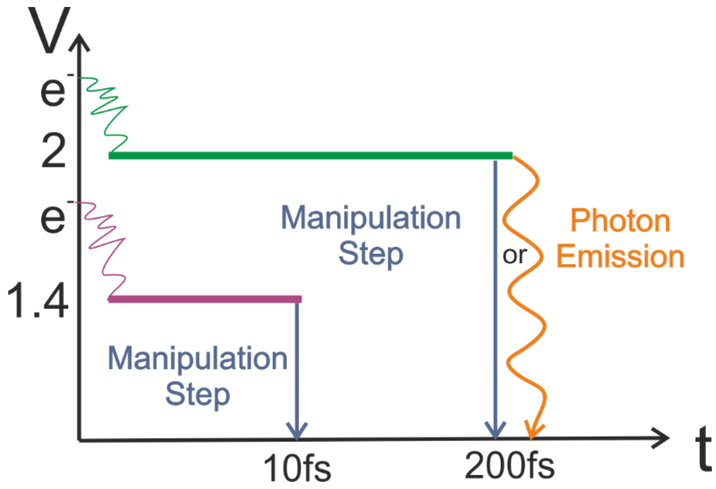

Figure 89: Schematic of voltage as a function of time illustrating the proposed local (purple) and non-local (green) manipulation mechanisms. For non-local, the injected electron undergoes ultrafast relaxation to 2 V before transtioning to a lower lying state to cause manipulation or the emission of a photon via two different inelastic decay channels shown in blue and orange respectively.

STS peak. The values shaded grey are outside the detectable range of the camera, so we are insensitive to any transitions between U_4 to U_3 and between U_3 to U_2. The average change in energy for the transitions U_3 to U_1 shaded in blue is 1.5 ± 0.1 eV, for U_4 to U_2 shaded in yellow is 1.7 ± 0.2 eV and for U_4 to U_1 shaded in green is 2.5 ± 0.1 eV. We assign these to the 1.4 ± 0.3, 1.85 ± 0.9 and 2.4 ± 0.8 eV photon emission energies respectively, from the work of Imada *et al*. [10]. There are no error values given in the paper by Imada *et al.* and hence the errors stated here are from my own estimation of the HWHM for each peak in Figure 80.

The ability to assign the photon emission voltage threshold that we have detected and the photon emission energies published by Imada *et al*. to the transition of charge between surface states of Si(111)-7x7, indicates that the non-local manipulation mechanism and the mechanism by which photons are emitted have a common origin. They both involve the injection of electrons into a surface state (U_3 or higher) where ultra-fast relaxation occurs to the bottom of that specific surface state. Following 2D diffusion, the electron then has two inelastic channels to decay via. One results in the manipulation of toluene molecules, or the other results in the emission of a photon.

Table 1: Energy differences between each surface state transition U_x of the Si(111)-7x7 surface for each atomic site of the unit cell.

	Atomic Site						
Surface State Transition/eV	UM	FM	UC	FC	UR	FR	CH
$U_4 \rightarrow U_3$	0.6 ± 0.5	0.7 ± 0.5	0.7 ± 0.4	0.7 ± 0.3	0.5 ± 0.3	0.1 ± 0.5	0.7 ± 0.3
$U_4 \rightarrow U_2$	1.7 ± 0.3	1.8 ± 0.3	2.0 ± 0.3	2.0 ± 0.5	1.6 ± 0.6	1.1 ± 0.7	1.9 ± 0.6
$U_4 \rightarrow U_1$	2.6 ± 0.4	2.6 ± 0.4	2.5 ± 0.3	2.5 ± 0.2	2.5 ± 0.3	2.6 ± 0.3	2.5 ± 0.2
$U_3 \rightarrow U_2$	0.7 ± 0.3	0.8 ± 0.3	1.0 ± 0.3	1.0 ± 0.5	0.6 ± 0.6	0.1 ± 0.7	0.9 ± 0.6
$U_3 \rightarrow U_1$	1.6 ± 0.4	1.6 ± 0.4	1.5 ± 0.3	1.5 ± 0.2	1.5 ± 0.4	1.6 ± 0.3	1.5 ±0.2

8.5 Future Work

This light emission has so far only been visible with one STM tip, across multiple days of experimentation. Five new STM tips have been investigated for light emission since, however none have proved successful in detecting emission. Possible reasons for this could be changes to: the camera, the external experimental setup or the tunnel junction.

The camera is borrowed from another research group, so internal settings to the camera may be different between experiments. Contact with the *Andor Luca* camera provider company suggests this is not possible. Therefore, the camera must still detect light in the same way.

The external experimental set-up aims to prevent excess light from entering the STM chamber using a black foil lined box and blackout fabric. This is rebuilt around the STM chamber prior to each experiment, however the background count level is consistent between experiments and therefore suggests that the camera count value when in tunnelling contact is not being masked by a higher background count value from any excess light in the system.

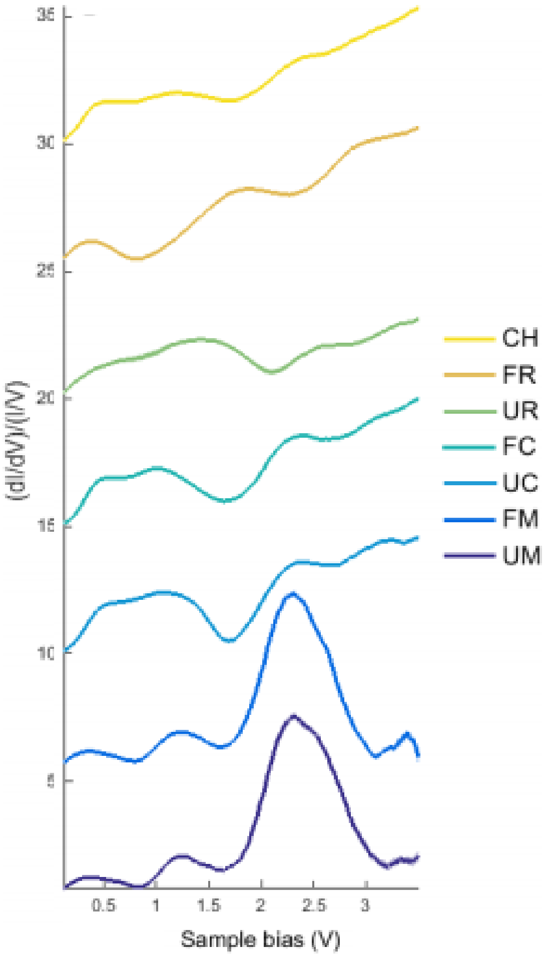

Figure 90: STS spectra obtained with positive bias at each atomic site of the Si(111)-7x7 unit cell [97]. (see Figure 34 for schematic of atomic sites and the corresponding abbreviations).

The investigation with new tips has obviously changed the tunnel junction. It could be that the macroscopic shape of the tip is affecting the optimum focus on the tunnel junction. The macro structure of the tip apex can exhibit angular and jagged edges if vibrations are experienced during the etching process. In some cases, a hook or recoil has even been observed at the apex. This results in a tip far from the ideal equal height and base aspect ratio, as discussed in section 4.6.1. The focus of the camera is adjusted before each experiment, judged by eye via a live 'lights on' image at low gain and exposure time. If the apex is slightly out of focus, the light emitted would be blurred across the detection area, giving a lower photon count spread over more pixels. This could be detrimental to determining the emission pixel in the 'on' images as counts were typically only double the 'off' counts.

Further investigation with new STM tips would be required to regain the detection of emission. SEM (scanning electron microscope) images of each tip following experimentation would allow insight into the macroscopic structure of tips that were ineffective at generating photon emission.

Once light detection is re-obtained, further work for this region of investigation could include looking into the current dependence on photon emission for electrons. Increasing the current would result in more tunnelling electrons and therefore should show a linear increase in the number of photons emitted.

Steps to automate the acquisition of data have been taken, but further work to complete the data analysis is needed. This automation offers the ability to take an image while the STM is paused and hence developing this to acquire images over silicon adatoms at specific sites in the Si(111)-7x7 unit cell would be a natural progression. This would allow comparisons between photon emission from different adatom sites in the unit cell, as suggested by the photon maps produced by Imada *et al*. where corner adatom sites reportedly have a higher emission intensity [10].

Another possibility for further work involves the inclusion of gratings or filters to enable the wavelength of the emitted photons to be detected. Initially this could involve repeating the electron emission data described in this chapter with a 654 nm filter. This would filter out this wavelength of light and strengthen the emission mechanism proposed in this chapter.

Finally, in the future, tuneable nano-sources of light may be possible by quenching or inducing states with adsorbates [89, 98, 99] to alter the states between which the injected charge transitions and hence change the wavelength of the light emitted.

Chapter 9

Graphite

Work done so far in this thesis has investigated the local manipulation mechanism and further investigated the non-local manipulation mechanism via the emission of photons. The understanding garnered in this process led to the investigating of whether these techniques could be achieved on a new substrate and molecule system, namely graphene and graphite. This chapter documents the initial ground work undertaken to achieve a reliable substrate/molecule system on which to investigate this.

9.1 Literature Review

Graphene and graphite surfaces have proved a popular material for research, with an abundance of information known about their physical and electronic structure [100]. Non-local transport work has previously been reported on epitaxial graphene, a graphene layer formed from a silicon carbide substrate [101]. Injecting charge into the graphene results in a modification to the buffer layer up to 10 nm away from the injection site, seen in Figure 91, with a schematic of the process in Figure 91(c). When injecting directly into the buffer layer, modifications are only seen up to 2 nm away and hence the graphene layer must be playing a role in the transport of injected charge before the modification event occurs.

To investigate manipulation of molecules on this surface, a suitable molecule must be found that bonds to the graphene surface. Hornett *et al.*, have investigated the effects of oxygen adsorption on the electrical properties of exfoliated graphene on a Si/SiO_2 substrate [102].

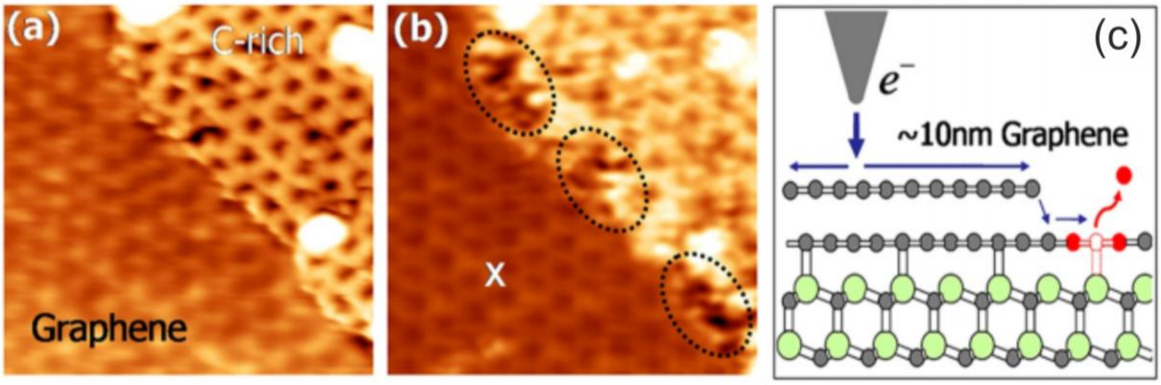

Figure 91: Non-local transport of graphene. (a) STM image of epitaxial graphene, the graphene and carbon buffer layer regions are indicated. (b) Voltage pulse injection at position 'x' results in modifications to the buffer layer up to 10 nm away from the injection site indicated by the dashed circles. Imaging parameters: -1.6 V and 0.1 nA, 20 nm x 20 nm. Voltage pulse: -4 V, 0.1 nA, 50 ms. (c) Schematic of the electron transport (blue arrow) across the graphene and modifying the buffer layer at a distance from the injection site. [101]

The sample was dosed by exposure to an atmosphere of oxygen before measurements were taken in ultra-high vacuum at room temperature. Correlated laser pulses were used to detect time delays allowing changes in the electrical conductivity of the graphene due to the presence of this adsorbed oxygen to be measured. This also provided information on the timescales involved with desorption events, revealing a scale of ~100 fs for oxygen desorption [102].

The conclusion from this paper, that the hot electrons from the laser pulses were the mechanism by which oxygen desorption was occurring, prompted the graphene/oxygen system to be considered for non-local experiments. The STM tip can also be considered as a source of hot electrons injected into the sample and hence manipulation events should be obtainable.

Further work by Hossain *et al*. was also carried out with atomic oxygen on epitaxial graphene [103]. Atomic oxygen was obtained by cracking O_2 molecules using a tungsten filament at 1500^oC, whilst maintaining the sample at 0^oC [103]. When imaged, a dosed sample displayed bright spots where atomic oxygen had bonded, with larger doses resulting in more frequent spots rather than the formation of larger clusters and islands of oxygen [103]. Figure 92 shows clean epitaxial graphene in a), and oxygen doses of 600 L and 2400 L in b) and c) respectively, followed by a 3D image of oxygen atoms on the surface in d). Each image was taken at 2.4 V and 50 pA [103]. Spectroscopy techniques such as XPS (X-ray photoelectron spectroscopy) were used within the chamber to verify the presence of oxygen.

Once dosed, it was found that heating the sample to 260^oC removed the oxygen from the surface and regenerated pristine graphene which was capable of being re-dosed, as seen in Figure 93b [103]. Further experiments found that high voltage scanning of +4 V and 1 nA with the STM tip caused desorptions of the oxygen within the scan area, seen in Figure 93c [103]. This provides further evidence that a graphene/atomic oxygen system should be ideal for tunnel current induced manipulations with the STM tip.

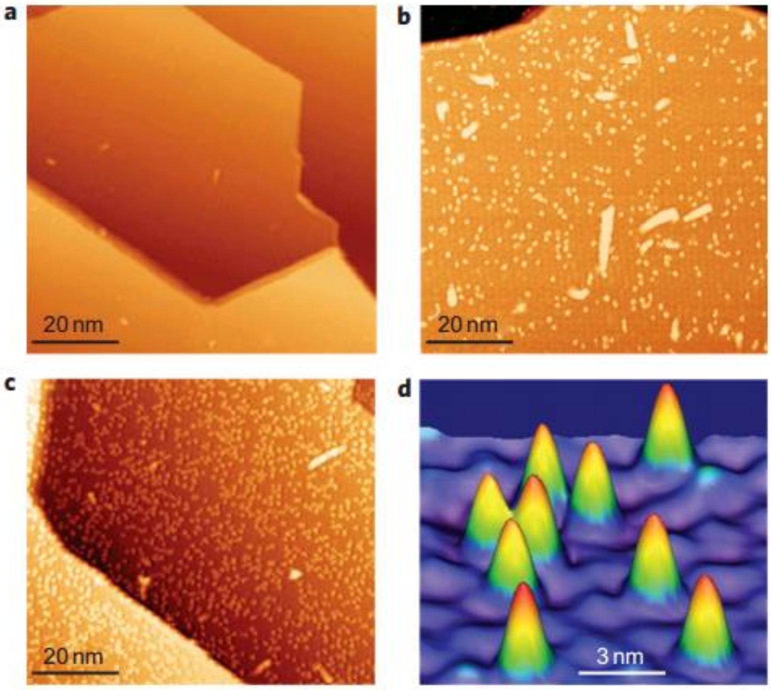

Figure 92: STM images of graphene and oxygen. a) Clean image of epitaxial graphene, b) and c) show the surface dosed with 600 and 2400 L of atomic oxygen respectively. d) A 3D image of oxygen atoms on the graphene surface. Image parameters: 2.4 V and 50 pA. [103]

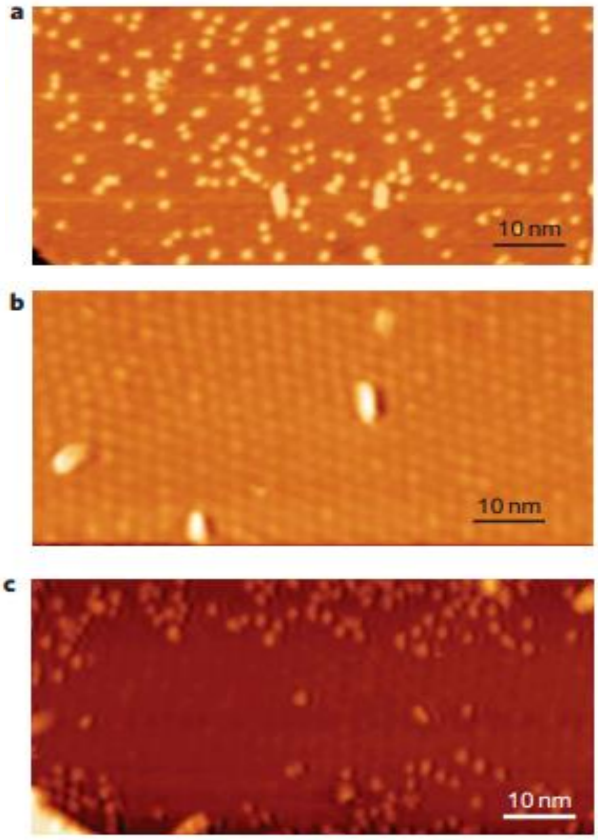

Figure 93: a) Epitaxial graphene dosed with atomic oxygen. b) Dosed substrate heated to 260˚C to remove oxygen atoms. c) Scanning at +4 V and 1 nA has removed oxygen within the scanned region. [103]

Considering the ability to bond to surface adsorbates, graphene and graphite have no dangling bonds on their surface unlike silicon, making the later highly reactive to adsorption. To encourage bonding, high energy atomic radicals would be required, hence the cracking of O_2 molecules to form O atoms, as bonding slightly distorts the carbon lattice into sp$_3$ which is energetically unfavourable [104]. Following various DFT calculations and models it has been shown that the oxygen atoms bind to the surface across a C-C bridge and extends the C-C bond slightly from 1.42 Å to 1.5 Å, as can be seen in Figure 94 [105].

9.2 Preliminary Results

9.2.1 Substrate Imaging

After extensive study and attempts of creating graphene samples via wet transfer techniques, monolayer graphene was transferred onto our Si/SiO$_2$ wafers decorated with hexagonal boron nitride (hBN) flakes commercially. The presence of the hBN reduces charge puddles on the surface as it is inert and atomically flat [106]. Despite this, the samples still proved incredibly difficult to image at room temperature. Atomic resolution was achieved in Figure 95, however for manipulation, large scale graphene areas are required. Example large scale images are shown in Figure 96, however many defects, charge puddles and ripples are present.

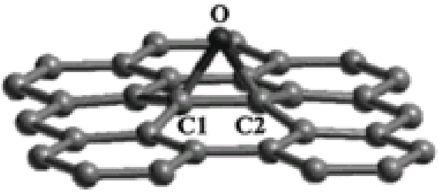

Figure 94: DFT modelling of an oxygen atom shows that bonding occurs over a C-C bridge and extends the C-C bond from 1.42 Å to 1.5 Å [105].

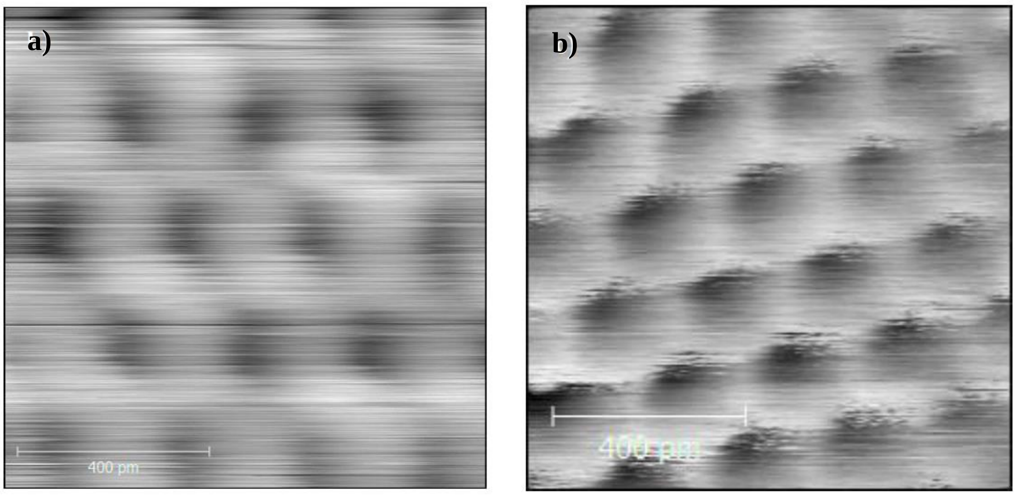

Figure 95: Example STM images of graphene with atomic resolution. Imaging parameters: a) 194 mV and 21 pA, b) 400 mV and 906 pA.

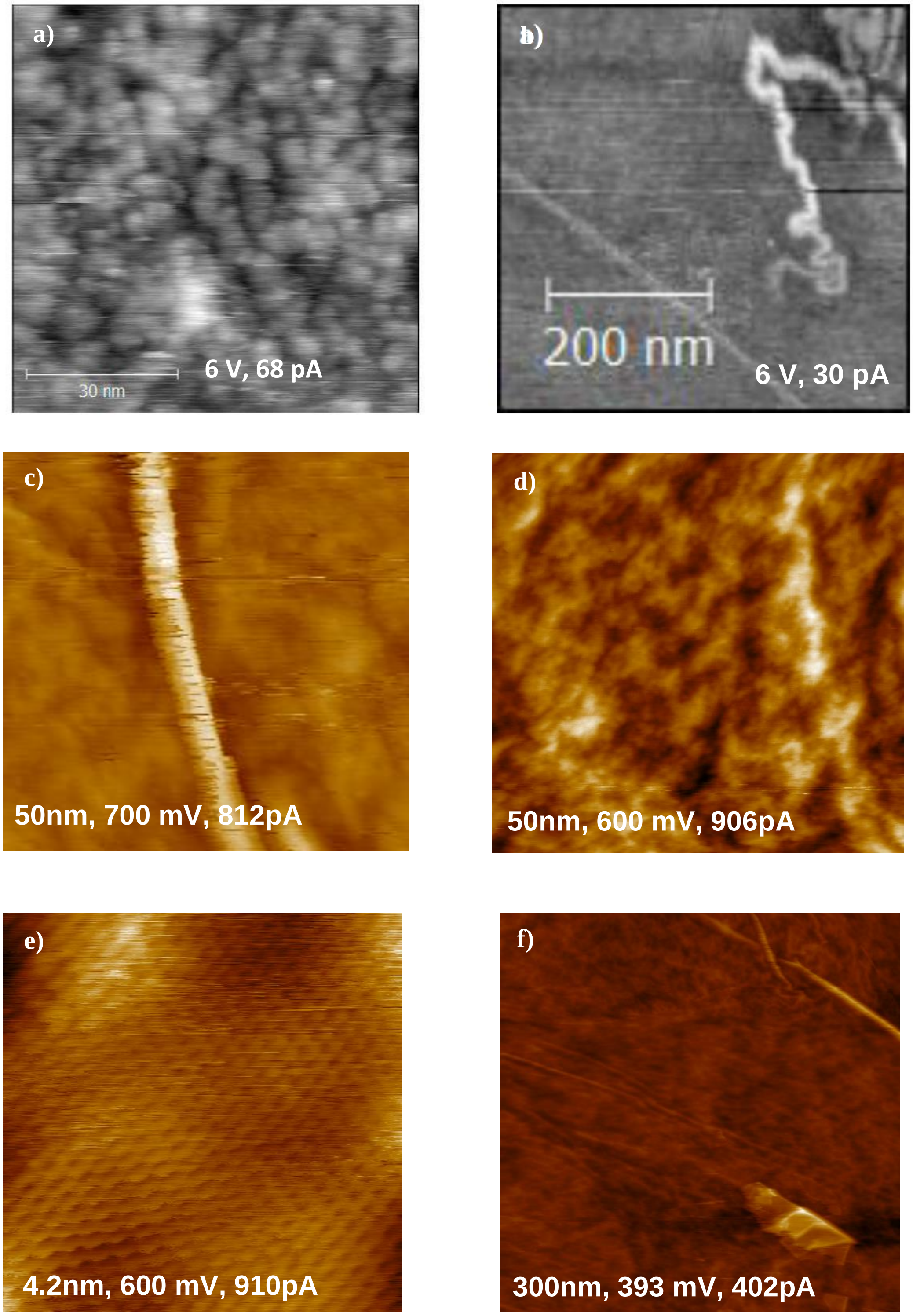

Figure 96: STM images of graphene at a larger scale. The imaging parameters are labelled for each image.

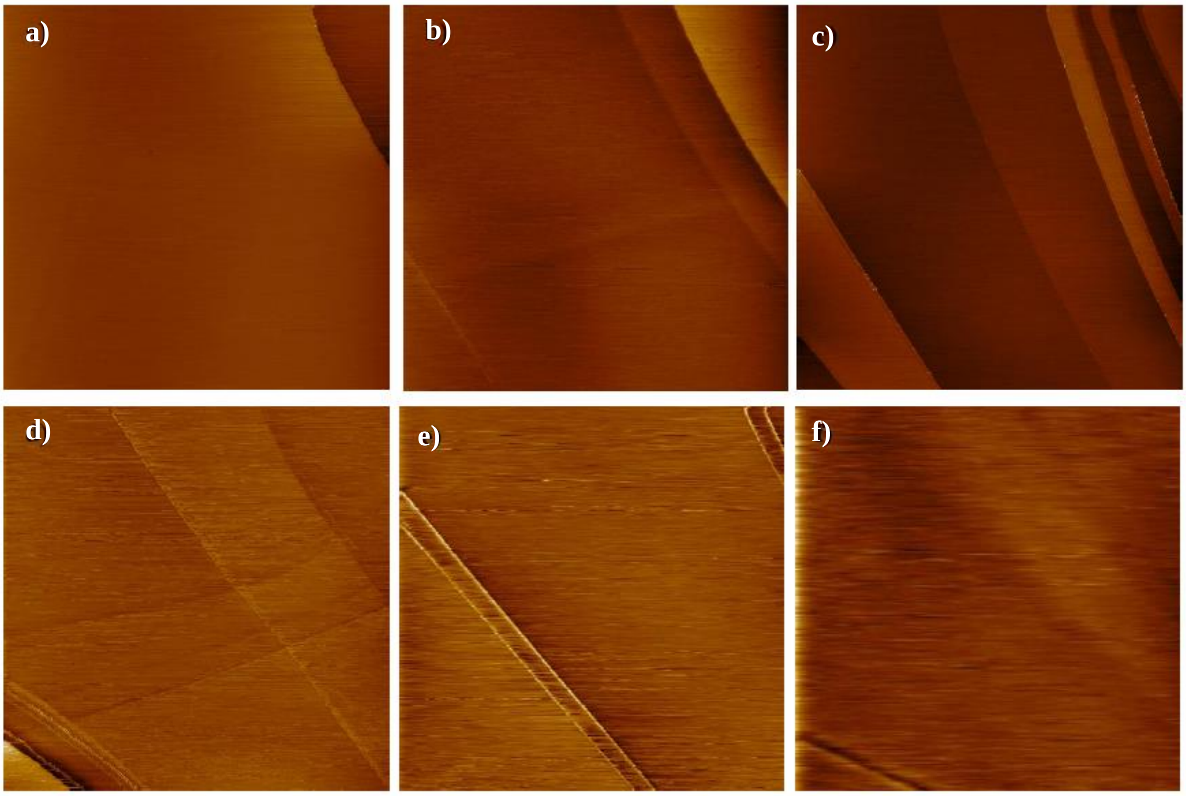

Figure 97: Large scale STM images of graphite at 1 μm size. The surface displays steps typically ~1 nm in height, but between are large flat areas of the surface suitable for use as a substrate for atomic manipulation. Imaging parameters: 1 V and 50 pA.

Imaging of a graphite sample then followed, as this substrate is less dependent on being a continuous sheet, due to the carbon layer beneath also being a conductor. This substrate also eliminates the charge puddle issues experienced when imaging graphene. The sample was cleaned by exfoliation before being mounted and placed into the UHV system. Imaging produced large, flat, defect free areas ideal for dosing with a molecule to manipulate. Images of graphite can be seen in Figure 96, each is 1 μm in size; the surface has steps typically of ~1 nm height but the large flat areas can be seen between.

9.2.2 Dosing Technique

As a substrate can now be reliably imaged, atoms to manipulate are required. An oxygen gas cannister attached to the chamber allows oxygen to be dosed into the prep chamber via LV2 in Figure 18, and again the mass spectrometer was used to verify the presence of pure oxygen within the chamber during this process. Extensive experimentation using the same methods documented by each group in the literature review section 9.1 were used to attempt the dosing of oxygen atoms on the surface, but each proved unsuccessful. Building on the tungsten filament technique of Hossain *et al*. [103], oxygen was successfully dosed using an electron gun. This involves a tungsten filament and a collecting rod of tungsten wire held at 500 V, shown schematically in Figure 98. This creates a strong electric field between the filament and the rod, accelerating electrons (emitted via thermionic emission by passing current through the filament) towards the collecting rod. Ideally these collide with an oxygen molecule and crack it. By connecting in series with an ammeter, the current flowing between the filament and the collecting rod can be measured.

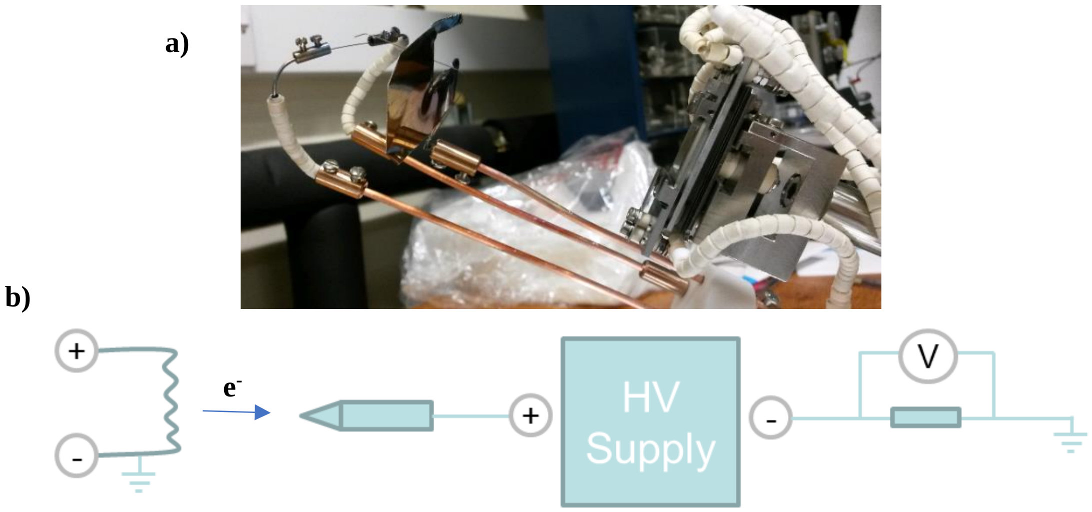

Figure 98: a) Photograph of the electron beam gun setup used for cracking atomic oxygen. b) Schematic of the electron beam gun. Electrons are emitted via thermionic emission by passing a current through a tungsten filament. A tungsten collecting rod held at 500 V accelerates the electrons towards it cracking any oxygen molecule it interacts with during this process. An ammeter in series allows the emitted current to be measured.

The graphite substrate is exposed to an oxygen dose at 5x10^{-8} mbar, whilst the filament is emitting electrons. Bright structures are imaged on the surface after this exposure, analogous to those in Figure 93, which we propose is atomic oxygen. Further evidence for this oxygen atom dosing is seen in Figure 99, where the number of bright spots increases as the exposure time to the filament increases.

To make this system more reliable a LabVIEW program was used to maintain a constant emission current flowing between the filament and the rod, aiming to provide a constant source of oxygen during a dose. A decrease in the detected emission current means an increased current is sent to the filament causing more electrons to be thermionically emitted.

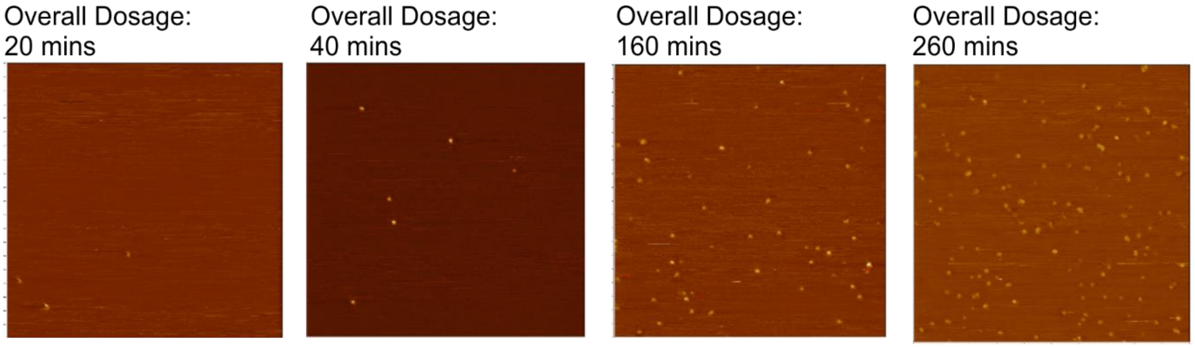
Overall Dosage: 20 mins

Overall Dosage: 40 mins

Overall Dosage: 160 mins

Overall Dosage: 260 mins

Figure 99: Time-line of STM images of graphite following increased exposure time to the electron beam gun for dosing atomic oxygen. The number of bright atomic oxygen spots increases with longer exposure. Imaging parameters: 1 V and 50 pA, 1μm x 1μm.

We believe the work documented here has resulted in a reliable method for dosing atomic oxygen on the surface. However, unlike the work by Hossain *et al*. [103], there are no XPS or other spectroscopic techniques within the chamber to verify the presence of oxygen on the surface.

9.3 Future Work

Initial scans at high voltage (4 V) were unable to manipulate the molecules as described by the Hossain group [103]. Heating also proved unsuccessful as a method for regenerating a clean graphite surface. Even with the removal of the sample into atmosphere and then re-imaging, the bright spots still remained. Only exfoliation was successful in re-creating a clean graphite surface. This and the difficulties in imaging meant this work was halted here.

Multiple avenues of investigation could further progress the research in this topic. Firstly, as the oxygen atoms seem very stable, it may be possible for the dosed sample to be removed and imaged with other SPM (scanning probe microscopy) techniques such as AFM (atomic force microscopy), to obtain further information about the diameter and height of these bright protrusions for further confirmation of their oxygen species.

Secondly STS spectra above both a carbon of the bare graphite surface and above the bright protrusion of an oxygen atom would be interesting comparisons to determine any differences in signatures. Attempts at this were begun on a qPlus LT STM however the 8 MHz noise and *z* drift of the tip hampered our progress.

Further investigation into manipulation could follow, with a more extensive experiment by increasing scanning voltages and current to determine optimum scanning parameters for removing the oxygen from the surface. Once these are known, the possibility of local and non-local manipulation on graphite could be explored with dosed atomic oxygen. Similar analysis to that undertaken in this thesis and the work by Rusimova *et al.* [43] could be used to see if the same mechanism may be occurring but with different voltage thresholds corresponding to states within this oxygen-graphite system.

Chapter 10

Summary

The aim of this PhD was to further understand the mechanisms involved in tunnel current induced atomic manipulation. On the local scale, the work presented here reveals the quenching of the excited state lifetime of a toluene molecule on the Si(111)-7x7 surface. Current injections into these toluene molecules reveals the rate of manipulation linearly depends on the tunnel current for both electrons and holes. This implies a one electron process from the $k \propto I^n$ relationship explained in section 6.1 and as seen in literature [5, 6]. For higher current hole injections (above 10 pA), a plateau is seen in the rate, suggesting a current invariant manipulation process. Thermal, electric field and mechanically induced manipulation methods are each ruled out as possible causes for this plateau.

Observing the data in terms of the probability of manipulation per injected charge reveals a decreasing probability as the tip approaches closer to the surface, for hole injection. Published work confirms a roughly linear relationship between a greater probability of desorption and a longer excited state lifetime of the molecule, with a measured life time of 10 fs [78]. Linearly mapping this lifetime to our maximum measured probability for hole injection reveals that the lifetime of the excited state of the toluene molecule is reduced by over two orders of magnitude (to less than 0.1 fs). Another research group have documented the creation of an interface state on a similar molecule adsorbed on the silicon surface as the tip approaches above the adsorbate [81]. We propose that this tip dependent state offers a new decay channel for the excited state of the toluene molecule in our system.

Using Fermi's golden rule analysis with a proposed decay rate consisting of two contributions (a sample and a tip dependent rate), the probability of manipulation can be considered to have the form $P_e = \frac{\beta\tau_s}{1+exp(-2\kappa m(z-z_0))}$. This shows that at large tip heights the probability is dominated by the 10 fs lifetime in a sample limited regime. For smaller tip heights, the probability decreases in a tip dependent regime due to the new decay channel of the interface state quenching the lifetime of the excited state before its naturally elapsed time.

Returning to the rate of manipulation equation: $k = \frac{P_e I}{e}$, the probability simplifies to a $1/I^m$ dependence at close distances to the molecule, showing the rate of manipulation plateaus with a $I^{(-0.1\pm0.1)}$ dependence. We believe the presence of the tip is quenching the excited state, at this close tip proximity via the creation of an interface state offering a new decay channel for the excited state, reducing its natural lifetime.

The ability to influence the manipulation process via the proximity of the tip to the surface prompted work on measuring the outcome of manipulation, to see if this can also be influenced. The voltage dependence of the branching ratio was investigated with a new stopping injection program to halt the injection of electrons after the first manipulation event occurred. This prevents any further manipulation events that may occur when using a fixed injection time.

The branching ratio is measured to be constant, 0.27 ± 0.02 across all voltages probed and for the associated change in tip height and electric field. Position dependence also reveals a constant branching ratio of 0.18 ± 0.02. This suggests: a) that a 1.4 V threshold exists for local manipulation and b) the final state of manipulation must be common to all voltages and manipulation outcomes. As for the non-local mechanism published in [43], the injection of charge in the local regime is also proposed to undergo a rapid relaxation before reaching the 1.4 V state. Here it can undergo manipulation events when the charge inelastically transitions to a lower lying state. Therefore, each injected charge induces manipulation at the same energy and hence the same ratio of outcomes is seen.

The non-local regime of manipulation has also been explored by investigating photon emission from the Si(111)-7x7 surface, expanding on previous work done within our research group to understand the mechanism involved [43]. The same ~2 V threshold was observed for photon emission as seen in the electron induced non-local manipulation [87]. We propose that this suggests an alternative method for photon emission to those proposed in literature. The non-local manipulation process involves the injected charge relaxing to the bottom of the U_3 silicon surface state to 2 V before it transitions to a lower lying dangling bond state, during which the manipulation of molecules occurs. We propose that the presence of a common voltage threshold suggests that these manipulation and emission processes have a common origin, relaxing to 2 V, where transitions can then occur via two inelastic decay channels. One results in manipulation and the other, the emission of photons.

Photon emission documented in the literature by Imada *et al*., shows that the emission detected from Si(111)-7x7 has three distinct energies at 1.4, 1.85 and 2.4 eV [10]. We propose that each of these corresponds to the onset of a new silicon surface state, which we assign following the analysis of STS data taken on our Si(111)-7x7 surface.

Finally, ground-work was undertaken to begin investigating these local and non-local manipulation processes on a new system. Graphene and graphite samples were imaged and an electron beam gun was successfully used to dose atomic oxygen on a graphite surface. This was reliably imaged as bright spots on the surface.

The work documented in this thesis demonstrates the ability of the STM to not only manipulate molecules, but to access fundamental information of quantum systems and influence them. It has also been demonstrated that the STM system can be utilised to detect photon emission and extract more information about the systems studied.

References

---

[1] Binnig G, Rohrer H, Gerber C and Weibel E, 1982, *Phys. Rev. Lett*, **49**, 57-61

[2] Feynman, R P, 1960, *"There's Plenty of Room at the Bottom", Engineering and Science*, **23**, 22-36

[3] Eigler D M and Schweizer E K, *Nature*, 1990, **344**, 524-526

[4] IBM website, http://www.research.ibm.com/articles/madewithatoms.shtml, [online - accessed 17/05/18]

[5] Stipe B C, Rezaei M A, Ho W, Gao S, Persson M, and Lundqvist B I, 1997, *Phys. Rev. Lett.,* **78**, 4410-4413

[6] Sloan P A and Palmer R E, 2005, *Nature*, **434**, 367-371

[7] Ladenthin J N, Grill L, Gawinkowski S, Liu S and Waluk J, 2015, *ACS Nano*, **9**, 7287-7295

[8] Lastapis M, Martin M, Riedel D, Hellner L, Comtet G and Dujardin G, 2005, *Science*, **308**, 1000-1003

[9] Downes A and Welland M E, 1998, *Phys. Rev. Lett*, **81**, 1857-1860

[10] Imada H, Ohta M and Yamamoto N, 2010, *Appl. Phys. Express,* **3**, 04570

[11] Lafferentz L., Ample F, Yu H, Hecht S, Joachim C, and Grill L., 2009, *Science,* **323**, 1193–1197

[12] Wang S, Wang W, and Lin N, 2011, *Phys. Rev. Lett*, **106**, 206803

[13] Mauerer M, Shumay I L, Berthold W and Höfer U, 2006, *Phys. Rev. B,* **73**, 245305

[14] Palmer R E and Rous P J, 1992, *Rev. Mod. Phys*., **64**, 383

[15] Rae A I M, *"Quantum Mechanics"*, IOP Publishing Ltd, 2002, 4th ed

[16] Chen C J, *"Introduction to Scanning Tunnelling Microscopy"*, Oxford University Press, 1993

[17] Hla S-W, Braun K-F, and Rieder K-H, 2003, *Phys. Rev. B*, **67**, 201402

[18] Zeppenfeld P, Lutz C P, and Eigler D M, 1992, *Ultramicroscopy*, **42-44**, 128-133

[19] Briner B G, Doering M, Rust H-P, and Bradshaw A M, 1997, *Phys. Rev. Lett*, **78**, 1516-1519

[20] Crommie M F, Lutz C P and Eigler D M, 1993, *Science,* **262**, 218-220

[21] Bartels L, Meyer G and Rieder K-H, 1997, *Phys. Rev. Lett,* **79**, 697

[22] Bartels L, Meyer G and Rieder K-H, 1997, *Appl. Phys. Letts,* **71**, 213-215

[23] Dujardin G, Mayne A, Robert O, Rose F, Joachim C, and Tang H, 1998. *Phys. Rev. Lett*, **80**, 3085-3088

[24] Gross L, Moll N, Mohn F, Curioni A, Meyer G, Hanke F, and Persson M, 2011, *Phys. Rev. Lett*, **107**, 086101

[25] Cheng Z, Du S, Guo W, Gao L, Deng Z, Jiang N, Guo H, Tang J, and Gao H-J, 2011, *Nano Res.,* **4,** 523–530

[26] Sugimoto Y, Yi I, Morita K, Abe M, and Morita S, 2010, *Appl. Phys. Lett.*, **96**, 263114

[27] Sweetman A, Jarvis S, Danza R, Bamidele J, Kantorovich L, and Moriarty P, 2011, *Phys. Rev. B,* **84**, 085426

[28] Sweetman A and Stannard A, 2014, *Beilstein J. Nanotechnol.*, **5**, 386–393

[29] Pub Chem, Open Chemistry Database website, https://pubchem.ncbi.nlm.nih.gov/compound/123025#section=Top [online – accessed 11/09/18]

[30] Whitman L J, Stroscio J A, Dragoset R A and Celotta R J, 1991, *Science*, **251**, 1206-1210

[31] Stroscio J A and Eigler D M, 1991, *Science*, **254**, 1319-1326

[32] Ohara M, Kim Y and Kawai M, 2008, *Phys, Rev. B,* **78**, 201405

[33] Lyo I W and Avouris P, 1991, *Science*, *253*, 173–176

[34] Mamin H J, Guethner P H, and Rugar D, 1990, *Phys. Rev. Lett*, **65**, 2418-2421

[35] Morgenstern K, Lorente N, and Rieder K-H, 2013, *Phys. Status Solidi B*, **250**, 1671–1751

[36] Stipe B C, Rezaei M A and Ho W, 1997, *Phys. Rev. Lett,* **79,** 4397-4400

[37] Sagisaka K, Luce A and Fujita D, 2010, *Nanotechnology*, **21**, 045707

[38] Kim Y, Komeda T, and Kawai M, 2002, *Phys. Rev. Lett,* **89**, 126104

[39] Simic-Milosevic V, Mehlhorn M, Rieder K-H, Meyer J, and Morgenstern K, 2007, *Phys. Rev. Lett*, **98**, 116102

[40] Maksymovych P, Dougherty D B, Zhu, X-Y and Yates Jr J T, 2007, *Phys. Rev. Lett*, **99**, 016101

[41] Nouchi R, Masunari K, Ohta T, Kubozono Y, and Iwasa Y, 2006, *Phys. Rev. Lett,* **97**, 196101

[42] Sloan P A, Sakulsermsuk S and Palmer R E, 2010, *Phys. Rev. Lett*, **105**, 048301

[43] Rusimova K R, Bannister N, Harrison P, Lock D, Crampin S, Palmer R E and Sloan P A, 2016, *Nat. Commun*, **7**, 12839

[44] Sloan P A, Sakulsermsuk S and Palmer R E, 2010, *Phys. Rev. Lett*, **105**, 048301

[45] Ju B-F, Chen Y-L, and Ge Y, 2011, *Rev. Sci. Instrum*, **82**, 013707

[46] Guise O L, Ahner J W, Jung M-C, Goughnour P C, and Yates J T, 2002, *Nano Lett*, **2**, 191-193

[47] Hla S-W, Braun K-F, Iancu V, and Deshpande A, 2004, *Nano Lett*, **4**, 1997-2001

[48] Uchida H, Huang D, Grey F, and Aono M, 1993, *Phys. Rev. Lett*, **70**, 2040-2043

[49] H Neddermeyer, 1996. *Rep. Prog. Phys.,* **59,** 701

[50] Avouris Ph and Wolkow R, *Phys. Rev. B*, 1989, **39**, 5091 – 5100

[51] Takayanagi K, Tanishiro Y, Takahasi S and Takahasi M, 1985, *Surf. Sci,* **164**, 367-392

[52] Tromp R M, Hamers R J, Demuth J E, *Science*, 1986, **234**, 304-309

[53] Stich I, Payne M C, King-Smith R D, Lin J-S and Clarke L J, 1992, *Phys. Rev. Lett*, **68**, 1351-1354

[54] Cao Y, Deng J F and Xu G Q, 2000, *J. Chem. Phys,* **112,** 4759-4767

[55] Tromp R M, Hamers R J and Demuth J E, 1986, *Science*, **234**, 304-309

[56] Himpsel F J, Hollinger G and Pollak R A, 1983, *Phys. Rev. B,* **28**, 7014-7018

[57] Oura k, Lifshits V G, Saranin A A, Zotov Z and Katayama M, *Surface Science: An Introduction,* Springer, 2003

[58] Zangwill A, *Physics at surfaces*, Cambridge: Cambridge University Press, 1988

[59] McEllistrem M, Haase G, Chen D, and Hamers R, 1993, *Phys. Rev. Lett,* **70**, 2471-2474

[60] Mysliveček J, Stróżecka A, Steffl J, Sobotík P, Ošťádal I and Voigtländer B, 2006, *Phys. Rev. B,* **73**, 161302

[61] Sloan P A and Palmer R E, 2006, *J. Phys.: Condens. Matter*, **18**, S1873

[62] Lu X, Polanyi J C and Yang J S Y, 2006, *Nano Lett*, **6**, 809-814

[63] Wolkow R A and Moffatt D J, 1995, *J. Chem. Phys,* **103**, 10696

[64] Brown D E, Moffatt D J and Wolkow R A, 1998, *Science,* **279**, 542-544

[65] Utecht M, Pan T, Klamroth T and Palmer R R, 2014, *J. Phys. Chem. A,* **118**, 6699-6704

[66] Tomimoto H, Takehara T, Fukawa K, Sumii R, Sekitani T and Tanaka K, 2003, *Surf. Sci.,* **526**, 341–350

[67] Sloan P A, Hedouin M F G, and Palmer R E, 2003, *Phys. Rev. Lett,* **91**, 118301

[68] Nickel A, Lehmann T, Meyer J, Esienhut F, Ohmann R, Ryndyk D A, Joachim C, Moresco F and Cuniberti G, 2016, *J. Phys. Chem.*, **120**, 27027-27032

[69] Soukiassian L, Mayne A J, Carbone A, and Dujardin G, 2003, *Phys. Rev. B,* **68**, 035303

[70] Shen T-C, Wang C, Abein G C, Tucker J R, Lyding J W, Avouris P, and Walkup R E, 1995, *Science*, **268**, 1590

[71] Stokbro K, Yu-Kuang Hu B, Thirstrup C, and Xie X C, 1998, *Phys. Rev. B*, **58**, 8038

[72] Rusimova K R, Purkiss R M, Howes R, Lee F, Crampin S and Sloan P A, 2018, *Science*, **361**, 1012-1016

[73] Saalfrank P, Boendgen G, Corriola C and Nakajima T, 2000, *Faraday Discuss.*, **117**, 65-83

[74] Stipe B C, Rezaei m A, Ho W, 1998, *Science,* **279**, 1907-1909

[75] Lock D, Sakulsermsuk S, Palmer R E and Sloan P A, 2015, *J. Phys.: Condens. Matter*, **27**, 054003

[76] Majzik P, Drevniok B, Kaminski W, Ondracek M, McLean B and Jelinek P, 2013, *ACS Nano*, **7**, 2686-2692

[77] Enkhtaivan B and Oshiyama A, 2017, *Phys. Rev. B*, **95**, 035309

[78] Alavi S, Rousseau R, Patitsas S N, Lopinski G P, Wolkow R A and Seideman T, 2000, *Phys. Rev. Lett*, **85**, 5372-5375

[79] Jelínek P, Ondráček M and Flores F, 2012, *J. Phys.: Condens. Matter*, **24**, 084001

[80] Paul W, Yang K, Baumann S, Romming N, Choi T, Lutz C P and Heinrich A J, 2017, *Nat. Phys.*, **13**, 403-408

[81] Ryan P M, Teague L C, Naydenov B, Borland D and Boland J J, 2008, *Phys. Rev. Lett,* **101**, 096801

[82] Anggara K, Huang K, Leung L, Chatterjee A, Cheng F and Polanyi J C, 2016, *Nat. Commun*, **7**, 13690

[83] Pascual J I, Lorente N, Song Z, Conrad H and Rust H-P, 2003. *Nature*, **423**, 525-528

[84] Liu Q, Lei Y, Shao X, Ming F, Xu H, Wang K and Xiao X, 2016, *Nanotechnology,* **27**, 135704

[85] Rusimova K R, and Sloan P A, 2017, *Nanotechnology*, **28**, 054002

[86] Feenstra R M, 1994, *Phys. Rev. B*, **50**, 4561-4570

[87] Purkiss R M, Rusimova K R and Sloan P A [in preparation]

[88] Huan Q, Jiang Y, Zhang Y Y, Ham U and Ho W, 2011, *J. Chem. Phys*, **135**, 014705

[89] Dupont-Ferrier E, Mallet P, Magaud L, and Veuillen J-Y, 2007, *Phys. Rev. B*, **75**, 205315

[90] Kuhnke K, Große C, Merino P and Kern K, 2017, *Chem. Rev*, **117**, 5174-5222

[91] Iwami M, Ueara Y and Ushioda S, 2001, *Appl. Surf. Sci,***169**, 188-192

[92] Berndt R and Gimzewski J K and Johansson J, 1993, *Phys. Rev. Lett*, **71**, 3493-3496

[93] Abraham D L, Veider A, Schönenberger C, Meier H P, Arent D J and Alvarado S F, 1990, *Appl. Phys. Lett*, **56**, 1564-1566

[94] Thirstrup C, Sakurai M, Stokbro S and Aono M, 1999, *Phys. Rev. Lett*, **82**, 1241-1244

[95] Andor Luca R Price Performance EMCCD*,* Specification Document, *Oxford Instruments*, https://www.andor.com/pdfs/specifications/Andor_Luca-R_604_Specifications.pdf, [online-accessed 24/05/18]

[96] Lock D, Rusimova K R, Pan T, Palmer R E and Sloan P A, 2015, *Nat. Commun,* **6**, 8365

[97] Rusimova K R, 2016, *'Mechanisms of Local and Nonlocal Atomic Manipulation with a Scanning Tunnelling Microscope',* PhD Thesis, University of Bath

[98] Eelbo T, Sikora M, Bihlmayer G, Dobrzanski M, Kozłowski A, Miotkowski I and Wiesendanger R, 2013, *New J. Phys.,* **15**, 113026

[99] Bolotov L, Uchida N, and Kanayama T, 2001, *Eur. Phys. J. D*, **16**, 271–274

[100] Novosolov K S, Geim A K, Morozov S V, Jiang D, Zhang Y, Dubonos S V, Grigorieva I V and Firsov A A, 2004, *Science,* **306**, 666-669

[101] Yang H, Mayne A J, Cejas C, Dujardin G and Kuk Y, 2013, *Appl. Phys. Lett.*, **102**, 223104

[102] Hornett S M, Heath M, Horsell D W, and Hendry E, 2014, *Phys. Rev. B,* **90**, 081401

[103] Hossain et al., 2012, *Nat. Chem.,* **4**, 305-309

[104] Johns J E and Hersam M C, 2013, *Acc Chem Res,.* **46**, 77–86

[105] Sorescu D C, and Jordan K D, *J. Phys. Chem. B,* 2001, **105**, 11227-11232

[106] Decker R, Wang Y, Brar V W, Regan W, Tsai H-Z, Wu Q, Gannett W, Zettl A and Crommie M F, 2011, *Nano Lett.*, **11**, 2291–2295